



Multiparametric organ modeling for shape statistics and simulation procedures

Juan Carlos Prieto Bernal

► To cite this version:

Juan Carlos Prieto Bernal. Multiparametric organ modeling for shape statistics and simulation procedures. Signal and Image processing. INSA de Lyon, 2014. English. NNT: 2014ISAL0010 . tel-01149922

HAL Id: tel-01149922

<https://theses.hal.science/tel-01149922>

Submitted on 7 May 2015

HAL is a multi-disciplinary open access archive for the deposit and dissemination of scientific research documents, whether they are published or not. The documents may come from teaching and research institutions in France or abroad, or from public or private research centers.

L'archive ouverte pluridisciplinaire **HAL**, est destinée au dépôt et à la diffusion de documents scientifiques de niveau recherche, publiés ou non, émanant des établissements d'enseignement et de recherche français ou étrangers, des laboratoires publics ou privés.



Numéro d'ordre : ISAL 0010

Année 2014

THÈSE
Délivrée par
L'Institut National des Sciences Appliquées de Lyon

DIPLÔME DE DOCTORAT
(arrêté du 7 aout 2006)

ÉCOLE DOCTORALE : Électronique, Électrotechnique, Automatique
Spécialité: STIC Santé

Soutenue publiquement le 31 Janvier 2014 par
Juan Carlos PRIETO

Multiparametric organ modeling for shape statistics and simulation procedures.

Jury

Christophe ODET	Professeur, INSA - Lyon	Directeur de thèse
Chantal MULLER	Maitre de Conférences, INSA - Lyon	Co-directeur de thèse
Martin STYNER	Maitre de Conférences, NIRAL - UNC	Rapporteur
Christian GERMAIN	Professeur, IMS - Université Bordeaux	Rapporteur
David ROUSSEAU	Professeur, INSA - Lyon	Examinateur
François COTTON	Professeur, Centre Hospitalier Lyon-Sud	Examinateur
Charles GUTTMANN	Maitre de Conférences, BWH - Boston Massachusetts	Examinateur
Stephen PIZER	Professeur, MIDAG - UNC	Examinateur

Acknowledgements

PAPA think (piensa), act (actua), persevere (persevera) and ambition (ambiciona).

– Jesus Prieto

First of all, I would like to thank my parents Martha Bernal and Jesus Prieto. They made the choice of adoption and they gave me the best they could. They taught me important values and made me the person that I am today.

To Prof. Chantal Muller, who gave me the opportunity to work on this project and trusted me from the beginning. I wish her the best.

It has been a privilege to work with Prof. Steve Pizer. Thanks to all the discussions we had, the most important contribution on this dissertation was achieved.

To Prof. Christophe Odet for his support during this thesis.

I would like to thank the rest of my thesis committee: Prof. Martin Styner, Prof. Christian Germain, Prof. David Rousseau, Prof. François Cotton and Prof. Charles Guttmann, for their feedback and comments.

A warm thought to my friends in Lyon and Chapel Hill for all the good moments we had during this PhD.

Finally, I would like to thank Aurélie Nguyen for her patience and for taking care of me when I was writing this manuscript.

Abstract

Geometric modeling has been one of the most researched areas in the medical domain. Today, there is not a well established methodology to model the shape of an organ. There are many approaches available and each one of them have different strengths and weaknesses.

Most state of the art methods to model shape use surface information only. There is an increasing need for techniques to support volumetric information. Besides shape characterization, a technique to differentiate objects by shape is needed. This requires computing statistics on shape.

In this work, we use a technique for shape modeling that is able to model surface and internal features, and is suited to compute shape statistics.

Using this technique (s-rep), a procedure to model the human cerebral cortex is proposed. This novel representation offers new possibilities to analyze cortical lesions and compute shape statistics on the cortex.

The second part of this work proposes a methodology to parameterize the interior of an object. The method is flexible and can enhance the visual aspect or the description of physical properties of an object.

The geometric modeling enhanced with physical parameters is used to produce simulated magnetic resonance images. This image simulation approach is validated by analyzing the behavior and performance of classic segmentation algorithms for real images.

Résumé

La modélisation géométrique a été l'un des sujets les plus étudiés pour la représentation des structures anatomiques dans le domaine médical. Aujourd'hui, il n'y a toujours pas de méthode bien établie pour modéliser la forme d'un organe. Cependant, il y a plusieurs types d'approches disponibles et chaque approche a ses forces et ses faiblesses.

La plupart des méthodes de pointe utilisent uniquement l'information surfacique mais un besoin croissant de modéliser l'information volumique des objets apparaît. En plus de la description géométrique, il faut pouvoir différencier les objets d'une population selon leur forme. Cela nécessite de disposer des statistiques sur la forme dans organe dans une population donné.

Dans ce travail de thèse, on utilise une représentation capable de modéliser les caractéristiques surfaciques et internes d'un objet. La représentation choisie (srep) a en plus l'avantage de permettre de déterminer les statistiques de forme pour une population d'objets.

En s'appuyant sur cette représentation, une procédure pour modéliser le cortex cérébral humain est proposée. Cette nouvelle modélisation offre de nouvelles possibilités pour analyser les lésions corticales et calculer des statistiques de forme sur le cortex.

La deuxième partie de ce travail propose une méthodologie pour décrire de manière paramétrique l'intérieur d'un objet. La méthode est flexible et peut améliorer l'aspect visuel ou la description des propriétés physiques d'un objet.

La modélisation géométrique enrichie avec des paramètres physiques volumiques est utilisée pour la simulation d'image par résonance magnétique pour produire des simulations plus réalistes. Cette approche de simulation d'images est validée en analysant le comportement et les performances des méthodes de segmentations classiquement utilisées pour traiter des images réelles du cerveau.

List of Figures

2.1	Rotated figure.	5
2.2	Snake's energy.	6
2.3	Segmentation with orientation.	7
2.4	SPHARM description.	10
2.5	MAT instabilities.	13
2.6	MA Pruning.	13
2.7	Medial atom definition.	15
2.8	Top, bottom and crest surfaces.	15
2.9	Slab type s-rep.	18
2.10	Slab's MS interpolation.	21
2.11	Top and bottom surface interpolation.	22
2.12	Radius interpolation.	23
2.13	Interpolated crest curve.	24
2.14	Slab's surfaces interpolation.	24
2.15	Amygdala's s-rep.	25
2.16	Quasi-tube interpolation.	26
2.17	Unfolding the s-rep.	27
2.18	X2U's map volume rendering.	27
3.1	Brain MRI.	30
3.2	Atom close up.	31
3.3	Flow diagram of s-rep projection and cortex folding.	32
3.4	Inflation procedure, mapping the cortex on a sphere.	33
3.5	Resampling of the s-rep.	34
3.6	Sphere's north and south pole sampling.	36
3.7	GM and WM surface mean error: grid size.	37
3.8	Average area of an srep's quad.	38
3.9	GM and WM surface mean error: log scale.	38
3.10	Comparison of the interpolated and original WM surfaces.	39
3.11	Comparison of the interpolated and original GM surfaces.	40
3.12	Mean modes of variation for the cortex.	41
3.13	S-rep deformation using the first mode.	42
3.14	Average thickness of the cortex.	43
3.15	Mean shape of the cortex: CPNS and <i>Freesurfer</i> .	44
4.1	Texture segregation.	46
4.2	Exemplar textures.	50
4.3	Texture synthesis neighborhoods.	51
4.4	Isotropic texture synthesis.	52
4.5	Isotropic texture synthesis of physical parameters.	53

4.6	Anisotropic texture synthesis.	53
4.7	Anisotropic texture synthesis and distance maps.	54
4.8	<i>SRμCT</i> and μ <i>MRI</i> synthesis.	55
4.9	Surface rendering of <i>SRμCT</i> trabecular bone.	55
4.10	Surface rendering of μ MR trabecular bone.	56
4.11	RGB histograms of exemplar and synthesized solid.	57
4.12	Histogram comparison: μ MR	57
4.13	Histogram comparison: physical parameters.	58
4.14	Morphological evaluation of <i>SRμCT</i> texture.	59
4.15	Morphological evaluation of μ MR texture.	60
5.1	<i>SimuBloch</i>	65
5.2	<i>SimuBloch</i> physical parameters.	66
5.3	Warping a solid texture to an s-rep.	67
5.4	S-rep textured with spheres and striated cardiac tissue.	69
5.5	S-rep of the cortex with zebra texture.	70
5.6	Image samples of physical parameters	71
5.7	Multi object subcortical	72
5.8	Synthetic textured complex.	73
5.9	Simulated brain MRI for three subjects.	74
5.10	Original brain MRI for three subjects.	75
5.11	Segmented MRI for three simulated subjects.	76
5.12	Visual comparison for cortical surface for Subject 1.	77
5.13	Visual comparison for cortical surface for Subject 2.	78
5.14	Visual comparison for cortical surface for Subject 3.	79
B.1	Rotation of the sub-sphere A_{d-1} to the northpole.	110
B.2	Best fitting sphere and projection to sub-sphere	111

Contents

Abstract	v
Contents	xi
List of Symbols	xiii
1 Introduction	1
2 3D object representation	3
2.1 Introduction	3
2.2 Surface representation	4
2.2.1 Landmark representations	4
2.2.2 Boundary representations	5
2.3 Solid representation	11
2.3.1 Atlas based deformable models	11
2.3.2 Medial representations	11
2.3.3 Quasi-medial representations	16
2.4 Object modeling using s-reps	20
2.4.1 MS interpolation	20
2.4.2 Crest interpolation	22
2.4.3 Internal coordinates of an object	26
2.5 Conclusions	26
3 Cortex modeling via s-reps	29
3.1 Introduction	29
3.2 Acknowledging the true shape of the cortex	31
3.2.1 Spherical representation of the cortex by <i>Freesurfer</i> and rotation . .	32
3.2.2 Transforming the srep into a circular log grid	34
3.2.3 Srep projection from the plane to the sphere	35
3.2.4 Fitting the srep to <i>Freesurfer</i> 's data	35
3.2.5 Folding the srep: from the sphere to the cortex	36
3.3 Evaluation of the implied GM and WM surfaces	37
3.3.1 Best srep size	37
3.3.2 Best srep sampling	37
3.4 Shape statistics of the cortex using CPNS	39
3.5 Conclusion	41

4 Texture synthesis for 3D object representation	45
4.1 Introduction	45
4.2 Texture synthesis methods and applications	47
4.2.1 Procedural texture synthesis	47
4.2.2 Exemplar based texture synthesis	47
4.2.3 Enhancing medical applications using textures	49
4.3 Solid texture synthesis	49
4.3.1 Search phase	51
4.3.2 Optimization phase	51
4.3.3 Histogram Matching	52
4.4 Types of solid textures	52
4.4.1 Isotropic texture from a 2D exemplar texture	52
4.4.2 Anisotropic texture from many 2D exemplar textures	53
4.4.3 Anisotropic texture constrained by additional masks	54
4.5 Evaluation of the synthesized textures	54
4.5.1 Statistical assessment	55
4.5.2 Morphological assessment	56
4.6 Conclusion	60
5 MRI simulation of the brain using textured s-reps	63
5.1 Introduction	63
5.2 Overview of <i>SimuBloch</i>	64
5.3 Texturing s-reps	65
5.3.1 Warping RGB textures	66
5.3.2 MRI simulation with textures of physical parameters	68
5.4 Evaluation of the simulated image	71
5.5 Conclusions	71
6 Conclusions and perspectives	81
6.1 Synopsis of the work	81
6.2 Future work	82
7 Résumé de thèse	83
7.1 Introduction	83
7.2 Représentation des objets en 3D	84
7.2.1 Représentations médiane	85
7.2.2 Représentations quasi-médianes	87
7.2.3 Modélisation d'objet avec s-reps	88
7.2.4 Conclusions	91
7.3 Modélisation du cortex par de s-reps	92
7.3.1 Introduction	92
7.3.2 La véritable forme du cortex	93
7.3.3 Conclusions	94
7.4 Synthèse de texture pour la représentation d'objets en 3D	94
7.4.1 Introduction	94
7.4.2 Synthèse de texture solide basé sur optimisation	96
7.4.3 Conclusion	97
7.5 Simulation d'IRM du cerveau à l'aide des s-reps texturés	97
7.5.1 Introduction	97
7.5.2 Simulation d'IRM avec s-reps texturés	98

7.5.3	Conclusion	99
7.6	Conclusions et perspectives	99
7.6.1	Conclusions	99
7.6.2	Perspectives	100
Appendix		105
A Principal Component Analysis		105
A.1	Computing PCA	105
A.1.1	Compute the mean	105
A.1.2	Compute the covariance of the data	105
A.1.3	Perform eigenanalysis on the covariance	106
A.1.4	Compute the total variance	106
A.1.5	Use a number of eigenvalues	106
A.2	Producing a compact data set	106
A.3	Recovering the original data	106
B Principal Nested Spheres		109
B.1	Computing PNS	109
B.1.1	Arc distance	109
B.1.2	Subsphere	110
B.1.3	Rotation to the north pole	110
B.1.4	Transformation of subsphere	110
B.1.5	Best fitting subsphere	110
B.1.6	Sequence of principal nested spheres	111
B.2	Residuals and principal arcs	112
Bibliography		122

Abbreviations

μ MR	Micro magnetic resonance
AAM	Active appereance models
ASM	Active shape models
b-reps	Boundary representations
CA	Computational anatomy)
CT	Computed tomography
DT	Distance Transform
DTI	Diffusion tensor imaging
ET	Echo time
FEM	Finite element method
MA	Medial axis
MAT	Medial axis transform
MRF	Markov Random Field
MRG	Model Guided Rendering
MRI	Magnetic resonance imaging
MS	Medial axis or medial sheet
ODE	Ordinary differential equation
PDM	Point distrubution models
PCA	Principal component analysis
PET	Positron emission tomography)
RF	Radio Frequency
SR μ CT	Synchrotron Radiation Computed Micro-Tomography
s-rep	Skeletal representation
SS	Skeletal sheet
TR	Time repetition
US	Ultra sound

1

Introduction

Recent advances on digital imaging modalities and computation have enabled an emerging field studying the biological variability of human anatomy. This field is called CA (computational anatomy).

CA as defined by [Grenander and Miller (1998)] has three principal aspects: construction of anatomical manifolds or shape modeling by points, curves, surfaces and volumes; comparison of these models; and statistical analysis of shape variability.

The statistics allows for inference and hypothesis testing of disease states. This is done using the statistical description to determine the probability of a hypothesis to be true or false. In other words, a new sample is classified as diseased or healthy according to its shape.

The automated construction of anatomical models has been the main interest of many research groups around the world. These models are based on algorithms and equations that capture the behavior and/or the appearance of the object.

Besides hypothesis testing, the models are also used for various types of simulation procedures such as simulation of medical images. Medical imaging consists in acquiring details of the interior of the human body by using different techniques. Among these techniques we find MRI (magnetic resonance imaging), CT (computed tomography), US (ultrasound) or PET (positron emission tomography). They are widely used to diagnose and plan treatment for patients with the information acquired in the image. These imaging devices can be very expensive, they require regular maintenance and are used only by specialized staff. In this context, image simulation is defined as the process of producing a synthesized image from a specific modality using the geometry of a virtual object. The virtual object in question could be an organ or a system of organs.

One purpose of image simulation is to improve imaging devices. This is done by acquiring better understanding of image acquisition phenomena or calibrating a specific set of parameters that will produce a desired outcome and then translate the experience to the real device. Another use for simulated images is to evaluate the performance of segmentation algorithms as the results can be directly correlated to the virtual model.

Other types of simulations are done to understand biological process, muscle deformation, cardiac cycle, respiratory cycle, cortical folding etc.

Knowing all the potential applications on the medical domain, the current challenge today is to create a virtual human, in other words, to create a model capable of integrating anatomical, physiological, mechanical, biological and physical information. This virtual human could be used to improve simulation procedures and also hypothesis testing for disease states.

The first objective of this dissertation is to provide a technique generic enough to model

the shape of various organs, giving the possibility to include information from different spatial scales, imaging modalities or other sources. To model the shape of an object, there are many approaches available. Notably deformable models have proven to be successful. They are able to automate, to a certain degree, image segmentation of structures and they also produce statistics on the deformations. Unfortunately, some of the techniques don't provide the necessary mechanisms for further use on simulation procedures. Chapter 2 summarizes the important features of the techniques frequently used to model the geometry of objects. The choice of the modeling technique should meet some specific requirements that will be used to model the human cerebral cortex. The representation should support the extremely folded geometry of the cortex and also be capable to locate internal features or provide a sense of orientation at every place inside the object.

Chapter 3 explains a methodology to create a cortex representation. The modeling technique relates to the true shape of the cortex which is that of a folded slab as most of the state of the art methods only use surface information or model the folds locally.

The second objective is to provide a mechanism to synthesize solids, meaning surface and internal properties of the object must be available. The procedure to synthesize solids uses small two dimensions textured images as exemplars. The synthesized result is visually and statistically similar to the exemplar. The textured images can be from various sources including images from the web, histology and complex ones such as MRI physical parameters acquired with relaxometry techniques. The generated solids can be used to enhance the visualization and/or internal properties of the models created using the techniques described in Chapter 2. Chapter 4 explains the solid synthesis procedure.

The third objective is to use the geometric description enhanced with internal properties such as physical parameters and generate simulated MRIs. Chapter 5 explains MRI simulation and uses the techniques for geometric modeling and solid synthesis to create some virtual objects. These objects are used to simulate MRIs, which are validated with well known segmentation algorithms.

Chapter 6 concludes the current research study and future perspectives are declared.

2

3D object representation

2.1 Introduction

Advances in technology have made possible to develop high quality 3D models that are used in various sectors of the industry. They implement a mathematical description of the appearance of the object that can be used for animation, prototyping and simulation purposes. The geometry of the object is the core of these procedures.

Today's challenge is to create models of objects that are adapted to perform robust simulation procedures. They should provide the mechanisms to include information from various sources at different spatial scales and also work in multi-object scenarios. Moreover, their shape must be representative of a population, implying the establishment of a methodology to compute mean shapes and a description of the variability in the population. There is no standard technique to deal with shape, nor to compute average shapes. Those are rather challenging tasks in computer vision.

Developing a model with the characteristics stated above opens the possibility to improve existing simulation procedures, acquire a better understanding of the systems in the human body, develop better automated analysis on medical images and also improve personalized medicine. Furthermore, (non-invasive) medical interventions could be planned using patient specific models since they are created from the information acquired on the medical images.

A review of state of the art techniques to improve 3D modeling of organs is done in the following section. 3D modeling can be divided broadly into two categories: surface modeling and solid modeling.

Surface models represent only the outer layer of the object. They are stored as a set of primitives such as points, edges or polygons and define the boundary of the object. During the last 20 years, most of the research has been focused on this category as they are easier to manipulate. Surface modeling can be divided into different sub-categories: landmark representations and boundary representations or b-reps.

Solid models on the other hand represent both, the exterior and the interior of the object. They can be divided mainly into two sub-categories: atlas based deformable models and quasi medial-representations.

The chapter is organized as follows, Section 2.2 gives an overview of the most important surface modeling techniques, Section 2.3 gives an overview of solid modeling techniques with emphasis on s-reps, the technique that I will be using throughout this dissertation. My contribution to s-reps are a new interpolation method based on splines, which will be explained in Section 2.4. Section 2.5 gives a conclusion of the methods.

2.2 Surface representation

Surface representation techniques can be divided broadly into two categories: landmark representations and boundary representation or b-reps. I overview the most prominent authors in the following section.

2.2.1 Landmark representations

Landmark representations were proposed by [Kendall (1989)]. Since landmark representation is a simple method to perform shape analysis, there has been an extensive study of their geometry and statistics [Bookstein (1991)], [Dryden and Mardia (1993)], [James Rohlf and Marcus (1993)], [Small (1996)].

Kendall understood shape as a set of prominent features (landmarks) in the objects and gave the following definition:

Definition 1. *Shape is all the geometrical information that remains when a specified group of transformations are filtered from the object. That group consists of translations, rotations and scaling.*

This filtering is accomplished by Procrustes analysis.

Procrustes analysis is done to match the landmarks by putting them on a common frame and derive valid information from their displacement. This is equivalent to understanding how the shape deforms on the population.

I will briefly describe how a Procrustes analysis is done. To filter the location, the object must be centered on its geometric center or centroid. Let $O = \{x_i : i < k, k \in N\} \in R^n$ be the set of landmarks that compose an object. The centroid of O is defined in Equation 2.1.

$$C(O) = \frac{\sum_i^k O(i)}{k} \quad (2.1)$$

The object is then translated by $C(O)$ i.e., $O_t = \{x_i - C(O) : i < k, k \in N\} \in R^n$. We will see in Section 2.3.2 that in some cases, centering at the centroid is not adequate to perform shape analysis.

To filter the scale or make O unit scale, the object is normalized. Scale is defined as a linear transformation that enlarges or shrinks an object. To remove the scale of an object the root mean square distance from the points to the centroid must be equal to 1. The calculation of this coefficient is defined in Equation 2.2.

$$N(O) = \sqrt{\frac{\sum_i^k (O(i) - C(O))^2}{k}} \quad (2.2)$$

The object O is scaled by $1/N(O)$: $O_s = \{O(i)/N(O) : i < k, k \in N\} \in R^n$.

The last step is to filter the rotation, which is defined as moving an object around a point or axis of rotation, as shown in figure 2.1. In this example, the object is rotated 45° clockwise and the axis of rotation is the crossproduct between the x and y axes.

Since a rotation can be expressed in matrix form, the alignment problem can be done iteratively by minimizing the distance from the points in two objects as shown in Equation 2.3.

$$[\hat{\Omega}] = \arg \min_{\Omega} ||\Omega O_i - T O_i|| \quad (2.3)$$

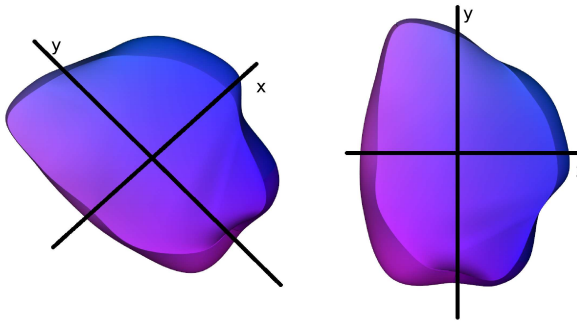


Figure 2.1: Figure rotated 45 degrees clockwise.

where Ω is a rotation matrix around the centroid of the object. O is an object and TO is a target object or template where both objects are centered on the origin and have unit scale. The problem consists in finding a matrix Ω such that the distance from points in O is minimum to the points in TO .

Using matched landmarks in a population of objects, this enables the study of shape by analyzing the displacements of the landmarks from the target to each object across the population.

Further improvements of landmark representations sought to produce constrained diffeomorphic deformations i.e., differentiable maps that have a differentiable inverse. Without the constraint, mapping an unfolded template to a folded structure produces non diffeomorphic deformation and causes to lose the geometry and topology of the template.

[Joshi and Miller (2000)] associated the transformation with an energy term, forcing the existence and uniqueness of the solution, thus, enabling the creation of smooth differentiable maps. This causes the landmarks to deform correctly to the target object and preserve the topology even if it is curved.

Although landmark matching performs well in the study of biological shape and is able to compute statistics from landmark displacements that capture information on scale, translation, rotation and shear. Information on bending, widening and elongation are not very well captured by the approach. Another major drawback is on landmark positioning. This is usually done by hand, which is time consuming.

2.2.2 Boundary representations

Boundary representation include the following approaches: active contours, active shape/appearance models and projection onto orthogonal functions.

Active contours

Active contours is a method proposed by [Kass *et al.* (1988)], commonly known as snakes. The method was conceived mainly for image segmentation procedures based on curve evolution.

It starts with the definition of a contour V composed by a set of points p_i and an energy function defined for V . The function has two components corresponding to the internal and external energy in the object being segmented or geometric typicality and an image match term as defined in Equation 2.6.

The geometric typicality is responsible for the smoothness of V and its propagation in a desired direction. Smoothness is controlled by *Econtinuity* and the direction of

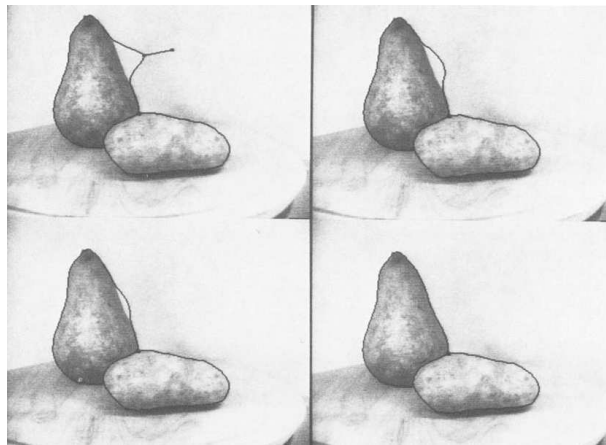


Figure 2.2: Image taken from [Kass *et al.* (1988)]. The contour moves back to the edge of the pear.

propagation by *Eballoon*, ensuring that the snake curve keeps propagating in the desired direction.

The image match term takes into consideration the intensity pattern around each vertex $p_i \in V$. *Eintensity* makes V move to a region of low or high image intensity information and *Egradient* attracts V to the edges of the object being segmented. The whole energy of the contour is defined by the integral in Equation 2.7.

$$E(V(s)) = \alpha Eint(V(s)) + \beta Eext(V(s))ds \quad (2.4)$$

$$Eint(V) = \gamma Econtinuity(V) + \delta Eballoon(V) \quad (2.5)$$

$$Eext(V) = \eta Eintensity(V) + \varphi Egradient(V) \quad (2.6)$$

$$E_{\text{snake}} = \int_0^1 E(V(s))ds \quad (2.7)$$

As shown in Figure 2.2, the contour maps back to the edge of the pear after the perturbation; this place is where the minimum is found.

Two major drawbacks of the active contour model are in the initialization step since the countour must be placed according to the object being segmented, and the need for the boundaries of the object to be defined by a gradient, i.e., to have a smooth boundary with contrast everywhere.

[Chan and Vese (2001)] proposed an active contour model based on the segmentation techniques by [Mumford and Shah (1989)] and the level set method. The level-set method models the internal information of an object. An example of a level set method is the DT (distance transform). The DT labels each pixel in the image with the distance value to the nearest boundary point, having 0 at the boundary and either positive or negative in the interior and exterior of the object. Even though this information could be used to locate and reference the position of internal features in the object, the information is only used to produce boundary segmentations or in other words, to model the curve/surface propagation flow until reaching a stable position.

Figure 2.3 shows the automatic segmentation of an object whose boundaries are not well defined and the contour can be place anywhere in the image.

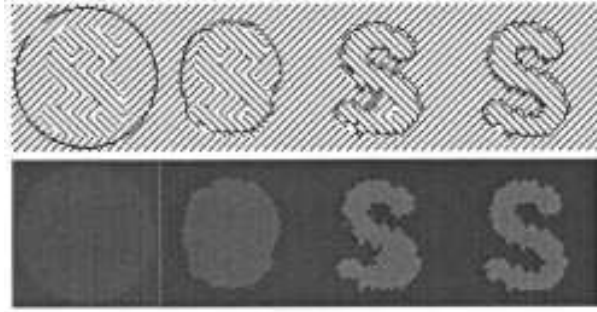


Figure 2.3: Image taken from [Chan and Vese (2001)]. The contour of 'S' is not well defined, the segmentation succeeds due to the grouping based on orientation identity.

In some situations the regions that are being segmented could be divided, due to high noise on the image or occlusion. To solve this problem, [Jean-Loic *et al.*] proposed a region growing approach that includes different type of descriptors in the minimization process.

The approach defines regions in the image via a discrete function:

$$\phi^n(x) = \begin{cases} 1, & \text{for } x \in \Omega_{in} \\ 0, & \text{for } x \in \Omega_{out}, \end{cases} \quad (2.8)$$

where Ω_{in} and Ω_{out} are the regions that correspond to the segmented pixels. The regions defined in Ω , change according to the region-based energy $J(\phi^n)$, which must be designed so that its minimum corresponds to the expected solution. At each iteration n , the voxels that are connected to Ω_{in} are tested. If the addition of those voxels decreases the energy, then, they are accepted and the discrete function is updated as

$$\phi^{n+1}(x) = \frac{1}{2}(1 - sign(\Delta J(\phi^{n+1}))). \quad (2.9)$$

This approach has been tested in segmentation of the vascular tree in the lung as shown by [Prieto *et al.* (2012)d], [Prieto *et al.* (2012)b]. The descriptors used on the images are based on a vesselness criterion proposed by [Sato *et al.* (1997)] and on the gray levels of the original image. The objective is to detect tubular structures in the image.

The complete formulation using the vesselness descriptors is as follows:

$$\Delta J(\phi^{n+1}) = 1 - 2\phi^n(\Delta J_1(f, v)), \quad (2.10)$$

$$\Delta J_1(f, v) = \frac{v}{MaxV}(|v - \mu_{v_{in}}|^2 - |v - \mu_{v_{out}}|^2) + \left| \frac{f}{MaxF} \right| (|f - \mu_{f_{in}}|^2 - |f - \mu_{f_{out}}|^2), \quad (2.11)$$

where $MaxV$ is the maximum value of the vesselness criterion, $\mu_{v_{in}}$ and $\mu_{v_{out}}$ are the mean values of the vesselness image voxels in Ω_{in} and Ω_{out} respectively. $MaxF$ is the maximum value in the original image, and similarly $\mu_{f_{in}}$ and $\mu_{f_{out}}$ are the respective mean values in the image for the regions Ω_{in} and Ω_{out} .

After the segmentation is done by any of the curve evolution methods stated above, the user is left with a set of points that correspond to the boundary of the object. Once again, notice that the approaches lack the mechanisms to describe internal features of the objects.

The following section introduces segmentation using combined geometric and intensity models, known as active shape and appearance models.

Active shape and appearance models

ASM (Active shape models) was proposed by [Cootes *et al.* (1995)]. The approach is based on the formulation that complex images can be analyzed by using shape priors. It differs from previous approaches that search to segment structures based on edges or homogeneous regions by introducing a deformable model template of the objects that exist in the image.

A deformable template is defined as proposed by [Fisker (2000)]:

Definition 2. A **deformable template** model can be characterized as a model, which under an implicit or explicit optimization criterion, deforms a shape to match a known type of object in an image.

The segmentation procedure uses the deformable template and tries to minimize an energy function that matches the template on the image. In general terms, the approach could be described as observe, learn and match.

The observation stage consists in generating the set of training cases. To do this, each object or structure of interest is represented by a set of points or landmarks. These points can represent the boundary and internal or external features. For each case, the points are required to be placed in the same manner. This task is usually performed by hand and validated by an expert. Although automatic methods have been proposed to speed up the process [Hill *et al.* (2000)], [Heimann *et al.* (2007)], the outputs are often revised and corrected.

Once the landmarks are placed on each training case, they are aligned to a common set of axes. Recall that if the cases are not aligned, the statistics are meaningless.

After the alignment, the learning stage is done using PCA (principal component analysis); see Appendix A for details. PCA detects salient features or principal directions of variation, removes redundant information and produces a compact representation of the data.

Once the principal direction of variation is detected in the population, any of the training sets in the data can be approximated using

$$x_i \approx Pb + \bar{x} \quad (2.12)$$

where $P = (p_1 | p_2 | \dots | p_n)$ contains n eigenvectors (produced by PCA) and b is a n dimensional vector that defines a set of parameters of a deformable model.

The variance of the i_{th} parameter of b_i across the training set is given by λ_i . By applying limits $\pm 3\sqrt{\lambda_i}$ the resulting model is guaranteed to be in the population.

The final stage is to match a new input to the training cases. This could be done in an iterative process. Using the alignment explained in section 2.2, the matching of a new object x_i goes as follows:

1. Initialize b to zero.
2. Generate a model y using Equation 2.12 and appearance information.
3. Align y to x_i using the transformation Γ given by Equation 2.3.
4. Project x_i into model coordinates using Γ^{-1} , $x'_i = \Gamma^{-1}(x_i)$.
5. Project x'_i into the tangent plane to \bar{x} by scaling: $x''_i = x'_i / (x'_i \cdot \bar{x})$
6. Update $b = P^T(x''_i - \bar{x})$

7. Repeat from 2 until convergence.

This general approach to match shape has proven to be very effective in image segmentation. It has been applied in applications such as object tracking, detection and recognition.

The AAM (Active Appearance Model) proposed by [Cootes *et al.* (2001)] improves the ASM by learning image appearance statistics as well as the location of the landmarks, i.e., each appearance vector is built from the image intensities (grey level or multiple components as RGB). PCA is applied separately on the landmark information of appearance and location.

A third PCA is applied to search for correlation between the shape and appearance analysis. This final PCA is the one used to produce the approximations of a new model.

A speed-up of the method was also proposed by [Mitchell *et al.* (2002)] where the search for the closest model is done in a multi-scale fashion.

In general terms ASM and AAM are robust and efficient methods in image segmentation, we will see in section 2.3.2 that other methods similar to PCA are best suited to produce statistical information for 3D shape analysis.

Function based models

Function based modeling offers great flexibility and precision. The key concept is to use a set of smooth functions to approximately model the surface of an object. One of the strengths of using such functions is that the derivatives of the object's surface are available and boundary normals and curvatures can be derived analytically. In contrast to PDM (point distribution models such as landmark based or ASM), these methods efficiently represent a shape model by using fewer parameters.

Different types of functions can be used to reconstruct a surface, including orthogonal functions and spline based methods such as NURBS (Non-Uniform Rational Basis Splines).

There are many type of orthogonal functions: spherical wavelets [Schröder and Sweldens (1995)], SPHARM (spherical harmonics [Brechbühler *et al.* (1995)], Hermite polynomials [Bradley *et al.* (1997)], among others.

Spherical Wavelets describe surfaces that have spherical topology. A wavelet is a function that localizes a given function in space and scale. In other words, wavelets can represent a given function at multiple levels of detail and in multiple regions. They are superior to a conventional Fourier transform because they capture low and high frequency components of the signal at specific locations in time or space. Equation 2.14 shows the general formula of a wavelet.

$$\Psi_{a,b}(t) = \frac{1}{\sqrt{a}} \Psi\left(\frac{t-b}{a}\right) \quad (2.13)$$

$$x_a(t) = \int \int x(t) \Psi_{a,b}(t) dt \quad (2.14)$$

To create a spherical wavelet, the shape of the object is mapped onto the sphere, and a signal is sampled from it [Schröder and Sweldens (1995)]. The signal is decomposed in various steps of subsampling and differentiating. At the end, the procedure retains a coarse representation of the sphere. To recover the information lost during the sumbsampling of the signal, a Haar-like operator is used such that it retains the differences between the two stages [Schwartz (2008)]. The wavelet signal can be used for (lossy) signal compression

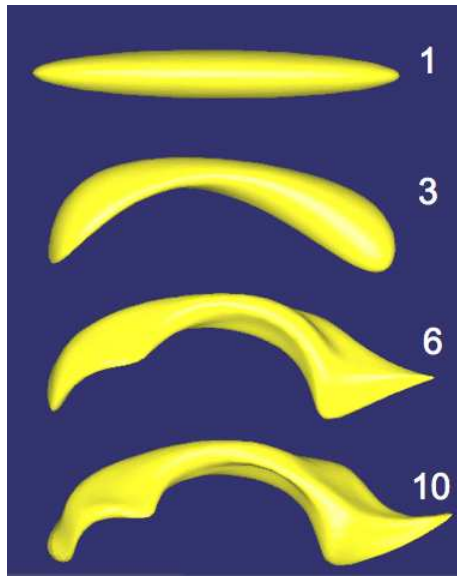


Figure 2.4: Image taken from [Styner *et al.* (2004)]. The SPHARM shape description of a human lateral ventricle shown at 4 different degrees (1, 3, 6, 10 harmonics).

and can be further analyzed by PCA. The analysis by PCA yields a mean shape that contains global information about the population. One of the major drawbacks of the approach lies in the fact that they are only able to represent objects of spherical topology. A second issue is also found for objects that need to be mapped on a sphere to produce the transformation. The mapping can introduce undesired distortion.

SPHARM functions only represent objects with spherical topology. This approach starts by unfolding and mapping the object onto a sphere, where each point can be expressed by two parameters in spherical coordinates (θ, ϕ) . An optimization is performed over the projected points that aims to preserve the area of original surface elements and minimize their distortion. Once the spherical parameterization is obtained, the surface $\vec{v}(\theta, \phi) = (x(\theta, \phi), y(\theta, \phi), z(\theta, \phi))^T$ can be expressed as

$$\vec{v}(\theta, \phi) = \sum_{l=0}^{\infty} \sum_{m=-l}^l \vec{c}_l^m Y_l^m(\theta, \phi) \quad (2.15)$$

where a least-squares procedure finds the best coefficients \vec{c}_l^m for the spherical harmonic basis functions $Y_l^m(\theta, \phi)$, for a review on spherical harmonic functions see [Mohlenkamp (2010)]. Image 2.4 shows a lateral ventricle surface using different harmonics.

SPHARM functions were used to estimate the age of a person based on the shape analysis of 3D X-ray CT images of human fourth ribs [Prieto *et al.* (2012)a].

Other type of functions can be used to model an object's surface. I am interested in the Hermite based functions and spline based methods. They will not be detailed in this section as they will be reviewed in Section 2.4.

2.3 Solid representation

2.3.1 Atlas based deformable models

Atlas based deformable models are included in solid representation because the geometry of the template (atlas) is well known, including its surface and internal features.

The atlas deformation is based on image registration techniques. To define image registration, I take the following definition given by [Brown (1992)]:

Definition 3. *Image registration can be defined as a mapping between two images both spatially and with respect to intensity.*

This matching produces deformation maps where every position p_i in the atlas I_a is known on the target I_t , therefore a registration can be expressed as

$$I_a(p_i) \approx g(I_t(f(p_i))) \quad (2.16)$$

where $f(p_i)$ is a spatial coordinate transformation and g is an intensity transformation.

Using the deformation maps, the position of every voxel (including internal features) from the atlas can be found on the target object.

To produce the registration, the transformation uses different image descriptors and spatial information. The mapping finds an optimal solution, where the optimum depends on the type of descriptors. For an updated review on image registration techniques see [Wyawahare *et al.* (2009)].

The outputs produced by registration techniques are smooth diffeomorphic maps; this means that local structure is also preserved during the deformation [Narayanan *et al.* (2005)]. For this reason, they have been used to develop transformation-based probabilistic atlas as shown by [Cao *et al.* (2005)] where it describes the variation of ventricular geometry and fiber organization (internal features).

Popular software suites for unsupervised segmentation and labeling of structures in the brain can be found in Freesurfer [Fischl *et al.* (2002)], [Fischl *et al.* (2004)] and BrainVisa [Pohl *et al.* (2007)]. Both are atlas based registration techniques.

Even though, image registration is known to have to much uncertainty, it is an approach broadly use for medical image analysis. It is difficult to evaluate how well the procedure performs and this is a critical point for medical diagnostics, where accuracy is needed. Uncertainty arises because the registration produces a single deterministic answer. Some authors propose solutions to solve this issue by doing posterior statistical analysis based on the intensity information [Kybic (2010)], [Simonson (2011)].

Measuring uncertainty is helpful to determine whether the results can be trusted or not. This measure could possibly be exploited in unsupervised segmentations or a multi-atlas registration scenario, by giving weights to each atlas based on their performance. In any case, statistics on deformations are still not adequately developed and remain the major drawback of the approach.

The following section is for medial representations, the type of modeling that will be used throughout this dissertation.

2.3.2 Medial representations

For even so simple a notion as location of an object, the contour or perimeter description is particularly poor.

– Harry Blum

The concept of medial representation started with [Blum *et al.* (1967)]. Blum noticed that for any shape, it was possible to calculate a medial axis and by doing it, the objects can be described from the inside, in contrast to the techniques in Section 2.2, that seek to model the outside of the object only.

To explain this concept Blum used a grassfire analogy, where the formation of the medial axis is done by setting fire to the outer layer of the object i.e., its boundary. The fire propagates uniformly towards the interior of the object and when the fronts meet we find the medial axis, a notion related to level-set. Following this concept the definition of a medial axis is as follow:

Definition 4. *The medial axis is the collection of interior points with at least two closest points on the boundary.*

In conjunction with the MA (MA will be use to denote medial axis or medial locus similarly) a MAT (medial axis transform) is generated:

Definition 5. *The medial axis transform contains the distance from each point of the medial axis to the boundary of the object.*

In the context of the grassfire analogy, the MAT adds to each axis point a value equivalent to the burning time from the boundary until two fronts meet at the MA. The MAT has been criticized as small boundary perturbations produce significant changes on the MA, which yields it impractical for shape description. Figure 2.5 shows an example of unstable MA. This instability has been the focus of many research groups that seek to produce a better computation of the MA. The idea is to identify the most meaningful subsets that compose the MA by trading exactness for stability.

Typically, a pruning of the MA is performed by a threshold value and a criterion that determines “substance” and “connection”, substance being the tangible part of the object and connection, how the parts are connected. To have a better understanding of this concept think of a complex object such as a hand. A hand is composed by a palm (a blob) and fingers (protrusions) or think of it as a collection of more complex objects. The substance is connected in a such a way that we perceive a hand.

Different authors provide the means of computing stable MA: see the methods by [Culver *et al.* (1999)], [Amenta *et al.* (2001)], [Katz and Pizer (2003)], [Miklos *et al.* (2010)].

A stable MA is a powerful shape descriptor that produces compact shape representations of the surface of an object and provides better notions of concepts such as “center point” and positions inside and relative to the object. As mentioned in section 2.2 the centroid is used to align objects on a common frame. In some cases the centroid of an object is outside the object itself, thus, making it unsuitable for alignment procedures. By computing the center point on the MA, it is guaranteed that it will be inside the object and its position will be stable under different transformations of the object [Liu *et al.* (2011)].

The notions such as a position inside the object or relative to other objects are not addressed by any of the techniques discussed in Section 2.2. These are trivial when an object is described by its MA. Positions inside the object will be discussed later in Section 2.4.3.

In 2D the MA is created by computing maximally inscribed discs, with at least two points on the boundary. The union of disk’s centers form the MA. In 3D the MA is composed by sheets, generated with maximally inscribed spheres. In general terms, the MA extends in higher dimensions, where it is composed by hypersurfaces generated with maximally inscribed hyperspheres.

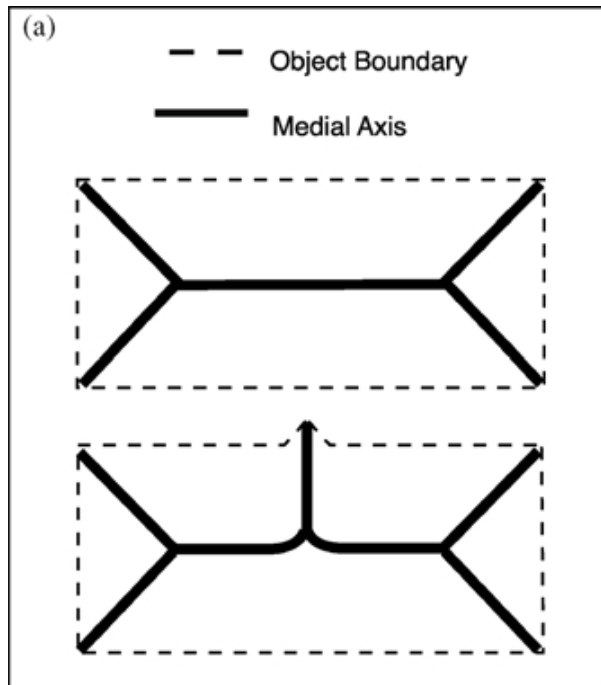


Figure 2.5: Image taken from [Katz and Pizer (2003)]. MAT instabilities: A tiny change in the boundary produces a large change in the MAT.

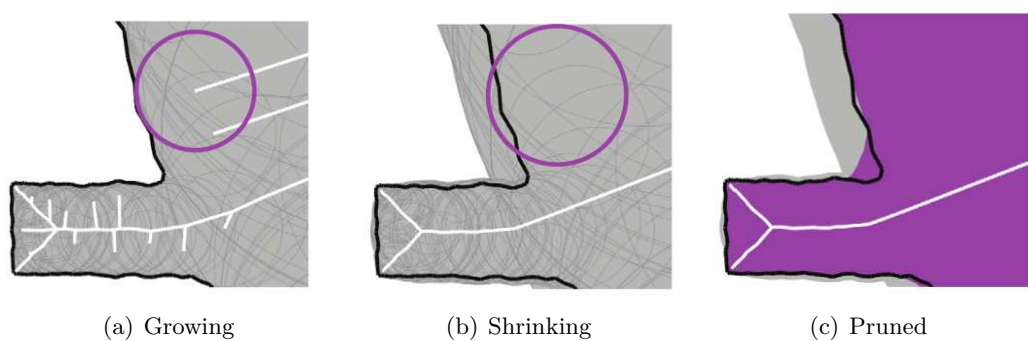


Figure 2.6: Image taken from [Miklos *et al.* (2010)]. Pruning the medial axis to detect important features.

To get an insight of one technique to compute a stable MA, let us take the example in figure 2.6. Figure 2.6.a shows the MA in white and a medial inscribed disk in purple. Figure 2.6.b shows the same disc scaled by δ . When all discs are scaled, large discs cover smaller nearby discs. Covered discs belong to branches that can be trimmed.

Using this criterion, the branches can be pruned using a scaling factor δ , keeping only the larger discs that belong to the 'substance' of the object.

Figure 2.6.c shows the simplified MA after the shrinking of the discs by the same δ . This procedure detects the least important branches on the MA, and by pruning them, the amount of data to represent the same figure with out loosing much precision is significantly reduced.

One important aspect left unanswered is if this type of representation is adequate to perform statistical analysis on a population of objects. One major difficulty will be to produce the correspondence of the branching structures. Statistics on branching objects is a subject of ongoing research by [Wang and Marron (2007)], [Sørensen *et al.* (2011)], [Aydin *et al.* (2011)], which is still not applicable to medial geometry. To use medial representations for statistical analysis on shape, the construction of the MA must be done in a different manner: the MA should have a stable structure for the population of objects we wish to represent.

If we take into consideration how the MA is built, we see that the procedure is a top-down approach, it starts on the boundary of the object and by using a certain criteria it gets to the MA. Another alternative is to operate the opposite way (down-top). We can find a down-top approach to build a MA in [Styner and Gerig (2001)].

In summary, Styner's method goes by computing an average MA from a population of objects and then sampling the average using a regular grid of points. The sampled grid of points is used as the new MA. To compute the average MA, a PDM of the branching structures is created by finely sampling their SPHARM representations. The PDM allows PCA to compute the average and finally the grid of points or m-rep (definition given shortly) is sampled by minimizing a distance function over the points. A series of tests are performed afterwards to assess the quality of the MA by generating different instances of the population using the PCA coefficients. For each instance, the m-rep is refitted, and an error measurement is estimated to evaluate how well it represents the whole population.

M-reps are continuous objects that define the MA of an object as a set of connected manifolds [Pizer *et al.* (1999)], [Yushkevich *et al.* (2003)], [Pizer *et al.* (2003)]. Figure 2.7 shows the components of the medial geometry. The MS (medial sheet, equivalent to MA in 2D) is parameterized by $MS(u, v)$ where u and v can take any value between $[0, 1] \in R$. The MS is a C^2 continuous set of medial atoms with a corresponding implied boundary y_0 for top surface and y_1 for bottom surface.

$$MS(u, v) = \{x, r, n_0, n_1\} \quad (2.17)$$

Equation 2.17 defines an atom for every (u, v) on the MS, where x is the position on the MS, n_0 and n_1 are the unit spoke directions, and r is the length of both vectors.

A different type of atom is found at the edges of the figure, named crest atoms. Figure 2.8 shows how the top and bottom surfaces join at the crest to produce the closed boundary of the object.

To describe an m-rep in the computer, a discrete set of atoms is used. From now on, the word m-rep relates to the discrete version of the object. M-reps use the interpolation mechanisms described in [Thall (2004)], which enables to reconstruct the object's surface. The interpolation matches the surface to the normals described by the vectors n_0 and n_1 . Matching the normals produces a C^2 continuous surface everywhere.

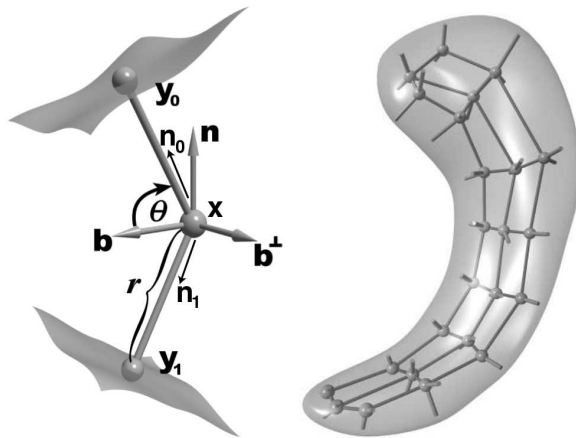


Figure 2.7: Image taken from [Fletcher *et al.* (2004)]. Medial atom definition (left) and a set of atoms representing a hippocampus (right). The atoms are arranged in a grid size 8×3 and are able to produce the boundary of the hippocampus.

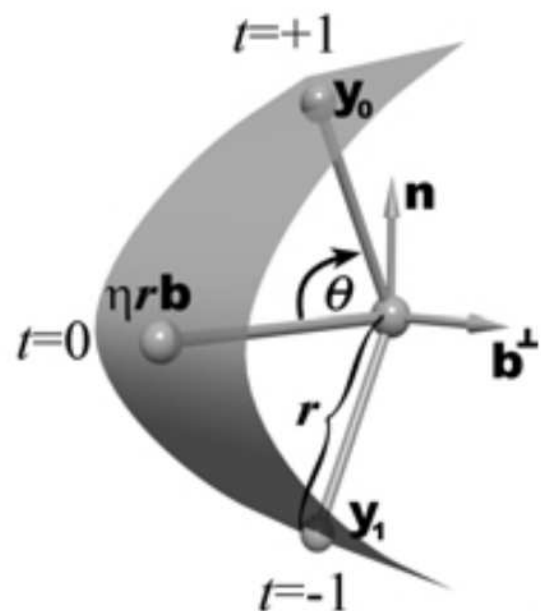


Figure 2.8: Image taken from [Pizer *et al.* (2003)]. Top and bottom surfaces of the m-rep join at the crest.

In summary, m-reps are efficient structures that describe in a multi-scale fashion the geometry of an object, they can be used for medical image segmentation [Pizer *et al.* (2005)] and perform statistical analysis on shape variability [Fletcher *et al.* (2004)].

The method used by m-reps to produce statistics is called PGA (principal geodesic analysis) a generalization of PCA to manifold data, which will be described briefly in the following section.

Principal geodesic analysis

We have seen that m-reps can represent a population of 3D figures by defining a stable MS and deforming it to best fit the various instances of the objects. One of the many strengths of m-reps is to describe shape changes in terms of thickness, bending and widening among the already known variations (translation, rotation and scale). In order to describe these variations standard techniques to compute statistics such as PCA do not apply, since m-reps are composed by elements of a non-Euclidean space. In fact they belong to a Riemannian symmetric space.

If we recall the definition of a medial atom 2.17, we see that it is composed by $x \in R^3$, the center of the inscribed sphere; $r \in R^+$, the local width defined as the common spoke length; $n_0, n_1 \in S^2$, the two unit spoke directions (here S^2 is the unit sphere in R^3). The medial atom is then a point on the manifold $M(1) = R^3 \times R^+ \times S^2 \times S^2$. Since an m-rep consists of n medial atoms, a single figure may be considered as a point on the manifold $M(n) = \prod_{i=1}^n M(1)$ i.e., the direct product of n copies of $M(1)$.

PGA (principal geodesic analysis) was developed as a generalization of PCA for manifold data. The idea is to project the data onto lower-dimensional subspaces that best represent the variability of the data. Concepts from PCA such as mean, variance, subspace and projection had to be revisited in order to work properly with manifold data. Details of PGA can be found in [Fletcher *et al.* (2004)].

PGA works well for data living on manifolds with spherical components, especially when the data is concentrated on a great circle path since the procedure fits the best great circle to describe these variations. However, m-rep data frequently lives on small circles as the mean computed with PGA is not optimal. A more suitable statistical framework can be developed taking this into consideration.

The following section describes quasi-medial representations or s-reps and the statistical framework to compute shape variations called CPNS (composite principal nested spheres).

2.3.3 Quasi-medial representations

Quasi-medial representations or s-reps [Pizer *et al.* (2012)] differ from m-reps on the strict medialness constraint on every atom, i.e., the position of an atom is not necessarily the center of a maximally inscribed sphere. In s-reps, the atoms are rewarded for being “as medial as possible” but small deviations are tolerated, this means that the spokes can have different lengths; this is done to improve the fit of an s-rep to a given object.

S-reps are continuous objects, defined as a locus of spoke vectors (p, S) with tail at p and tip at $p + S$, also parameterized by (u, v) such that the skeletal sheet is defined as $SS = \{p(u, v) : \forall(u, v) \in [0, 1]\}$, the spokes $SP = \{S(u, v) : \forall(u, v) \in [0, 1]\}$ and the boundary of the object is $BO = \{p(u, v) + S(u, v) : \forall(u, v) \in [0, 1]\}$. The union of tails form the skeletal locus as a fully folded multi-sided sheet, i.e., the top side of the sheet is parameterized by $v \in [0, 0.5]$ and the bottom side by $v \in [0.5, 1]$. Given this definition, every point inside the object can be reached by at least one spoke; special care in the

corners of the object since they are reached by multiple spokes but allow the SS to fold and create the interior filling representation.

The lengths of the spokes are defined as $r(u, v) = |S(u, v)|$ and the directions of the spokes as $U(u, v) = S(u, v)/r(u, v)$. Figure 2.9-a shows a slab figure parameterized by (u, v, τ) . $\tau \in [0, 1]$ is the portion of the spoke length from the SS to the boundary of the object. The s-rep description can be used on tubular objects also. The tube figure is parameterized by (u, ϕ, τ) . Figure 2.9-b shows the interior filling representation of a tubular object.

Section 2.4.3 extends the concept of interior filling objects and the generation of $X2U$ (world coordinates to s-rep coordinates) and $U2X$ (s-rep coordinates to world coordinates) maps.

In a similar manner to m-reps, in the computer, s-reps are represented with a discrete set of atoms. From now on, s-rep is the discrete version of the object. S-reps use the interpolation mechanisms described in [Damon (2003)], [Han *et al.* (2006)], [Damon (2008)] to produce a smooth skeletal locus and a smooth vector field of spokes that generates the boundary of the object. For slab figures, represented as a $m \times n$ grid of atoms, the interpolation defines operators called $S_{rad}(u, v)$ and $S_E(u, v)$, applicable to non-fold medial points (top and bottom side of the sheet without the edges) and to the edge of the figure respectively. The operators are defined as 2×2 matrices that can be computed for each spoke. They describe how the vector $U(u, v)$ moves along and across the field of spokes. To interpolate a spoke at position $(u + \Delta u, v + \Delta v)$ the method uses the eigen-decomposition of the matrices. Damon shows that the object remains legal i.e., the spokes do not cross each other, if and only if for all (u, v) the eigenvalues of $S_{rad}(u, v) < 1/r(u, v)$.

The field of spokes can be retrieved by taking a small Δ step in the (u, v) direction and interpolating the eigenvalues found from the eigen-decomposition of the matrix. The interpolation is done using the neighboring discrete spokes in the quad.

A quad is defined as

$$Q_{i,j} = \{S\left(\frac{i}{n}, \frac{j}{m}\right), S\left(\frac{i+1}{n}, \frac{j}{m}\right), S\left(\frac{i+1}{n}, \frac{j+1}{m}\right), S\left(\frac{i}{n}, \frac{j+1}{m}\right) : i \in [1, n-1], j \in [1, m-1]\} \quad (2.18)$$

At each $(u + \Delta u, v + \Delta v)$ new eigenvalues are calculated that can be turned back into an S_{rad} operator. Integrating S_{rad} from (u, v) at the corner to $(u + \Delta u, v + \Delta v)$ following a straight line, the full swing of the spoke can be computed.

Besides object modeling using the interpolation mechanisms just described, the goal is to produce s-reps suitable for probabilistic analysis. Similarly to m-reps, the MS on an s-rep figure must remain stable through the population of objects. S-reps go through a fitting process to produce the best possible representation for each subject in the population. The procedure has mainly 3 stages to produce the fit. First, the s-rep is aligned to the image; second, each atom is moved around separately to improve the fit; third, the spoke lengths are modified to further match the object's boundary. Further details are given in the following section.

S-rep fitting

The fitting process is done to produce the best geometric approximation of an object using a base s-rep, thus, stabilizing the MS through the population and giving the possibility to compute better statistics afterwards. For the case of s-reps, instead of GPA, CPNS (Composite Principal Nested Spheres) is used.

The s-rep fitting is done on already segmented data, usually provided in the form of a binary image. The image is converted into a signed distance transform [Saboo *et al.* (2011)],

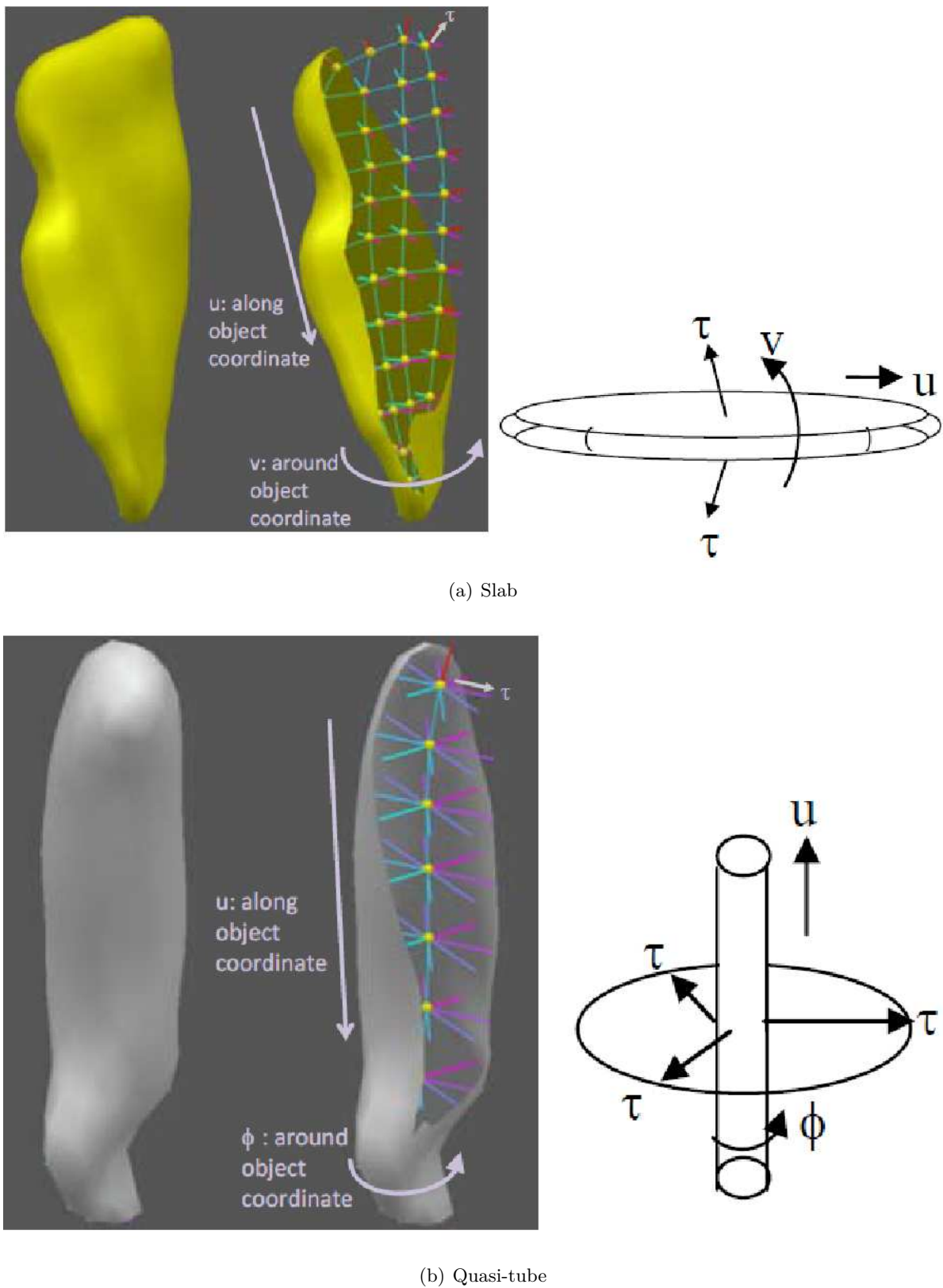


Figure 2.9: Image taken from [Pizer *et al.* (2012)]. S-rep slab, interior filling object. Parameterized by $(u, v, \tau) \in [0, 1]$ every point inside the object can be reached by only one spoke. Similarly a tube figure is parameterized by (u, ϕ, τ) , ϕ is the rotation around the space curve that defines the MA.

with negative values in the interior, 0 at the boundary and positive outside of the object. After the conversion, the fitting starts by aligning the s-rep to the data via matching of moments of boundary positions (zero level on the distance transform) or using landmarks provided by the user.

In the second stage or atom stage, each atom in the s-rep is optimized by measuring how well each of the spokes fits into the distance image $D(x)$ while maintaining the regularity of the grid. In this stage, the only variable affected is the position and orientation of the atom.

In the third stage or spoke stage, each spoke is optimized to produce the best match to the boundary of the object while fixing the tail and changing the angle and length of the spokes.

The following penalties are used to produce the fit:

1. Regularity of the quads (see Equation 2.18 for quad definition).
2. Deviation from medialness using the spokes located at opposite sides of the MS $|r(u, v) - r(u, 1 - v)|$.
3. Deviation of spoke directions from boundary normals $\cos^{-1}(\nabla \hat{D}(x) \cdot U(u, v))$ where $x = p(u, v) + S(u, v)$.
4. Deviation at the crest from the angle between w_2 and $U(u, v) \times U(u, 1 - v)$, where w_2 is orthogonal to the principal curvature direction.
5. Illegality of spoke crossings, i.e., $S_{rad}(u, v) > 1/r(u, v)$

Once the optimization described above is done for every object in the population, correspondence among the cases must be achieved prior to computing statistics using CPNS; this can be done by using the SS that is composed by a set of points $\{p_i\}$ as a PDM. The PDM can be centered at the origin and then scaled by making the sum of the squared distances of the points to the origin equal to 1. The scaling factor of the PDM will be named λ . After the alignment, in order to produce shape statistics, let us analyze the abstract space where an s-rep lives.

S-rep abstract space and composite analysis

An s-rep lives in $R^{n+1} \times S^{3n-4} \times (S^2)^n$. To explain this abstract space, let us define one s-rep composed by n spokes $s_{rep} = \{(p_i, r_i, U_i) | i = 1, 2, \dots, n\}$. This corresponds to the Cartesian product of $n + 2$ manifolds, one of which is Euclidean and the rest are spheres. The Euclidean manifold R^{n+1} corresponds to $n \log r_i$ values plus the scaling factor of the PDM ($\log \lambda$). The spherical manifolds are the S^{3n-4} corresponding to the PDM and the $(S^2)^n$ are for the n spoke directions.

In order to study a population of s-reps and knowing that they are composed by elements on different manifolds, each one of them is analyzed separately at first.

PNS (principal nested spheres) [Jung *et al.* (2012)] allows estimating the principal modes for each non-Euclidean component and produces Euclidean scores (see Appendix B). All of the scores are composed on a matrix that contains Euclidean data only, thus, making possible to do further analysis using PCA. The composite matrix Z_{comp} is shown in Equation 2.19, where N is the number of s-reps and $*$ means that the mean has been subtracted from the variable.

Sphere 0: Scaled medial points	$\begin{bmatrix} z_{1,1}^t & \cdots & z_{1,N}^t \\ \vdots & \ddots & \vdots \\ z_{N-1,1}^t & \cdots & z_{N-1,N}^t \end{bmatrix}$	$\begin{bmatrix} \bar{\lambda} \\ \vdots \\ \bar{\lambda} \end{bmatrix}$	(2.19)
Spheres 1 - n: Spoke directions	$\begin{bmatrix} z_{1,1}^{S_1} & \cdots & z_{1,N}^{S_1} \\ \vdots & \ddots & \vdots \\ z_{n,1}^{S_n} & \cdots & z_{n,N}^{S_n} \end{bmatrix}$	$\begin{bmatrix} \bar{r}_1 \\ \vdots \\ \bar{r}_n \end{bmatrix}$	
Euclidean variables: Scaling	$\begin{bmatrix} \log_{\lambda_1}^* & \cdots & \log_{\lambda_N}^* \end{bmatrix}$	$\begin{bmatrix} \bar{\lambda} \\ \vdots \\ \bar{\lambda} \end{bmatrix}$	
Spoke lengths	$\begin{bmatrix} \log_{r_{1,1}}^* & \cdots & \log_{r_{n,N}}^* \\ \vdots & \ddots & \vdots \\ \log_{r_{n,1}}^* & \cdots & \log_{r_{n,N}}^* \end{bmatrix}$	$\begin{bmatrix} \bar{r}_1 \\ \vdots \\ \bar{r}_n \end{bmatrix}$	
	$\xleftarrow{\text{Cases}}$	$\xrightarrow{\text{Scaling}}$	

CPNS produces a set of eigenmodes that can be used to approximate any of the shapes in the population (see Appendix A). This results in a vector that lives in Euclidean space equivalent to the Z_{comp} matrix. Using this vector, each of the Euclidean components are ready to be mapped back to their corresponding spheres by adding the mean value computed at the PNS analysis.

We have seen that it is possible to compute robust statistics for 3D shape objects using medial representations. The following section explains the implementation based on the concepts seen for medial representations.

2.4 Object modeling using s-reps

The srep implementation done for this dissertation defines the interpolation mechanisms similar to [Han *et al.* (2006)].

2.4.1 MS interpolation

The interpolation is done with cubic Hermite splines. To produce the interpolation, the partial derivatives for every atom on the SS, and the normal must be defined.

Let $s_{rep} = \{(p_i, S_i) : i \in N\}$ and $N = m \times n$, represent a discrete grid of atoms. The interpolation is done using the four control points from each quad in the grid.

Equations 2.20 and 2.21 shows how to compute the partial derivative for a given atom in the u and v direction on the SS. $\Delta u = 1/m$ and $\Delta v = 1/n$ correspond to a step length. $u + \Delta u$ moves along the u direction onto the next atom on the discrete grid, and similarly for the v direction.

$$\partial p(u, v)_u = \begin{cases} p(u + \Delta u, v) - p(u, v) & u = 0 \\ (p(u + \Delta u, v) - p(u - \Delta u, v))/2 & 0 < u < 1 \\ p(u, v) - p(u - \Delta u, v) & u = 1 \end{cases} \quad (2.20)$$

$$\partial p(u, v)_v = \begin{cases} p(u, v + \Delta v) - p(u, v) & v = 0 \\ (p(u, v + \Delta v) - p(u, v - \Delta v))/2 & 0 < v < 1 \\ p(u, v) - p(u, v - \Delta v) & v = 1 \end{cases} \quad (2.21)$$

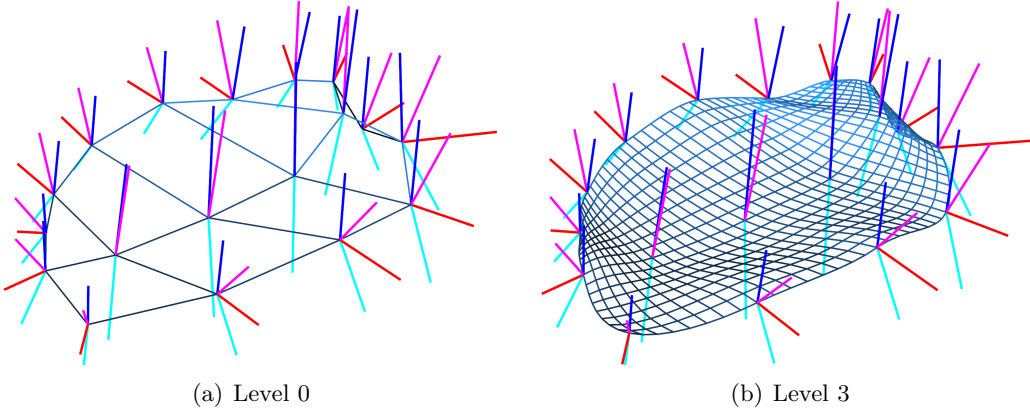


Figure 2.10: MS interpolation for a slab type s-rep. The top spoke is shown in magenta, the bottom spoke in cyan, the crest spoke in red, the MS is shown in light blue and the normal to the sheet is shown in blue.

Equation 2.22 gives an approximation to the normal of an atom to the SS. The normal is computed from opposite spokes with tail at equal position on the SS. More precisely, N is normal to the SS if the two spokes are exactly boundary normals and have the same length.

$$N(u, v) \approx \frac{S(u, v) - S(u, 1-v)}{\|S(u, v) - S(u, 1-v)\|} \quad u \in [0, 1], v \in [0, 0.5] \quad (2.22)$$

$$H_{control} = \begin{bmatrix} p_{11} & p_{12} & \partial p_{11v}^T & \partial p_{12v}^T \\ p_{21} & p_{22} & \partial p_{21v}^T & \partial p_{22v}^T \\ \partial p_{11u}^T & \partial p_{12u}^T & h_0 & h_0 \\ \partial p_{21u}^T & \partial p_{22u}^T & h_0 & h_0 \end{bmatrix} \quad (2.23)$$

To interpolate the SS, a Hermite matrix patch is defined in equation 2.23, where $\partial p(u, v)^T = \partial p(u, v) - (\partial p(u, v) \cdot N(u, v))N(u, v)$ is the projection of the discrete derivatives in directions u or v onto the tangent planes that are determined by the normals $N(u, v)$, so the MS interpolation depends on the normals and the discrete derivatives; h_0 is a vector filled with 0.

$$\begin{aligned} H_1(s) &= 2s^3 - 3s^2 + 1 \\ H_2(s) &= -2s^3 + 3s^2 \\ H_3(s) &= s^3 - 2s^2 + s \\ H_4(s) &= s^3 - s^2 \end{aligned} \quad (2.24)$$

$$p(u, v) = \begin{bmatrix} H_1(\hat{u}) & H_2(\hat{u}) & H_3(\hat{u}) & H_4(\hat{u}) \end{bmatrix} H_{control} \begin{bmatrix} H_1(\hat{v}) \\ H_2(\hat{v}) \\ H_3(\hat{v}) \\ H_4(\hat{v}) \end{bmatrix} \quad (2.25)$$

The interpolated position for any atom on the SS is shown in equation 2.25, using a Hermite matrix control patch and the weight functions defined in 2.24. $\hat{u} = (u - floor(u))/\Delta u$, where $floor(u)$ returns the u coordinate of the atom at p_{11} , similarly for \hat{v} , notice that every patch is interpolated by varying $(\hat{u}, \hat{v}) : 0 \rightarrow 1$. Figure 2.10 shows the interpolation of the MS at different levels for the same figure.

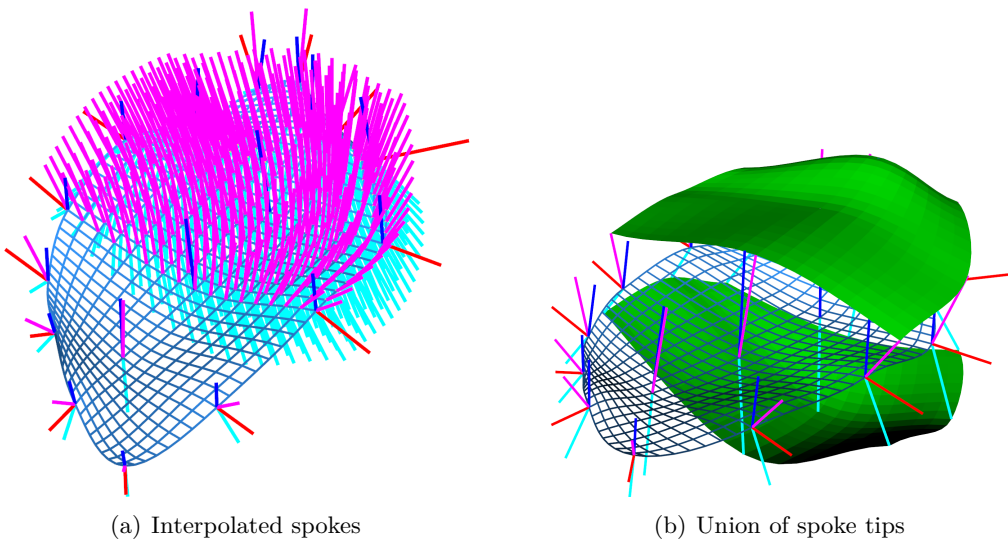


Figure 2.11: Top and bottom surfaces interpolated for a given atom. The surfaces are generated from the spoke interpolation.

In a similar manner, the spoke interpolation can be done using Hermite basis functions. Instead of using the control points $p(u, v)$, the spokes $S(u, v)$ are used. Accordingly, the discrete derivatives are computed for each spoke, the difference in this case is that no projection is done using the normals to the SS; the spoke interpolation only depends on the discrete derivatives.

The top and bottom surface can be generated using the mechanisms described above. Figure 2.11 shows the implied surface generated by the union of interpolated spoke tips. As mentioned before, both surfaces meet at the crest of the object, Section 2.4.2 explains how to perform the crest interpolation which can also be used to interpolate tubular figures.

2.4.2 Crest interpolation

For the crest interpolation, we wish to fit a surface that does not collapse towards the interior of the object. In other words, its cross-section should be convex in the principal direction and preserve C^2 continuity. Another property of the surface is that the directional derivatives computed for every spoke should be matched in order to produce a smooth surface to the Hermite based interpolation previously explained.

The crest interpolation method is explained by showing how to interpolate the lengths r of a spoke that sweeps according to an angle θ . The function $r(\theta)$ returns the length at a given angle. In a similar way, we wish to interpolate the cross-section in the crest, where theta runs between the terminus of the top or bottom spoke to the crest spoke.

The same problem can be extended to 3 dimensions where the interpolation produces a space curve. In order to produce an interpolated surface the interpolation of the cross-section sweeps along the skeletal sheet.

$$\frac{\partial^2 r(\theta)}{\partial \theta} = q_0 + q_1 \theta + q_2 \theta^2 \quad (2.26)$$

The first step is to define a quadratic function of the curvature, as shown in Equation 2.26, we would like to enforce convexity in the interpolated curve. By integrating this equation twice, we find the function that gives us the length for $\theta \in [0, \theta_{max}]$.

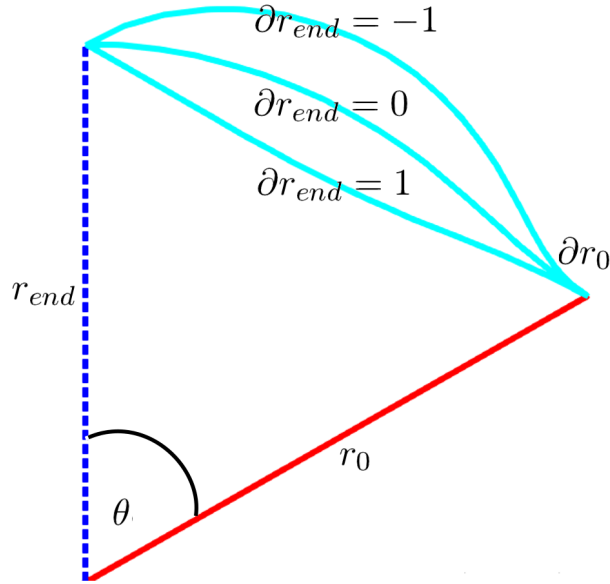


Figure 2.12: Radius interpolation showing the result for different ∂r_{end} .

$$\frac{\partial r(\theta)}{\partial \theta} = \int_0^{\theta_{max}} \frac{\partial^2 r(\theta)}{\partial \theta^2} d\theta \quad (2.27)$$

$$\frac{\partial r(\theta)}{\partial \theta} = \frac{\partial r_0}{\partial \theta} + q_0 \theta + \frac{1}{2} q_1 \theta^2 + \frac{1}{3} q_2 \theta^3 \quad (2.28)$$

$$r(\theta) = \int_0^{\theta_{max}} \frac{\partial r(\theta)}{\partial \theta} d\theta \quad (2.29)$$

$$r(\theta) = r_0 + \frac{\partial r_0}{\partial \theta} \theta + \frac{1}{2} q_0 \theta^2 + \frac{1}{6} q_1 \theta^3 + \frac{1}{12} q_2 \theta^4 \quad (2.30)$$

We start by solving for coefficients q_1 and q_2 , using the system of equations $r(\theta)$, $\partial r(\theta)/\partial \theta$ and $\partial^2 r(\theta)/\partial \theta^2$, as shown in equation 2.32.

$$q_2 = \frac{6}{\theta_{max}^4} (2\partial r_{end} \theta_{max} + q_0 \theta_{max}^2 - 6r_{end} + 6r_0 + 4\partial r_0 \theta_{max}) \quad (2.31)$$

$$q_1 = \frac{-6}{\theta_{max}^3} (-\partial r_{end} + r_0 + \partial r_0 \theta_{max} + \frac{q_0}{2} \theta_{max} + \frac{q_2}{12} \theta_{max}^4) \quad (2.32)$$

There exists a solution to the problem for every q_0 but the optimal solution is found when q_0 minimizes the average 2nd derivative of r as shown in Equation 2.34.

$$\partial r_{end} = -1 \quad \partial r_{end} = 0 \quad \partial r_{end} = 1 \quad r_0 \theta \partial r_0 \quad (2.33)$$

$$\hat{q}_0 = \arg \min_{q_0} \sum_{\theta=0}^{\theta_{max}} \frac{\partial^2 r(\theta)}{\partial \theta^2} \quad (2.34)$$

Notice that the parameters r_0 , r_{end} , ∂r_0 and ∂r_{end} correspond to initial and final lengths, and rates of the change at r_0 and r_{end} respectively.

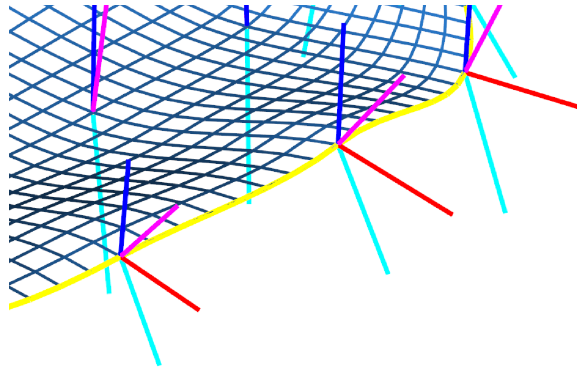


Figure 2.13: The interpolated crest curve is shown in yellow, using the crest positions to compute the directional derivatives and projecting the derivatives onto the tangent plane.

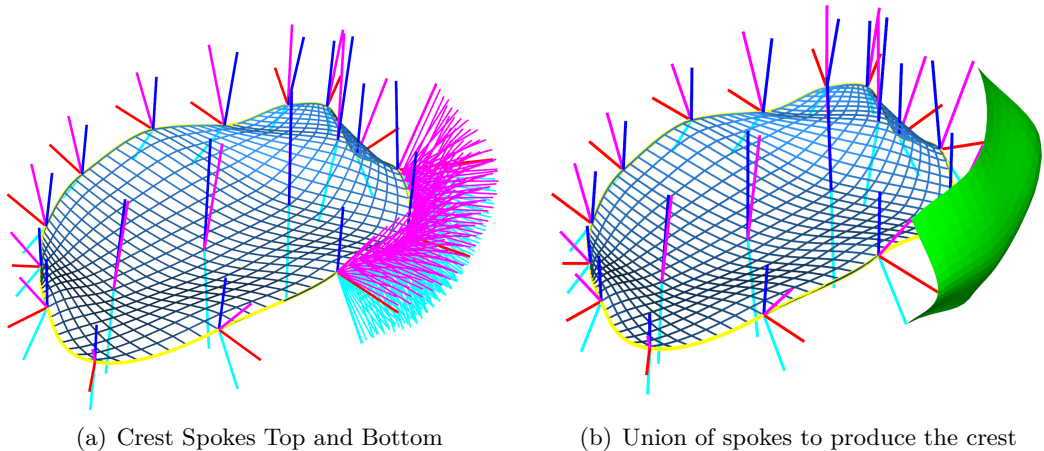


Figure 2.14: The method interpolates top, crest and bottom spokes separately. A second interpolation is produced using the interpolated top, crest and bottom spokes in order to join both sides of the object at the crest.

To produce space curves, the fitting is done for $[x, y, z]$ separately. Using the discrete information given by the s-rep, it is possible to retrieve p_0 , p_{end} , and compute the discrete derivatives ∂p_0 , and ∂p_{end} which are the parameters to produce the fit. To produce the crest curve, the crest atoms are considered to be on a loop where the crest positions are given by cp_n where n is the number of crest positions. The directional derivatives are calculated as $\partial cp_j = (cp_{j+1} - cp_{j-1})/2$ which are projected onto the tangent plane given by the SS normal at each atom $\partial \hat{cp}_j = \partial cp_j - (\partial cp_j \cdot N_{cp_j})N_{cp_j}$. Figure 2.13 shows the interpolated crest as a space curve.

The same interpolation mechanism is used for top, crest and bottom spokes, therefore, for a given t , it is possible to find the top spoke $CS(t)^1$, the crest spoke $CS(t)^0$ and the bottom spoke $CS(t)^{-1}$ plus the space curve to find the positions $Cp(t)$ where $t \in [0, 1]$ goes around the whole crest of the object.

Finally we perform a second interpolation to generate the spokes from *top* \rightarrow *bottom*, which allows us to produce the interpolated crest. Figure 2.14 shows the interpolated spokes and the union of spokes forming a piece of the crest surface. Figure 2.15 shows an example of the interpolated surface of an amygdala and the crest that joins both surfaces.

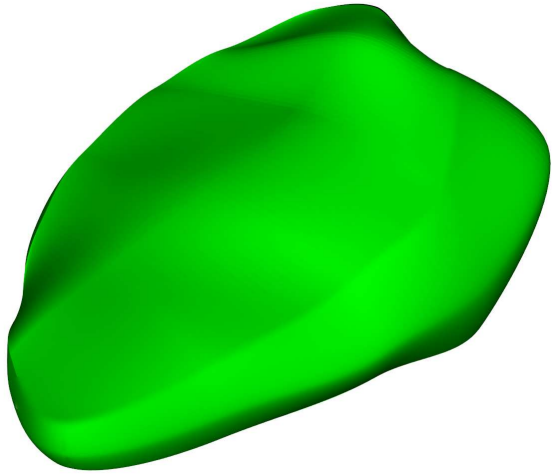


Figure 2.15: Complete s-rep of an amygdala, with top, bottom and crest surfaces. The level of interpolation is higher to produce a smoother boundary.

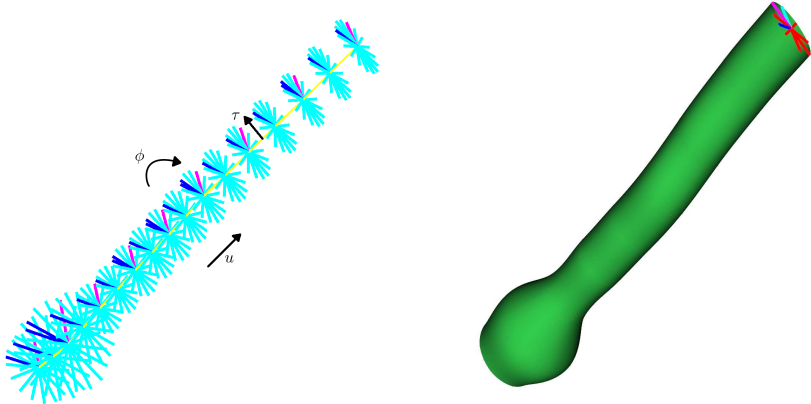
Tubular objects

Different organs in the human body, such as blood vessels, the airways, and the intestines among many others are best represented using tubular structures. Representing these objects with slab type s-reps is more difficult, because SS cannot be oriented in an intuitive manner. Instead, a parameterized space curve provides a more stable representation of a SS. Prominent authors such as [Binford (1971)] proposed generalized cylinders, this method consists of a space curve, or axis, and a cross section function defined on the axis. For example, the function may be an ellipse. Another approach is the one proposed by [Huang and Stockman (1993)] named generalized tubes. It is a two step approach, to segment and model tubular structures. It starts with a local contour detection followed by a global recognition stage where the tube figures from the first stage are verified. Such tube figures have been widely used on segmentation and modeling procedures, but unfortunately, it is not trivial to include shape statistics using the approaches mentioned before; such structures are best conceived to model individual tubes and not a population of them. For this reason the tubular model proposed here is closely related to quasi-tubes, a model proposed by [Saboo *et al.*].

Figure 2.16 shows the result of the interpolation using the same formulation from the crest method. These quasi-tubes are defined in the same manner as s-reps, $S_{rep} = \{p_i, S_i\}$; the difference is that the spokes are all placed following a space curve that defines the MA, and the interpolation is done with the spokes that share the same hub. They are differentiated by the angle ϕ from the spoke located at $\phi = 0$ which is highlighted in magenta.

Since the definition of this tubular object is equivalent to the definition of an s-rep, the statistical framework CPNS is also compatible. However, tubular objects are not widely used in this dissertation and will be reserved for future work.

The last subject that is addressed on geometric representation is the internal coordinates of an object.



(a) Interpolated spokes of a tube figure, (b) The union of spoke tips produce the MA is shown in yellow and the spokes boundary of the tubular object in cyan. The MA is parameterized by a single parameter u , while the spokes on the MA are parameterized by (u, ϕ) , τ represents the portion of the spoke from the MA to the boundary.

Figure 2.16: The crest interpolation method is also capable of interpolating tube figures.

2.4.3 Internal coordinates of an object

The internal coordinates of an object are described by $X2U$ maps. The mapping enables querying world coordinates to find object coordinates. $X2U$ maps will be used in Chapter 5 to map the solids generated in Chapter 4 to an s-rep. This is possible since the solids are synthesized in a cube. Each coordinates in the cube can be related to $[u, v, \tau]$, thus, providing a simple mechanism to map a solid to an object.

The amygdala shown in Figure 2.15 is composed by 18 atoms placed on a double sided grid $(m, n) = (6, 3)$, where every spoke's tail is placed. The total number of spokes is 26 and in order to give a unique coordinate to every spoke, the MS is unfolded.

Figure 2.17 shows a representation of the unique (u, v) coordinate given to every spoke in the object, they are represented by the color gradient using red for the u direction and green for the v direction. The blue color is used to represent the spoke length which is $\tau = 0$.

By means of the mechanisms described to interpolate the MS, top, bottom and crest spokes, a function $U2X(u, v, \tau) = [x, y, z] | (u, v, \tau) \in [0, 1]$ is designed to retrieve a position inside the object by querying (u, v, τ) coordinates. This function is used to calculate the $X2U$ map.

Figure 2.18 shows the $X2U$ map of the amygdala.

2.5 Conclusions

We have seen different types of approaches to model the boundaries of objects and produce statistics on their shape. It has been shown that deformable models behave better and increase the accuracy of segmentation procedures or object recognition. They are less sensitive to noise and are more likely to find the global optimal object boundary. Two major components in probabilistic deformable model methods are learning shape statistics and the segmentation of target images using the statistical probability distributions. There is

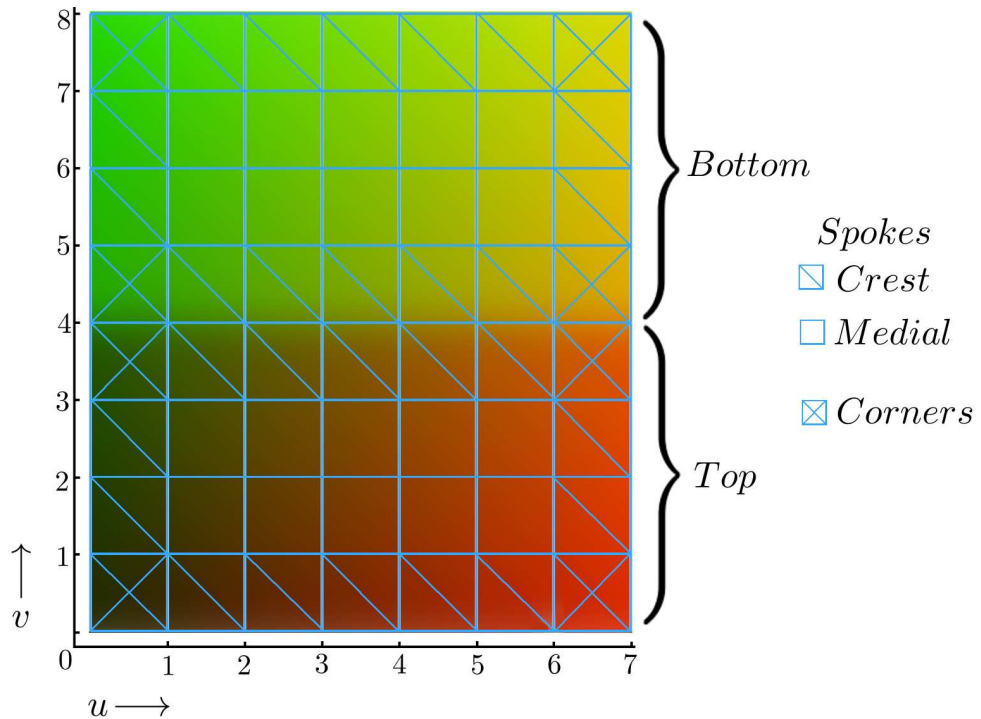


Figure 2.17: Unfolded s-rep of 6×3 atoms. Each intersection corresponds to a spoke in the s-rep, the crest spokes repeat them selves on the top and bottom sides. The corners of the object are shown with the blue cross, they also correspond to the 4 crest spokes that join top, bottom and connect the sides of the object. Using this unfolded version of the MS we provide a unique u, v value represented by the color gradient, the grid size is $(m + 1) \times 2 \times (n + 1)$.

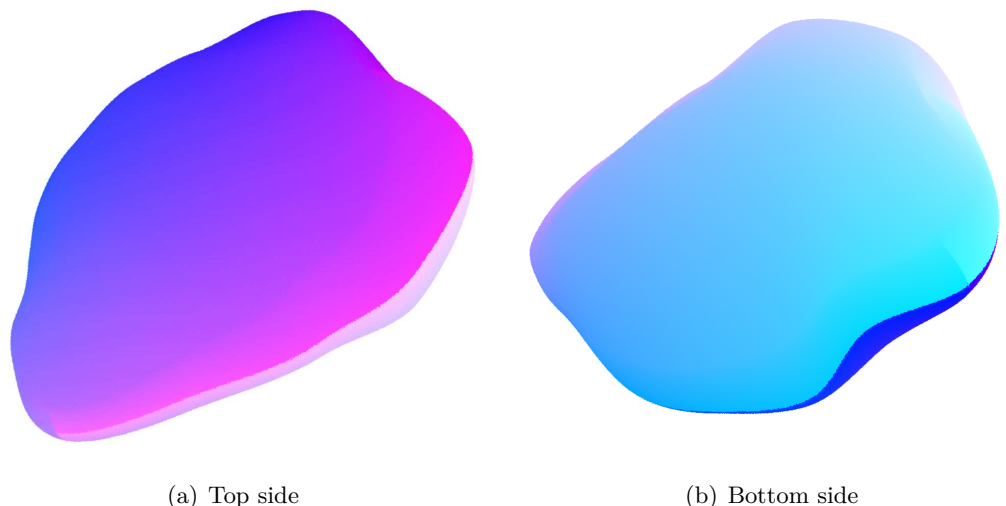


Figure 2.18: Volume rendering of an $X2U$ map showing both sides when $\tau = 1$

still more improvement to be done at the training stage of the deformable model because this step requires too much user intervention and is time consuming.

Besides surface modeling, a summary on 3D modeling techniques has been given. Those models are best suited to describe the internal features of 3D objects. S-reps in particular are able to explain the continuum of space in an object, giving possibilities to include information into the model in a multi-scale fashion. The continuum of space described by the s-reps will be used to include the necessary parameters to perform MRI simulation.

Furthermore, s-reps are suited to produce shape statistics with CPNS and can describe shape variations with a few coefficients, a mean shape and eigenmodes of shape variation.

The following chapter explains a novel methodology to fit s-reps to the brain cortex because they also support foldability. With the fitted structure a statistical analysis is conducted using CPNS proving that s-reps are well suited to model complex structures.

3

Cortex modeling via s-reps

3.1 Introduction

The cerebral cortex is a highly folded slab of neural tissue with compact interconnections that enables sophisticated processing of information. It plays an important role in memory, attention, perceptual awareness, thought, language, and consciousness. Progress has been made in understanding the structure and function of the cortex. [Lorente de Nó (1934)] proposed that the cortex is formed by small cylinders containing vertical chains of neurons; These structures were later called columns, corresponding to groups of local cells running perpendicular to the cortical surface. This hypothesis was later confirmed with the physiological studies done by [Mountcastle (1998)].

The cortex is a layered sheet with a more or less uniform cellular structure. It is composed by the following layers:

1. Layer I (molecular layer): apical dendrites of cells and axons;
2. Layer II (external granular layer): small granule cells and some larger pyramidal cells;
3. Layer III (external pyramidal layer): small to medium sized pyramidal neurons;
4. Layer IV (Internal granular layer): interneurons receiving ascending sensory input and projecting to layers II/III. No pyramidal neurons are found in this layer;
5. Layer V (Internal pyramidal layer): medium to very large pyramidal neurons;
6. Layer VI (Multiform layer): assortment of cell types including pyramidal cells, cells that receive input from layers II, III and V and axons projecting to superficial cortical layers and subcortical regions.

Today the columnar organization is the most widely adopted model to explain the cortical processing of information.

Figure 3.1 shows a slice of an MRI with the cortex region outlined. In brown the grey matter (GM) and in green the white matter (WM) surfaces are shown. Since nearly two thirds of the cortical surface is buried within the sulci, it is difficult to perform computation and visualization tasks. Different procedures have been developed to unfold and map the cortical surface onto different spaces (inflated, spherical or flattened) [Drury *et al.* (1996)], [Hermosillo *et al.* (1999)], [Fischl *et al.* (1999)], [Pons *et al.* (2004)]. This allows the cortical surface to be analyzed and visualized and statistical methods to be applied on these



Figure 3.1: Brain MRI. The grey and white matter surfaces are shown in brown and green respectively.

spaces. *Freesurfer* (an automated tool for brain's cortical surface reconstruction using structural MRI data) uses the inflation and flattening procedure from [Fischl *et al.* (1999)].

Likewise, cortex evolution has also been a subject of great interest. Much of the efforts have been focused on understanding how the folding process occurs. Many species have folded cortices, but the degree of folding is different among them. In general terms, a greater degree of folding is related to higher intelligence [Buettner-Janusch (1964)]. Humans have extremely folded cortices. The folding patterns are unique to each brain, and abnormal folding is related to neurological disorders such as schizophrenia, epilepsy, autism and Down's syndrome. Different methods have been proposed to explain how the folding occurs: growing a 2D curve in a closed space [Raghavan *et al.* (1997)]; growing 2D and 3D truss elements constrained by radially aligned fibers [Toro and Burnod (2005)]; using spherical wavelets on close surfaces [Yu *et al.* (2007)]; using a FEM (finite element method) biomechanical model [Geng *et al.* (2009)]; combining a mathematical model with biomechanical data [Bayly *et al.* (2013)]. For a recent review on folding theories see [Filas *et al.* (2013)].

There are research opportunities in developing cortex models. As stated by Javier de Felipe [Defelipe *et al.* (2012)], “it is still necessary to achieve a better fundamental understanding of what columns are and how they are used in cortical processes. Accordingly, it is now important to translate recent technical advances and new findings in the neurosciences into practical applications for neuroscientists, clinicians, and for those interested in comparative anatomy and brain evolution.”

Taking these facts into consideration, one of the objectives in this dissertation is to provide a tool that models the shape of the cortex and relates to the real physical structure. Section 2.4 defines an s-rep with the corresponding interpolation mechanisms that parameterize the interior of the object by $[u, v, \tau]$. S-reps can be used to model the anatomic and physiologic information from the different layers of the cortex. This information can be naturally included using the τ coordinate.

Figure 3.2 shows how an s-rep fits into the cortex.

Besides shape description, s-reps have been used successfully to compute shape statis-

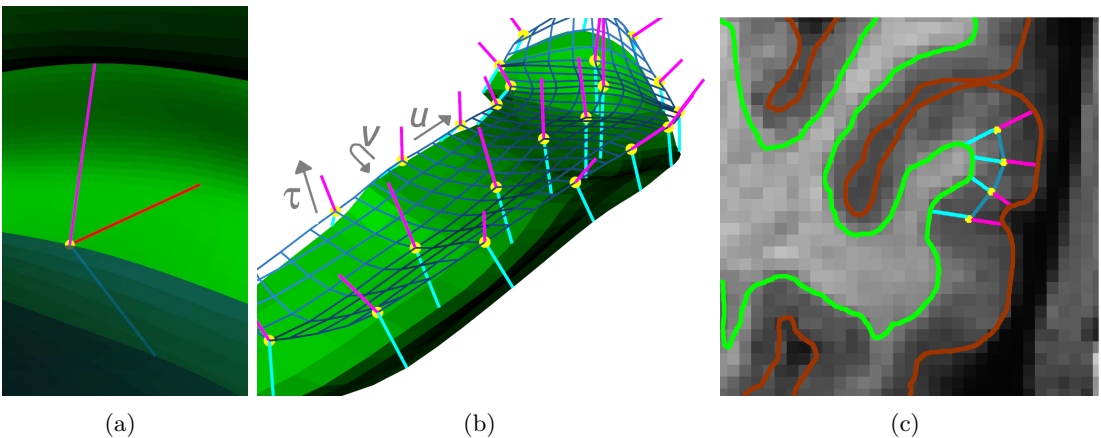


Figure 3.2: Figure (a) shows a close up of an atom represented as the yellow ball with its corresponding spokes, top (magenta), bottom (cyan), crest (red). The s-rep on figure (b) shows the quasi-medial surface in wireframe representation (blue), with the sampled atoms. The MRI image on figure (c) shows a cross-section of the skeletal locus of the cortex and some atoms with the corresponding top and bottom spokes.

tics and mean shapes from a population of objects. With this statistical description, it appears to be possible to classify objects by shape frequently more accurately than any other method. S-reps model single non-branching objects, and tubular objects, as explained in Section 2.3.3. The objects modeled with s-reps until now are simple as most of them have a blob-like or elongated shape structure like the hippocampus [Pizer *et al.* (2012)].

It is demonstrated that s-reps are suited to represent a folded complex structure such as the cortex. The sheet of the object does not branch and captures the majority of the folds in the cortex. Moreover, a statistical analysis of shape variability is done using the s-rep description of the cortex.

The following section explains how to create an s-rep of the cortex from an MRI image. The procedure uses a spherical representation of the cortex [Fischl *et al.* (1999)] that relates the WM and the GM surfaces to the sphere. Folding the s-rep into the cortex is done by projecting the SS (skeletal sheet) of the s-rep on the sphere and using the relationship of the sphere and the cortical surfaces. The following section explains in detail the procedure to create an s-rep of the cortex. With the skeletal figure inside the cortex, top and bottom spokes point towards the GM and WM surfaces respectively. The interpolation mechanisms of the s-rep allows reconstructing the GM surface and the WM surface. Section 3.3 evaluates the quality of the interpolated surfaces. Finally, a population of cortex s-reps is generated, and a statistical analysis is made in Section 3.4 using CPNS (Composite Principal Nested Spheres, which is described in Appendix B).

3.2 Acknowledging the true shape of the cortex

The cortex is a highly folded sheet. It has thickness that varies through the cortical regions. Unfortunately, the cortex is often represented using surfaces and is difficult to represent interior features. To acknowledge its true shape which is similar to a folded pancake, a procedure to create an s-rep of the cortex is proposed. As shown in Figure 3.3, the procedure has five steps:

- (a) A mapping of the cortex on a sphere is done using the method from

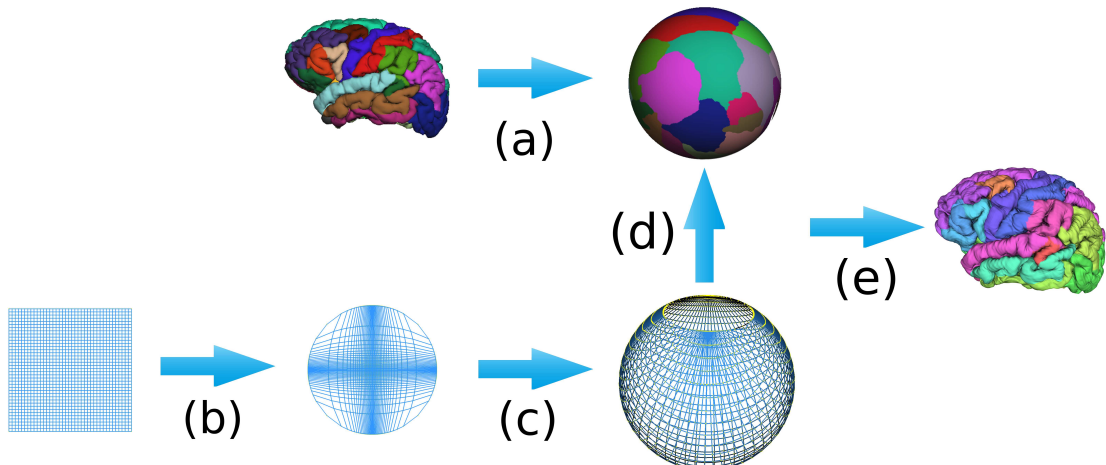


Figure 3.3: (a) Inflation of the cortex by *Freesurfer* and rotation of the sphere to the north using the points in the corpus callosum. (b) Transformation of a base s-rep into a circle. (c) Transformation of the circle into a sphere. (d) Fitting the s-rep to *Freesurfer*'s data on the sphere. (e) Folding the SS of the s-rep inside the the cortex and determine the widths of the slab.

- [Fischl *et al.* (1999)]. The sphere is rotated to the north using the corpus callosum.
- (b) A regular grid or the SS of a base s-rep is transformed into a 'circular log-grid'.
- (c) The 'circular log-grid' is transformed into a sphere (with a spherical cap oppening in the north pole).
- (d) The SS on the sphere is fitted to the mapping of the cortex on the sphere.
- (e) The SS is folded back into the shape of the cortex. During the folding procedure, the widths of the slab or the thickness of the s-rep is determined.

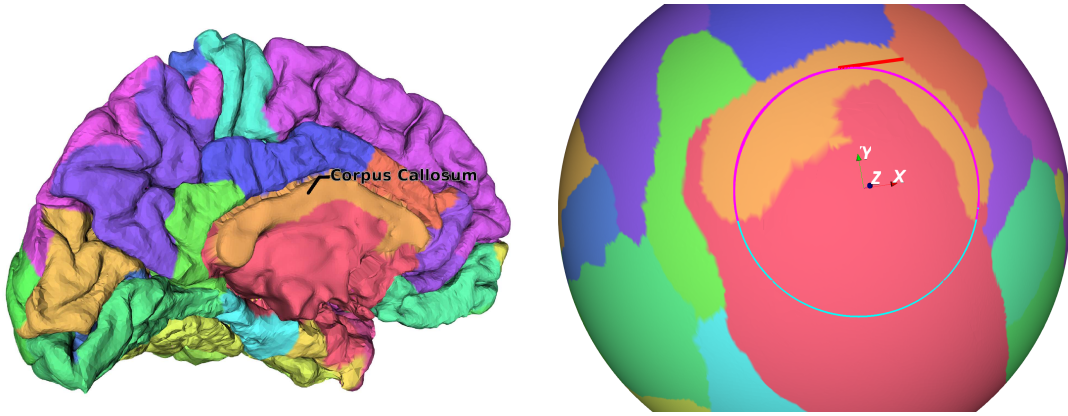
The following sections explain the details of each step and shows how to create an s-rep of the cortex.

3.2.1 Spherical representation of the cortex by *Freesurfer* and rotation

The materials used in this study are 8 MRI scans acquired at "CERMÉP - Imagerie du vivant" on a Siemens Sonata system with a 1.5 T magnet, with gradients of 40 mT/m and an 8-channel head coil. The overall protocol includes anatomical acquisitions, spectroscopy and diffusion.

In this study, only T1-weighted anatomical images are considered. The 8 datasets were obtained by the acquisition of millimetric sagittal slices from a 3D T1-weighted MPR sequence (repetition time (TR) = 1880 ms, echo time (TE) Ms = 4). The total acquisition time of each of these anatomical images was done in 18 minutes.

All the datasets were segmented using *Freesurfer*. The method proposed by [Fischl *et al.* (1999)] creates a spherical representation of the cortex. It removes the folds from the surface using an energy functional with a distance term for unfolded or positive regions. An unfolded region is recognized by calculating the normal direction and the ordered cross-product of the triangle legs for every face in the surface tessellation. If the resulting vector is anti-parallel to the normal direction, a negative area is assigned.



(a) The internal part of the left hemisphere of the cortex. The corpus callosum is shown in the figure. The points that compose the corpus callosum are used in the minimization procedure.

(b) Spherical representation of the left hemisphere. The best fitting circle is shown in cyan and the projected points on top of the circle in magenta. The center of the circle is aligned with the north pole.

Figure 3.4: The inflation procedure maps the cortical surface onto a sphere. The best fitting circle is found using the points of the corpus callosum.

The folds from the surface are eliminated when the area is constrained to be positive everywhere. After the inflation procedure, the cortical surface has spherical topology. A mapping of the cortex is made onto a sphere providing a 1 – 1 relationship for every point on the cortical surface and spherical mapping.

The procedure to build the s-rep of the cortex uses a modified stereographic projection. The stereographic projection [Snyder (1987)] was probably known to the Egyptians in its polar form, but Hipparchus (2nd Century B.C) was apparently the first Greek to use it, so he is considered its inventor. Ptolemy referred to it as “Planisphaerum”, the name stereographic was given by François d’Aiguillon in 1613. The stereographic projection enables a mapping of the points on a plane to the sphere and it has two properties that should be treated carefully: the scale increases away from the center of the projection, and the point opposite to the center of the projection cannot be plotted (north pole).

The first step to do a stereographic projection is to choose the north pole. The north pole of the sphere cannot be mapped by the stereographic projection because it maps to infinity. For this reason, the representation must have a spherical cap opening in the north pole.

The corpus callosum is a brain structure located beneath the cortex. It facilitates interhemispheric communication with a bundle of 200-250 million fibers for this task. Figure 3.4 displays the corpus callosum. This brain structure is used to find the north pole. The points in the corpus callosum are used in a fitting procedure that minimizes the geodesic distance from each point to a circle. The center of the best fitting circle is chosen to be the north pole.

To find the best circle for a set of points in a sphere, a method similar to [Jung *et al.* (2012)] is used. A circle on the sphere S^2 is defined by a vector v_1 and a distance $r_1 \in (0, \pi/2]$ as in equation 3.1, where ρ_d is the geodesic distance function.

$$C(v_1, r_1) = \{x \in S^2 : \rho_d(v_1, x) = r_1\}. \quad (3.1)$$

The best fitting circle is found with a least squares minimization that uses the geodesic distance as follows: let $CC = \{x_i : i \in N\} \in S^2$ be the points of the corpus callosum on the sphere. We first define the residual ε of x_i from a circle $C(v_1, r_1)$ of S^2 as the signed

length of the minimal geodesic that joins x_i to C . Then $\varepsilon = \rho_d(v_1, x) - r_1$. The sign of ε is negative if x_i is in the interior of C , and is positive if x_i is in the exterior. The best fitting circle $\hat{C} \equiv C(\hat{v}_1, \hat{r}_1)$ is found by minimizing the sum of squares of residuals of the data points to C . In other words v_1 and r_1 minimize Equation 3.2.

$$\hat{C} = \operatorname{Arg\,min}_{v_1, r_1} \sum_{i=1}^n \varepsilon_i(v_1, r_1)^2 = \operatorname{Arg\,min}_{v_1, r_1} \sum_{i=1}^n \{\rho_d(x_i, v_1) - r_1\}^2 \quad (3.2)$$

Once the center of the circle is found, a rotation is done to align its center to the north pole. Figure 3.4 shows the corpus callosum and a spherical representation of the cortex with the best fitting circle.

The following section explains how to modify the s-rep to produce the best possible mapping on the sphere. The projection to the sphere is explained in Section 3.2.3.

3.2.2 Transforming the s-rep into a circular log grid

An s-rep is built using a grid of sampled points where each intersection is a hub or atom of the s-rep. An atom is defined as a sampled point on the SS or quasi-medial surface of the object as shown in Figure 3.2-a.

To generate the s-rep of the cortex, the structured collection of atoms (the grid) is mapped on a sphere. This mapping is equivalent to the mapmakers problem, *i.e.*, to map two surfaces with different Gaussian curvatures. This was shown to be impossible by Gauss in 1828. To lower the distortion effects of the projection and allow the construction of the s-rep, the grid of the s-rep is modified. This is done to improve the sampling of the hubs on the sphere while preserving the grid topology.

Relating the points from the plane to the sphere is the key to produce the s-rep of the cortex. Each projected hub can be related to the spherical representation of the cortex provided by *Freesurfer*.

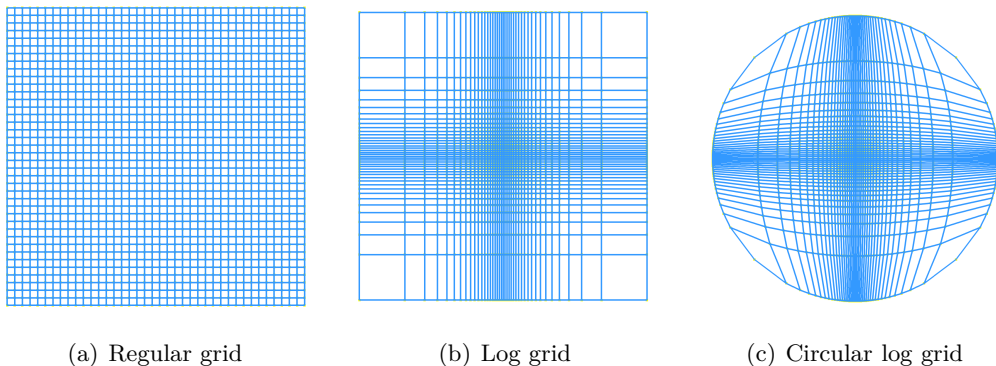


Figure 3.5: An s-rep is represented with a grid of points. If the regular grid is projected on the sphere a distortion effect is produced by the stereographic projection. In order to lower the distortion effects, the grid is resampled using a log function. The transformation into a circle is done to match the s-rep to the best-fitting circle of the corpuscallosum.

An s-rep is represented by a regular grid on a plane. Mapping a regular grid on the sphere causes a distortion since the majority of the hubs will map towards the north pole (first property of the stereographic projection). To produce the best s-rep of the cortex and capture accurately the geometry of the folds, the hubs should be spaced evenly on the sphere.

To attain a regular spacing of the hubs, a log function is used to resample the position of the hubs in the grid. Figure 3.5 shows how the log function maps more points towards the center of projection.

$$S(x) = \begin{cases} Min + x * (\frac{Max-Min}{N/2}), & x < \frac{N}{2} \\ Min + (N - x) * (\frac{Max-Min}{N/2}), & otherwise \end{cases} \quad (3.3)$$

$$L(S(x)) = \begin{cases} \frac{\log(S(x))}{\log(Min)}, & x < \frac{N}{2} \\ -\frac{\log(S(x))}{\log(Min)}, & otherwise \end{cases} \quad (3.4)$$

Equations 3.3 and 3.4 show how to transform the regular grid. Each hub $(x, y) \in [0, N-1]$ is distributed regularly with $S(x) \in [Min, Max]$ where N is the number of points for one side of the grid, $Min \in (0, Max)$, and Max is always set to 1. $L(S(x)) \in [-1, 1]$ moves the points towards the center of projection (south pole). Having an increased number of points near the center reduces the distortion effects produced by the stereographic projection.

Finally, to further improve the projection of the grid on the sphere, the grid is transformed into a circle as described in [Nowell]. By projecting the circle on the sphere, the spherical cap opening required by the stereographic projections is naturally found. Equation 3.5 shows how the transformation is done. Notice that the points over the axis do not change, points in the corners get normalized and all others are transformed accordingly, as shown in Figure 3.5.

$$\begin{aligned} x' &= x\sqrt{1 - \frac{1-y^2}{2}} \\ y' &= y\sqrt{1 - \frac{1-x^2}{2}} \end{aligned} \quad (3.5)$$

The following section explains how to project the transformed grid to the sphere. Figure 3.6 shows the results of mapping a regular-grid and log-grid on the sphere.

3.2.3 S-rep projection from the plane to the sphere

Once the “circular log grid” is created, the projection finds the corresponding positions on the sphere. Equation 3.6 shows how the projection is done where $X = L(S(x'))$ and $Y = L(S(y'))$.

$$\begin{aligned} xs &= 2X/(1 + X^2 + Y^2) \\ ys &= 2Y/(1 + X^2 + Y^2) \\ zs &= (-1 + X^2 + Y^2)/(1 + X^2 + Y^2) \end{aligned} \quad (3.6)$$

Figure 3.6 shows how the points from the regular grid and the log grid map on a sphere. The latter has better hub distribution on the sphere and produces a better s-rep of the cortex.

Once the hub positions are sampled on the sphere, a fitting procedure to the spherical data provided by *Freesurfer* is done.

3.2.4 Fitting the s-rep to *Freesurfer*’s data

At this point there are two spherical representations. The first one corresponds to a cortex; the second one corresponds to the s-rep’s SS.

To fit the s-rep to the spherical representation of the cortex, each hub position is used as input to search for a set of closest points on the spherical representation of the cortex.

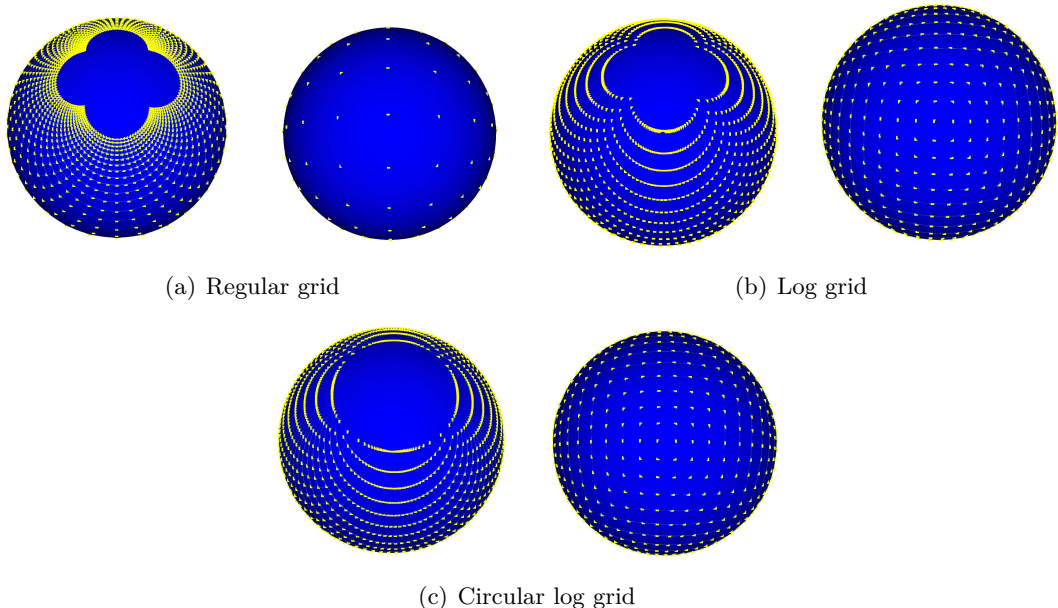


Figure 3.6: The north (left) and south (right) poles are sampled using a regular, a log grid and a circular log grid. The log grid sampling maps more points towards the south pole, and the circular grid produces the spherical cap opening in the representation.

The searching procedure uses as standard closest neighborhood search algorithm with kd-trees. The kd-tree quickly locates the closest points on the sphere from *Freesurfer*.

The folding procedure in the following section uses the points found and their relationship to the GM and WM surfaces in order to fold the s-rep into the cortex.

3.2.5 Folding the s-rep: from the sphere to the cortex

The s-rep is folded into the cortex using the points found on the sphere and the cortical widths given by *Freesurfer*.

The following penalties minimize an objective function for each hub:

1. The hub's distance to the GM and WM surfaces (half the cortical width).
 2. The top spoke's tip distance to the GM surface.
 3. The bottom spoke's tip distance to WM surface.
 4. The normal of the SS (see Equation 2.22) to the normal of the WM surface.
 5. The normal of the SS to the normal of the GM surface.

The procedure folds back the s-rep that was sampled on the spherical space to the original shape of the cortex. After the folding, the topology of the s-rep is preserved. In other words, each of the quads that build the skeletal structure are correctly oriented on the folded form of the cortex. Moreover, both top and bottom spokes point towards the GM and WM surfaces respectively. The width of the spokes is also determined.

The interpolation mechanisms described in Section 2.4 can be used to produce the WM and GM surfaces. Since the implied surfaces are not equivalent to the original ones, the following section evaluates their quality.

3.3 Evaluation of the implied GM and WM surfaces

To evaluate if the surfaces are close enough to the original ones, a tool known as *Meshvalmet* is used. The tool uses the Hausdorff distance to estimate the difference between discrete 3D surfaces. The approach is based on [Aspert *et al.* (2002)]. It calculates the mean distance error from each vertex of the reference surface to a target one, in this case, the interpolated surface against the original surface. The comparison is done separately on the GM and WM surfaces. The sampling step is set to 0.1 and an absolute distance measure is used. By lowering the sampling step and using the absolute distance, the accuracy of *Meshvalmet* is increased.

Analyzing the results of *Meshvalmet* yields a set of parameters to generate the best possible representation for all subjects. The parameters to set for the s-rep are size and sampling step on the sphere. The following section analyzes the size of the s-rep.

3.3.1 Best s-rep size

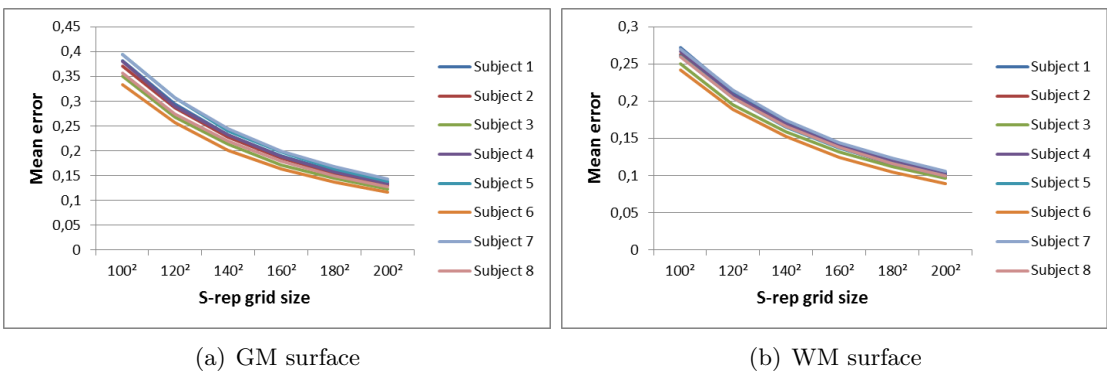


Figure 3.7: Mean error using different grid size of the s-rep.

The first parameter to set is the size of the s-rep. This is based on different criteria such as reducing the number of points in the original data. A typical cortical surface contains 130,000+ vertex. By using an s-rep of 160^2 atoms, the information is reduced by 40%, *i.e.* 76.800 tuples including the hub positions plus both spoke directions.

Figure 3.7 shows the mean error using s-reps of different sizes, tested on 8 different subjects. The following analysis uses a grid of 160^2 atoms for all cases.

3.3.2 Best s-rep sampling

The second parameter to set is the initial value for the log scale sampling on the grid. This parameter controls how the hubs will distribute on the sphere. A value close to 0 will map a larger number of points towards the south pole. Figure 3.8 shows the average area of the quads that compose the skeletal locus of the s-rep and their SD (standard deviation). Notice that for values greater than 0.04, the SD increases rapidly. Figure 3.9 shows the mean error of the interpolated surfaces for different *Min* values. According to the analysis, values between 0.01 and 0.4 seem reasonable as the minimum error overall cases for the surfaces is found inside this range. The *Min* value is set to 0.02 in order to increase the regularity of the quads and lower the mean error of the surface. This value produces the best results over all subjects used in the analysis.

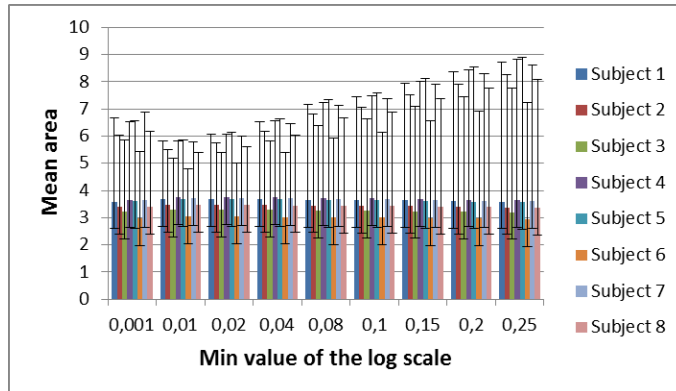


Figure 3.8: Average quad area of the s-rep with standard deviation for different *MIN* values of the log scale.

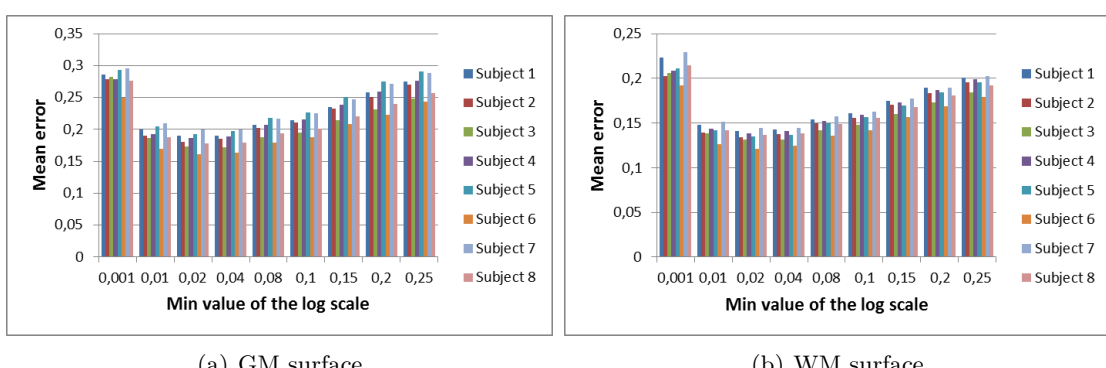


Figure 3.9: Mean error of the GM and WM surfaces for different *MIN* values of the log scale.

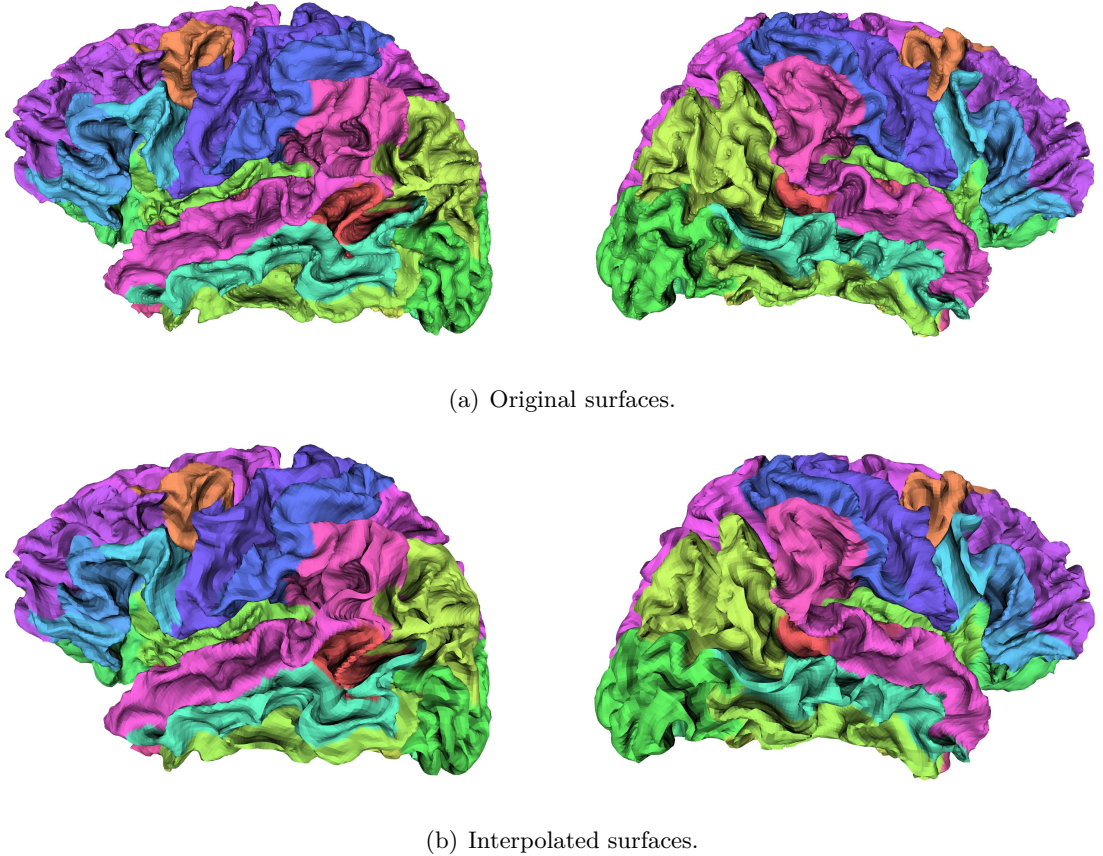


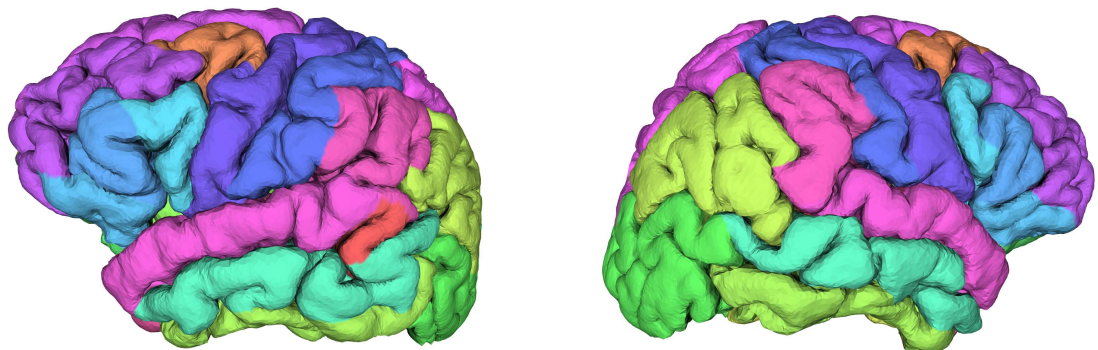
Figure 3.10: Comparison of the original and interpolated WM surfaces for the left and right hemispheres. The s-rep has 160^2 atoms. The interpolated surfaces seem to have wrinkles at some places but according to the error measurement, they are close to the original ones. Moreover, modeling the cortex via s-reps offers new capabilities such as the local coordinate system inside the structure. This new set of capabilities are not available in the regular representation.

Figure 3.11 shows the interpolated cortex for both hemispheres. The coloring on the surfaces are set according to the cortical parcellation of the neuroanatomical structures at each location in the cortex.

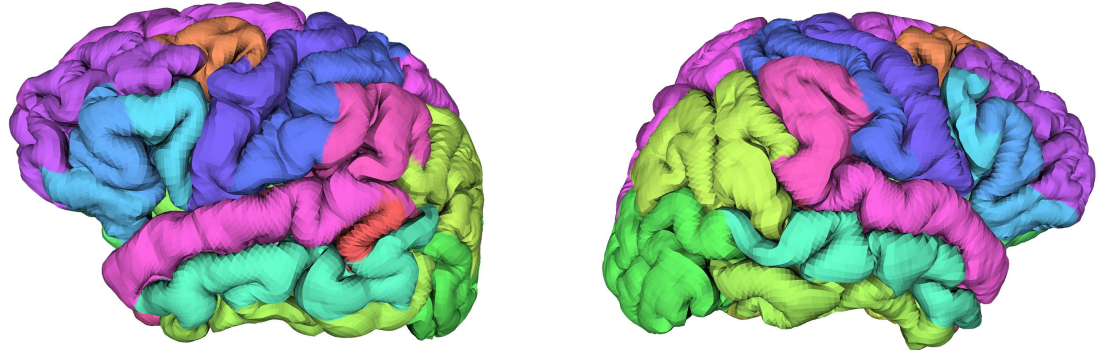
In the following section, the s-rep of the cortex is used to evaluate the changes of cortical width using synthesized data from a base model.

3.4 Shape statistics of the cortex using CPNS

S-reps live in abstract manifolds that are curved, composed by a Cartesian product of a Euclidean space and a collection of spherical spaces. Using s-reps to compute shape statistics should yield better shape descriptors as volumetric information is included into the analysis. Previous studies on s-reps of hippocampi have shown CPNS to yield lower-dimensional shape space with an efficient collection of modes of variation better than PCA-based statistical analysis of other skeletal or non skeletal models [Pizer *et al.* (2012)], [Schulz *et al.* (2012)]. The analysis on the cortex is challenging since its dimension is very high and shape variations could go undetected by the approach.



(a) Original surfaces.



(b) Interpolated surfaces.

Figure 3.11: Comparison of the original and interpolated GM surfaces for the left and right hemispheres. The s-rep has 160^2 atoms. The interpolated surfaces seem to have wrinkles at some places but according to the error measurement, they are close to the original ones. Moreover, modeling the cortex via s-reps offers new capabilities such as the local coordinate system inside the structure. This new set of capabilities are not available in the regular representation.

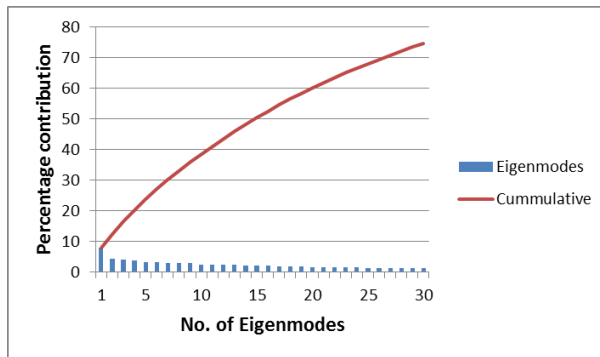


Figure 3.12: Mean modes of variation for the cortical representation.

The objective of using CPNS on the cortex is to detect cortical thickness variations. In order to do this a test case is made using a base s-rep and 60 models derived from the same one. The cortical thickness is reduced in specific regions of the cortex. The datasets are created by adding some Gaussian noise to the position of the model, and to every spoke direction and radii in the s-rep. Each sample is going to be further modified with a linear variation of the cortical thickness, specifically on the superior frontal and superior temporal regions of the cortex. Spoke lengths are reduced 30% of their original length. If CPNS produces modes of variation, then the first mode should be related to the cortical thickness reduction.

Figure 3.12 shows the plot of the eigenvalues describing the mean modes of variation computed with CPNS. The first mode is responsible for the largest variation found in the dataset and should correspond to thickness reduction in the specific areas.

Figure 3.13 shows the evolution of the model by manipulating the first mode of variation. In the figure, the regions of the superior frontal and superior temporal of the cortex are thinner, and adjacent structures remain constant through the deformation. This can also be verified by checking the average thickness as shown in figure 3.14. As expected the first mode corresponds to the cortical thickness variation.

3.5 Conclusion

One of the major contributions of this work is to represent the cortex as a folded slab using s-reps. S-reps are able to model continuum space. This characteristic can be used for the following purposes: to include information in the cortex at different scale levels; provide new ways to analyze cortical columns, the building blocks of the cortical tissue; analyze cortical lesions in a different space.

These new advantages will use the local coordinate system $[u, v, \tau]$ provided by s-reps.

A second contribution is to provide a compact representation of the cortex using CPNS. This statistical description models cortical thickness variations with a mean shape, some eigenmodes and a few coefficients. Previous work with CPNS was done to study shape variations on the hippocampus using a grid size of 8×3 atoms to represent the population of objects. In this case, the s-rep size is 160×160 atoms; nevertheless, CPNS was able to capture the localized thickness variation produced in the superior-frontal and superior-temporal regions of the cortex. This suggests that the approach could produce statistics for longitudinal clinical cases that are characterized by cortical thickness variations. Cortical thinning is a natural process of aging [Kaplan *et al.* (2009)]. Other clinical cases such as psychosis, schizophrenia, hyperactivity disorder in children and autism also present

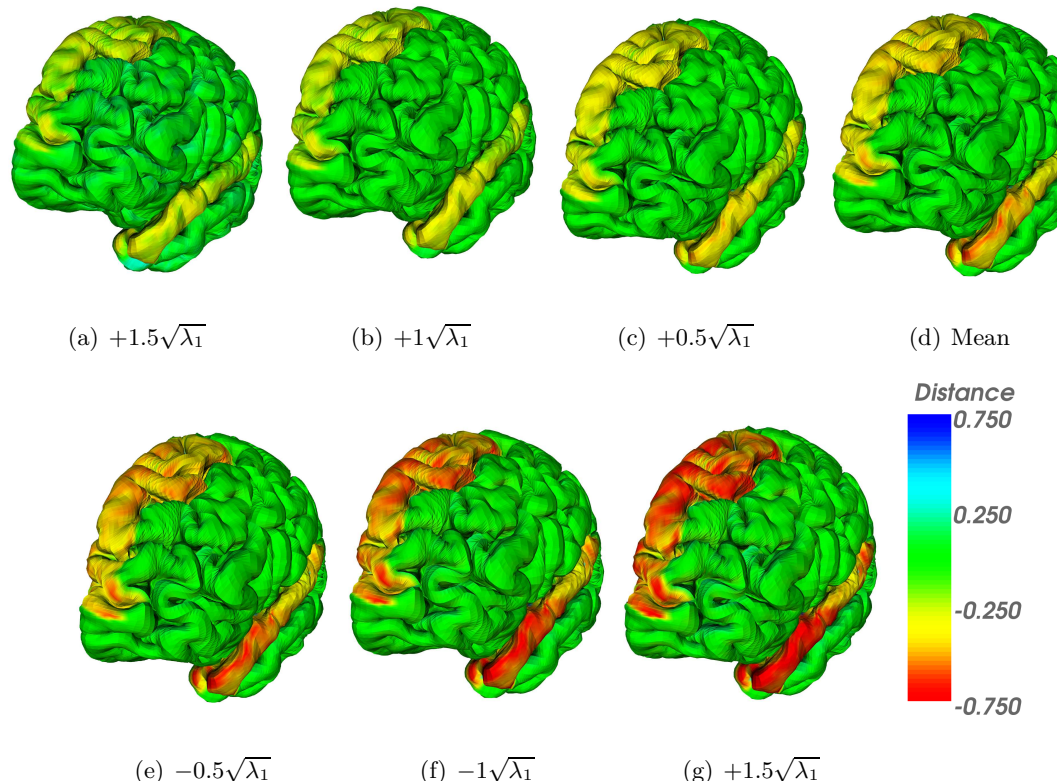


Figure 3.13: Deforming the s-rep model using the first mode of variation and comparing it against the base s-rep.

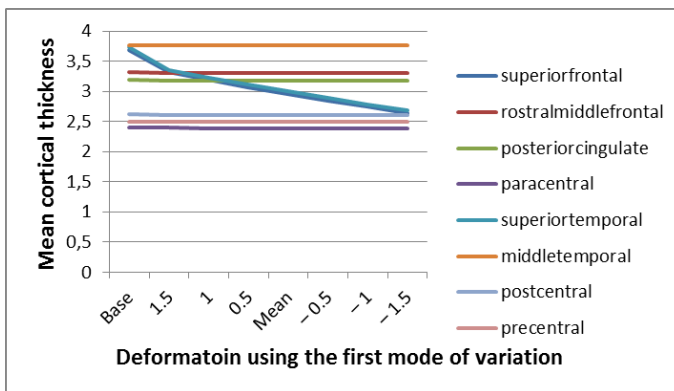


Figure 3.14: Average thickness for some cortical regions in the cortex. The two regions changing through the deformation are the superiorfrontal and superiortemporal.

abnormal cortical thickness variations.

A third contribution is to model the cortex of different patients using the same underlying skeletal structure. A test case was done to compute a mean shape of the cortex for the 8 patients used in this study. Figure 3.15 shows the mean surface for the 8 datasets computed with *Freesurfer* and CPNS.

Unfortunately in this case, CPNS was not able to detect principal modes of variation. This could be for two reasons. The main one is related to the number of datasets used in the study. The dimension of the s-rep is too high compared to the sample size. The second reason could be related to the alignment of each of the cortical regions. To produce accurate shape statistics, the objects must be aligned correctly.

It has been proven that s-reps are suitable entities to model the complex shape of the cortex and provide new ways of cortex analysis.

Future work considers the following possibilities: the first opportunity is related to shape analysis of the cortex in multiple subjects scenarios. The objective is to produce a usable set of coefficients and eigenmodes that models a population of cortices. A second opportunity is related to cortex analysis on longitudinal scenarios. For this purpose three or more acquisitions of a patient at different time points could be used to study the process of aging.

The work presented here showed that CPNS can detect cortical thinning on a set of cortices; a third line of work seeks to describe the folding procedure of the cerebral cortex using shape descriptors.

The following chapter explains a texture synthesis technique to create volumetric representations using 2D image samples. The volumes can be used on s-rep models to create solid objects.

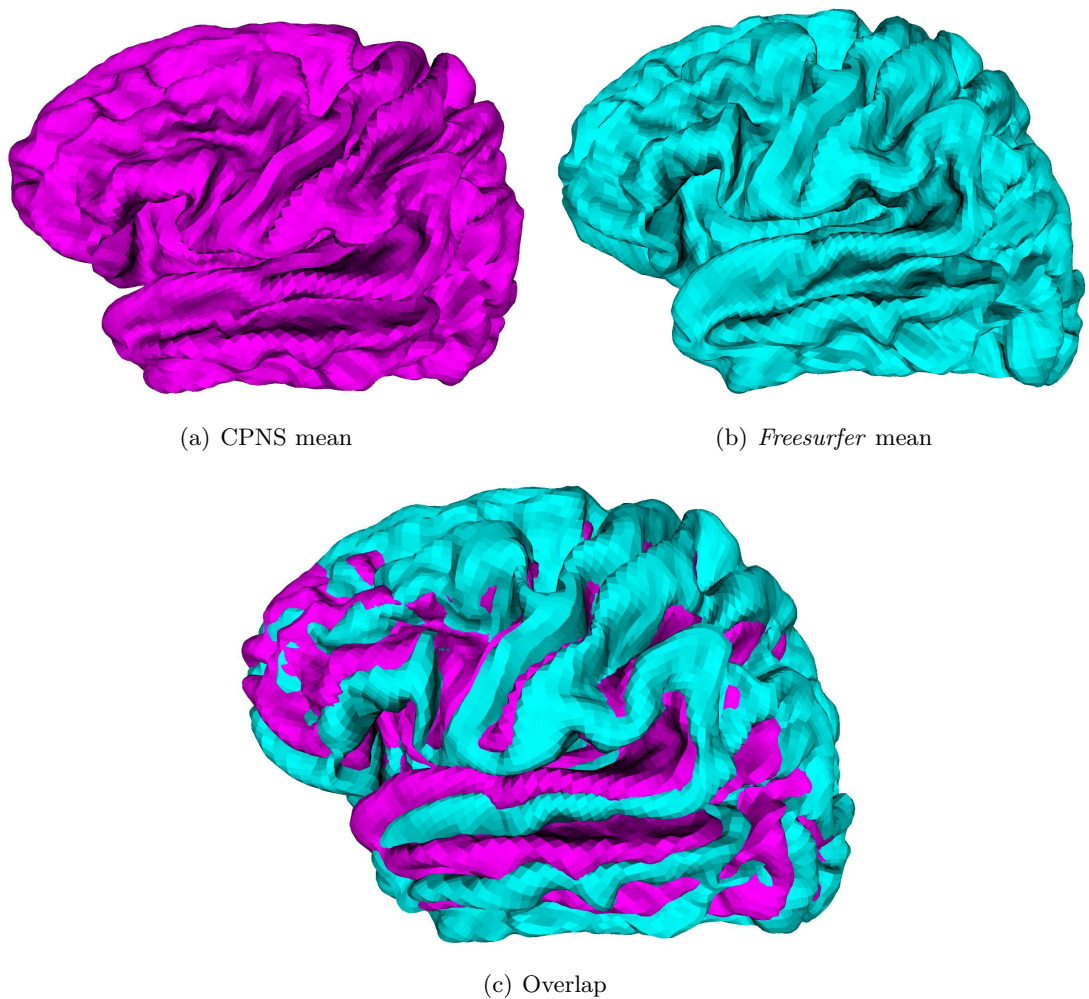


Figure 3.15: Mean shape computed from the 8 datasets.

4

Texture synthesis for 3D object representation

4.1 Introduction

A texture synthesis approach will be used to enhance the properties of objects. The objective in this dissertation is to produce solid blocs of physical parameters. These solids will be used with s-reps to produce simulated images. To understand this approach, it is necessary to understand the properties of texture.

Objects in the real world have a large number of visual properties. Among those properties are luminance, color, relative motion, stereo disparity and surface characteristics including reflectance and roughness. When all of them are combined, the result is a textured image.

Human perception has the capability to separate textured regions. This phenomenon is known as texture segregation; it allows us to distinguish a wide variety of objects and materials with little effort.

Figure 4.1 shows an image composed by three types of letters Xs , Ts and Ls . We are able to easily detect the left region (Xs) but some effort is required to differentiate the right region (Ts) from the background (Ls). Even though there are no clear edges in the image, our visual system is capable of detecting all of the regions.

This type of observation led to the *Julesz conjecture*, a hypothesis as to whether human texture perception was sensitive only to differences in the first and second order statistics. It was later concluded by Julesz himself that images with identical third order statistics could also be easily discriminated by our visual system [Julész *et al.* (1978)].

The counterexamples gave the idea that it was possible to model texture with low-order statistics and led to feature-based theoretical approaches.

Definition 6. *Textons are fundamental micro-structures in generic natural images and the basic elements in early (pre-attentive) visual perception.*

Texture analysis by its features or textons enabled the reduction of redundant information and produced compact representations of texture easier to manipulate. This characterization found application in a wide variety of fields that include image segmentation and object recognition [Leung and Malik (2001)], and image/video editing, merging, and completion [Wexler *et al.* (2004)]. It provided cues to understand the function of neurons in biologic vision systems which led to advances in neurophysiological texture perception [Olshausen and Field (1997)], [Landy and Graham (2004)].

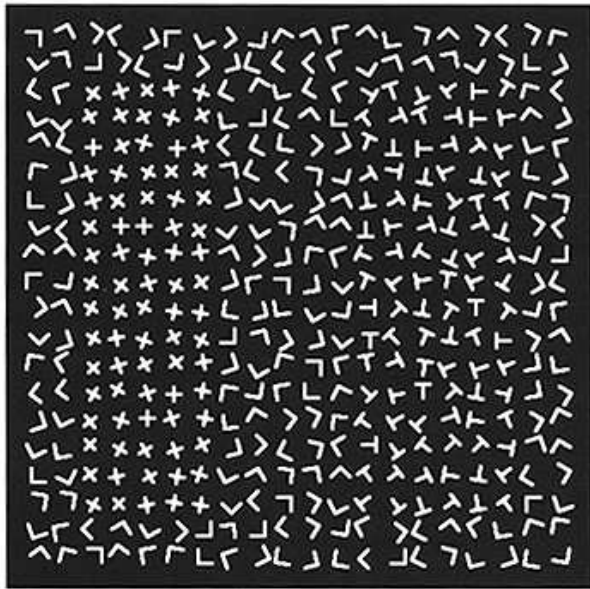


Figure 4.1: Image taken from [Bergen and Landy (1991)]. The image has three regions that can be distinguished: One composed by X s a second one with T s and the background with L s.

In computer graphics, applying textures to geometric models is key to enhance 3D object representation. As texturing and rendering methods improve, 3D virtual objects become more realistic and appealing to our visual system.

The first step to apply texture in a 3D object is to acquire samples large enough to cover their whole surface. To do this, we need methods capable of synthesizing texture.

Textures can be categorized in a structural vs. stochastic tradeoff. Natural textures are found somewhere in between containing stochastic and regular aspects. Structural textures have regular patterns such as a tiled floor. Stochastic textures don't have a specific structure or organization; they look like colored dots randomly distributed in the image. In general, there are two approaches to synthesize texture. Procedural and exemplar-based.

Procedural approaches seek to model texture using noise functions. These methods exploit the stochastic features of textures and a wide variety of results can be achieved by "structuring" the noise.

On the other hand, exemplar-based approaches rely on the MRF (Markov Random Field) assumption, *i.e.*, texture locality and texture stationarity. Assume that we are able to analyze a textured image using small windows of fixed size. Texture locality means that new pixels could be predicted from the information on a single spatial window and texture stationarity means that texture spatial statistics are invariant in multiple windows. This line of thought has many desirable properties. It suggest that a small textured sample can be used to replicate the stochastic and structural features on larger images. The major drawback would be the time to synthesize a result.

The first challenge of MRF approaches is to keep the initial look of the exemplar. This can be done by replicating the texture features at random places in the new image while avoiding unnatural seams and repetitions. A second challenge is to synthesize texture on a surface using properties such as orientation or scale.

In this dissertation, a MRF approach for solid texture synthesis is used. Solid tex-

tures provide volumetric information and model internal properties. They can be used to perform scattering simulations, enhance volume rendering of an object or reveal internal features. In the same manner, the synthesis method uses 2D textured images and produces a solid with similar characteristics to the exemplar.

Solid textures will be used on organ models to generate solids representing the parameters for MRI image simulation. These parameters are obtained using relaxometry. A technique that measures specific physical and chemical properties of materials in MRI. Besides generating distributions of physical parameters, the synthesis method can be used to improve the visual properties of objects.

Exemplar textures are generated for some brain structures containing the corresponding physical parameters acquired in the relaxometry images. The textures have four channels: T_1 , T_2 , T_2^* and $M0$, *i.e.*, two relaxation constants, the local field inhomogeneity and proton density. The generated textures applied on the geometric models will be used to simulate an image of some brain structures, the simulation is explained in Chapter 5.

The following section reviews the most important authors for procedural and exemplar-based texture synthesis.

4.2 Texture synthesis methods and applications

4.2.1 Procedural texture synthesis

Procedural texture synthesis methods are useful to simulate elements from nature like clouds or water waves. They are memory-efficient and guarantee continuity and consistency of the texture. In theory, procedural approaches can generate any pattern but the calibration of the method can be a very difficult task. The procedure is not intuitive since the user must elaborate an analytic description of the texture.

Solid textures can be synthesized by procedural methods [Perlin (1985)] and [Peachey (1985)]. In fact, the functions return a color value at any given point in 3-space.

Different texture patterns have been studied. [Witkin and Kass (1991)] used a reaction-diffusion equation to generate stripe patterns. [Walter *et al.* (2001)] used a biological model to reproduce the texture of animal skin.

A recent approach by [Lagae *et al.* (2009)] is able to generate several natural textures like marble, wood and different animal skin patterns. It provides a user-friendly interface to set up the required parameters to control how the texture is generated. Controlling the noise patterns allows texture generation according to surface orientation; in other words, a fiber-like texture can be oriented on the object's surface and no object-coordinates are needed.

The advantages of procedural texture synthesis are that it does not require much memory to synthesize the texture; that the resolution is not fixed and detail can be added depending on the scale; that it can cover large areas without seams or texture repetitions; and that it can be parameterized to generate a transition to a different texture during the procedure.

4.2.2 Exemplar based texture synthesis

In this dissertation, an exemplar-based method is used to generate solid textures. The reasons are that procedural textures are difficult to build and it is hard to control how the patterns are generated. Exemplar-based approaches provide more flexibility to be used with different textures in the stochastic - structured range.

For the rest of the chapter the following definition of texture synthesis is used:

Definition 7. *Texture synthesis is the process of generating a larger textured image from a small exemplar.*

Exemplar-based synthesis usually has two stages: a search in the texture sample space and a merge phase to produce the synthesized output. Most of the methods have also been extended to synthesize solids.

Pixel-based synthesis

The texture synthesis approach proposed by [Efros and Leung (1999)], starts with a seed pixel and grows outwards. It performs a closest neighborhood search in the sample image and then it grows by adding new pixels accordingly. To achieve good results with textures such as a brick wall, it is necessary to employ large neighborhoods in order to capture the structure of the texture. Moreover, the search step does not enforce using all of the texture information in the image and causes repetition of the same neighborhoods very often.

[Wei and Levoy (2000)] proposed some improvements that modified the search step using a fixed size neighborhood and a random initialization of the output texture. The fixed neighborhood allowed data structures such as kd-trees to accelerate the search phase and allowed the random initialization enforced in the synthesis to use more information from the exemplar. Unfortunately, the method is highly dependent on the initialization stage and in some cases is not able to include all the information from the exemplar.

[Ashikhmin (2001)] proposed a speedup based on coherence. The idea is to keep the positions on the exemplar of the synthesized pixels. It is unlikely that pixel chosen during the synthesis will change to a different one. Therefore, keeping the index position reduces the overall search time to produce an output. [Tong *et al.* (2002)] further improved coherence by keeping k candidate pixels. The k -coherence approach produces the best results among the pixel based methods.

Patch-based synthesis

Patch-based synthesis is similar to pixel-based approaches. The difference is that instead of writing a single pixel, a whole patch is written to the result. Some techniques conceived to produce a good result when merging patches are the following: overwrite the overlapping patch [Praun *et al.* (2000)]; blend the overlapping regions [Liang *et al.* (2001)]; find an optimal cut to seam the patches [Kwatra *et al.* (2003)]; and warp the patches to ensure continuity [Wu and Yu (2004)].

There are some known issues about these techniques. Blending the patches might cause blurring , and when the smooth transition between regions is not found, the output textures contain visible seams.

In general, pixel- and patch-based approaches are prone to accumulate small errors over the synthesis procedure and lead to inconsistencies in the synthesized texture.

Optimization-based synthesis

Texture synthesis by optimization was proposed by [Kwatra *et al.* (2005)]. The approach uses the best of both techniques previously discussed. It calculates the output value one pixel at time, but it uses the information from all of the patches that contribute to a single pixel. The value is determined by optimizing a quadratic energy function, leading to better output quality.

The global optimization framework is designed from an MRF assumption. If locality and stationarity are satisfied, a global measure of energy can be designed by comparing the neighborhoods of the input and output textures. The energy is defined as the distance to the closest neighborhood in the exemplar. The sum over all neighborhoods defines the total energy of the output texture, and the solution of the synthesis procedure is found when the energy is minimized.

Texture synthesis by optimization is very flexible. It has the advantage of creating models using one or multiple samples in order to constrain the view perpendicular to each axis direction. It can use multi-channel textures like RGB and distance maps [Lefebvre and Hoppe (2006)]. [Kopf *et al.* (2007)] improved the optimization procedure by adding histogram matching and enforcing the exemplar statistics on the volume. [Chen and Wang (2010)] uses index and position histograms to enforce the synthesis procedure to use all neighborhoods from the exemplar.

4.2.3 Enhancing medical applications using textures

Texturing anatomical structures of the body has been used to understand complex medical images and distinguish organ details such as orientation, scale and materials [Netter (2010)].

This type of illustration is used to facilitate the communication process among doctors, students and patients. Medical students use these illustrations to facilitate the learning and training process. Doctors and surgeons use them to explain a certain treatment to a patient. However, it is desirable to have this information using patient-specific data since the shape of an organ may vary depending on the phenotype or pathology from one patient to another. Moreover, patient-specific illustrations can be used to guide subsequent treatment and planning to an optimal direction; notably dose radiation for cancer treatment needs high quality patient-specific models.

[Merck (2009)] proposed MGR (model guided rendering). It seeks to enhance patient-specific anatomical models using textures and provides the mechanism to improve radiotherapy planning. [Kabul *et al.* (2011)] improved the mechanisms to apply texture to organ models by controlling the synthesis procedure using vector fields and texture metamorphosis. Texture metamorphosis refers to the process of smoothly interpolating between two textures.

MGR uses the coordinate system provided by m-reps (see Section 2.3.2) and applies solid textures to the models according to their geometric properties. The following section explains the technique to synthesize solid textures.

4.3 Solid texture synthesis

The interior of organs must be textured to make them appear as if they were the physical parameters required for MRI simulation. The solid texture synthesis method derives from [Kopf *et al.* (2007)]. Similarly, the method uses exemplars and by means of an energy optimization process, the 3D texture looks like the 2D image in every slice. This implementation has been reviewed in [Prieto *et al.* (2012)e], [Prieto *et al.* (2012)c], [Prieto *et al.* (2011)]. The reference image can be textured elements from different sources such as:

1. Artificial images artistically created for computer graphic design or medical atlases.
2. Real images from digital microscopy of biomedical histological slices.

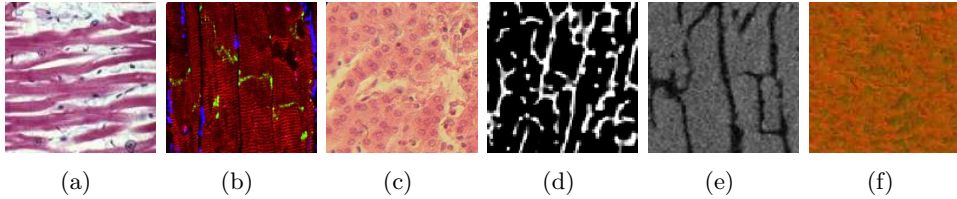


Figure 4.2: 128^2 textured samples available to create volumetric data: histology images of (a) striated cardiac muscle, (b) myocytes, (c) hepatocytes; (d - e) a slice from a SR μ CT and μ MR image of a trabecular bone sample; (f) physical parameters image of the hippocampus (T_1 -red, T_2 -green, T_2^* -blue, M_0 -alpha). All channels rescaled between [0-255] for illustration purposes).

3. 2D reference textures provided by slices extracted from a μ MR and SR μ CT.
4. Textured images of physical parameters required to perform MRI simulation (the image is rescaled for visualization purposes).

Figure 4.2 shows some examples of texture.

Section 4.4 presents the generated solids with the exemplar images shown in Figure 4.2.

Modeling different types of organs and tissues at the cellular level represents an interest for histology, *i.e.*, the study of tissues. Histology plays an important role in the comprehension of morphological relationships between the organs and tissues. It considers the structural organization or precise hierarchy of the organs with the smallest details. When a geometric model is enhanced with these type of textures, it will acquire structural information at different scales.

The approach is based on the optimization framework proposed by [Kwatra *et al.* (2005)] defined by the following equation:

$$E(o, \{e\}) = \sum_t \sum_{i \in \{x,y,z\}} \sum_{u \in N_i(t)} w_{t,i} (o_{t,i,u} - e_{t,i,u})^2 \quad (4.1)$$

$$w_{t,i} = ||o_{t,i} - e_{t,i}||^{-1.2} \quad (4.2)$$

Equation 4.1 calculates the distance between the x , y and z neighborhoods of a texel t in the object o to the collection of 2D neighborhoods of the exemplar texture e . Equation 4.2 shows how to calculate the weight given to each neighborhood. The coefficient -1.2 is used to perform a robust optimization [Kwatra *et al.* (2005)]. When this function is minimized using IRLS (iterative re-weighted least squares), the result is an increase of similarity between the sample and the synthetic object.

The procedure begins at a coarse resolution assigning random values from the sample to the synthetic object. It alternates between a search phase, where the closest neighborhoods are found, and an optimization phase, where the weighted average of every texel is calculated. When the optimization converges, it changes to a finer resolution level using linear interpolation.

The following section gives details about the implementation. Section 4.4 shows the volumes and Section 4.5 evaluates the quality of the synthesized texture.

The accuracy of the synthetic images is assessed and discussed by comparing statistical and morphological parameters computed from the virtual and the real images.

4.3.1 Search phase

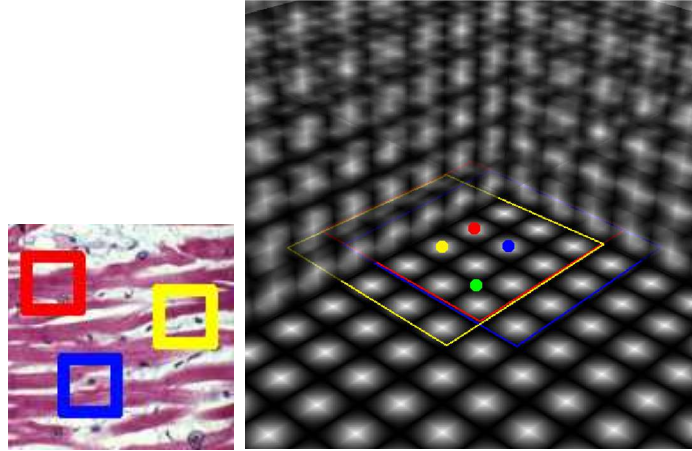


Figure 4.3: 9×9 red, blue and yellow neighborhoods for a slice in the volume, the center is represented by the colored dot. The green voxel is affected by multiple neighborhoods.

The sample image is divided into 9×9 neighborhoods that overlap each other. These neighborhoods are vectorized, *i.e.*, every texel from the neighborhood is stacked into a single vector. For RGB texels we have $9 \times 9 \times 3 = 243$ values in a single vector.

Once the vectors from the sample are constructed, PCA (see Appendix A) reduces the dimensionality of each vector passing from 243 to 18 values approximately. Reducing the vectors is a very convenient step, there are less values but we are still keeping 95% of the relevant information. The reduced vectors can be used to perform a standard closest neighborhood search in a high dimensional space. The ANN library¹ is used for this purpose.

During the search phase, a weight for each neighborhood is calculated. The energy function is written as shown in Equation 4.1. The weight of each neighborhood is calculated as shown in Equation 4.2. $N_i(t)$ represents the neighborhoods for each dimension x, y, z and u is the texel in the neighborhood of t . This means that a texel in the object is affected by multiple texels from different neighborhoods in the exemplar texture. The search is performed for every two texels $g_x = \{(i, 2 \times j, 2 \times k), \forall i, j, k\}$ (g_x is the voxel in a slice perpendicular to x). This is done similarly for y and z , as shown in Figure 4.3.

Once the search phase is done the optimization phase takes place and it consists in averaging all the values found for each texel of the volume.

4.3.2 Optimization phase

The optimization phase consists in averaging the values that affect one texel in the object. If the search phase is performed for every two texels as in 4.3.1, the average will be for at most 75 texels (25 for each dimension).

$$o_t = \frac{\sum_{i \in \{x, y, z\}} \sum_{u \in N_i(t)} w_{u,i,t} \times e_{u,i,t}}{\sum_{i \in \{x, y, z\}} \sum_{u \in N_i(t)} w_{u,i,t}} \quad (4.3)$$

Equation 4.3 shows the value of a texel in the object. When the texels present a high

¹ANN: A library for approximate nearest neighbor searching; <http://www.cs.umd.edu/~mount/ANN/>
Mount, D. M. and Arya, S. 2006

variability, the resulting object might be blurred. In order to avoid this issue, clustering is performed to only average those texels that correspond to the principal cluster.

After the optimization phase, histogram matching is done. This method preserves the global statistics of the exemplar in the synthetic object. As explained in the following section.

4.3.3 Histogram Matching

This method maintains the global statistics of the sample by using a histogram matching approach [Rolland *et al.* (2000)], [Heeger and Bergen (1995)]. To perform histogram matching, the *CDF* (cumulative distribution function) of the histograms is calculated for both the exemplar and the object. Two *LUTs* are constructed in order to perform faster calculations. The lookup table LUT_o maps the RGB values of the object to their corresponding value in the CDF_o . The lookup table LUT_e maps the CDF_e to the corresponding RGB values from the sample. The object is then modified by taking each of the texels t and using $LUT_o(t)$ to find the $CDF_o(t)$. Using $LUT_e(CDF_o(t))$ finds the corresponding RGB value from the sample. The value of the object is replaced by the corresponding value in the exemplar.

The following section shows some results produced by the implementation of the texture synthesis algorithm.

4.4 Types of solid textures

4.4.1 Isotropic texture from a 2D exemplar texture

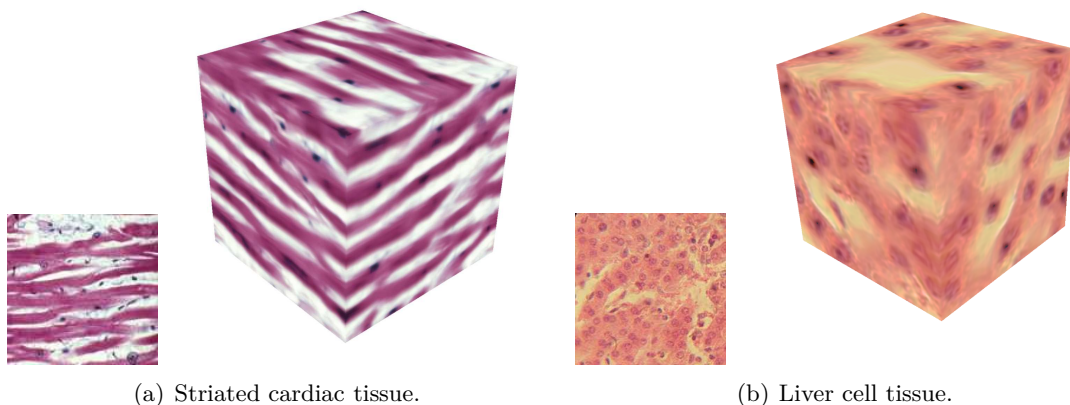


Figure 4.4: Results of isotropic synthesis. The striated cardiac muscle tissue (left) and liver cell tissue (right) were generated using a single reference texture for the axial, longitudinal and transversal planes.

Figure 4.4 shows some results when the same exemplar is used to constrain the axial, longitudinal and transversal planes. The method produces a volume of striated cardiac muscle tissue and the liver cell tissue from histology. Every longitudinal or transversal slice of the volume is similar to the reference texture without being, however, identical.

Figure 4.5 shows two synthesized volumes of physical parameters. The MRI values (see Chapter 5) for each component are between the following intervals: $T_1 = [1672 - 4111]$, $T_2 = [787 - 1793]$, $T_2^* = [54 - 2246]$ and $M0 = [20 - 595]$. All of them are rescaled to

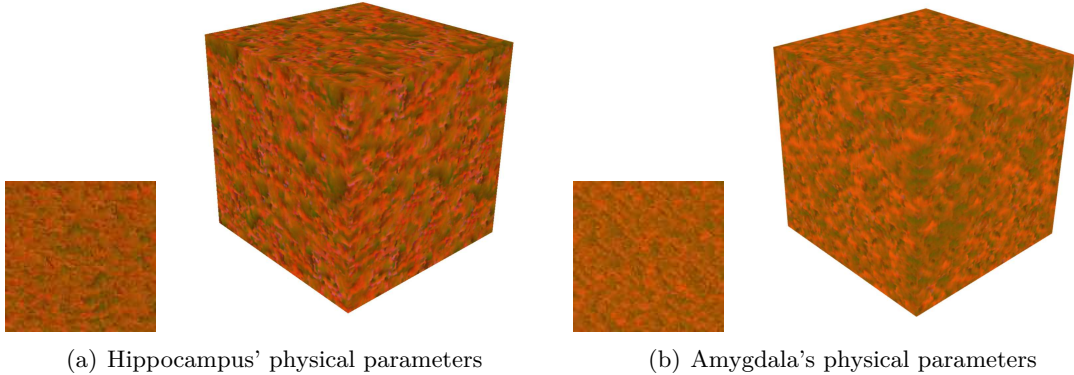


Figure 4.5: Results of isotropic texture synthesis using images of physical parameters of the hippocampus (left) and amygdala (right). The images have been rescaled to [0-255].

[0, 255] and are assigned red, green, blue and transparency respectively, this is done for visualization purposes.

The following sections shows the different type of textures that can be synthesized by the approach.

4.4.2 Anisotropic texture from many 2D exemplar textures

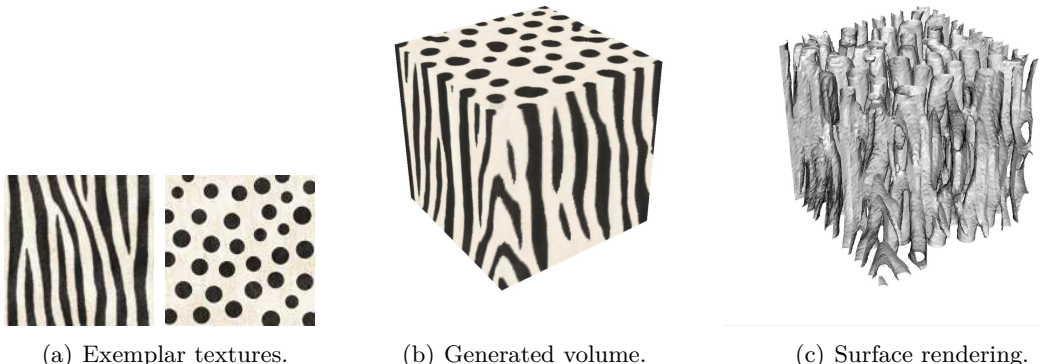


Figure 4.6: Results of anisotropic synthesis. The optimization was performed using the zebra texture to constraint the longitudinal and transversal planes. The dot texture was used in the axial plane.

Many anatomical structures and materials have different orientations and scales. These features can be illustrated by creating a texture that mimics these variations.

Figure 4.6 shows the result of selecting two different textures to constrain the optimization. Selecting the zebra texture and the dot pattern generated cylinder like structures. This is done by doing the search phase for the longitudinal and transversal planes in the zebra texture, while the axial plane does the search phase in the dot texture.

When rendering the surface of the object, we can see that the generated structure is very complex and consists of tubes that join and separate at arbitrary slices. This synthetic structure can be used to test Brownian simulation algorithms that reveal the environment's structures.

4.4.3 Anisotropic texture constrained by additional masks

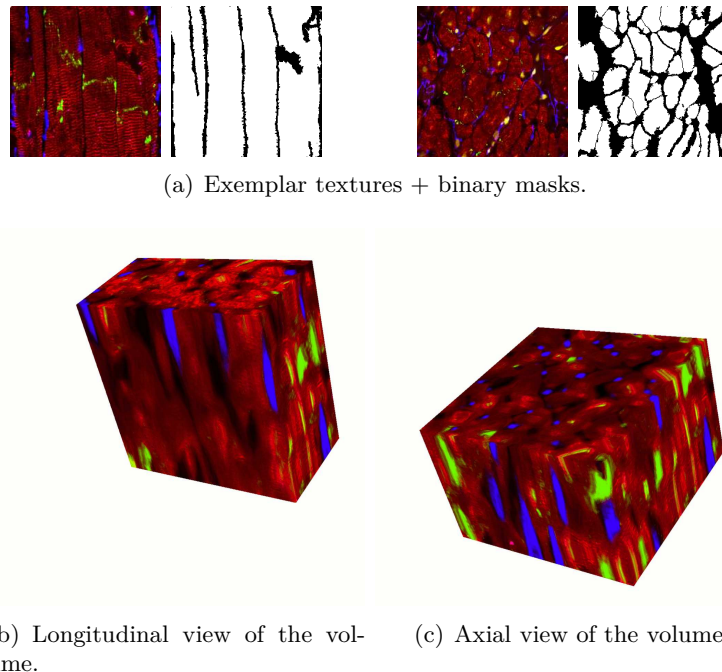


Figure 4.7: Results of anisotropic synthesis starting from two different textures and their additional binary masks.

It is possible to use a distance map as an extra channel, in addition to the RGB components. A binary image of the texture can be used to compute a distance map. This is useful when the texture has large unstructured areas [Lefebvre and Hoppe (2006)].

Figure 4.7 shows the synthesis results using different exemplar textures obtained from confocal images² and the corresponding binary masks. A signed Euclidean distance map is computed from the binary image and used as an extra channel in the synthesis procedure.

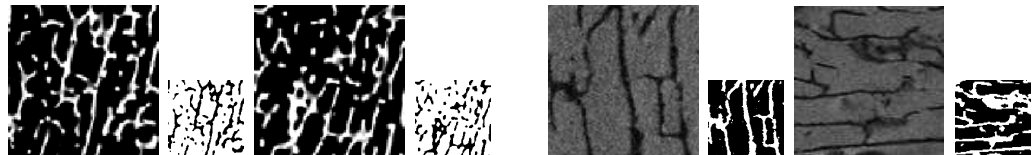
The 3D texture representing a myocyte cell tissue are quite representative of tissue viewed as complexes of cells (myocytes in red and fibroblasts in blue). The anisotropy of the cells is conspicuous and the contrast of staining is well preserved thanks to the use of the binary masks.

One main advantage of this method is to generate a 3D texture from 2D information. Up to now, it was impossible for the biologist or the physician to have a 3D representation of the cell tissue, since it is technically very difficult or even impossible to have an axial resolution as good as those in the slice. Thanks to this approach, the experts can get a virtual 3D representation of the tissues that are close to reality.

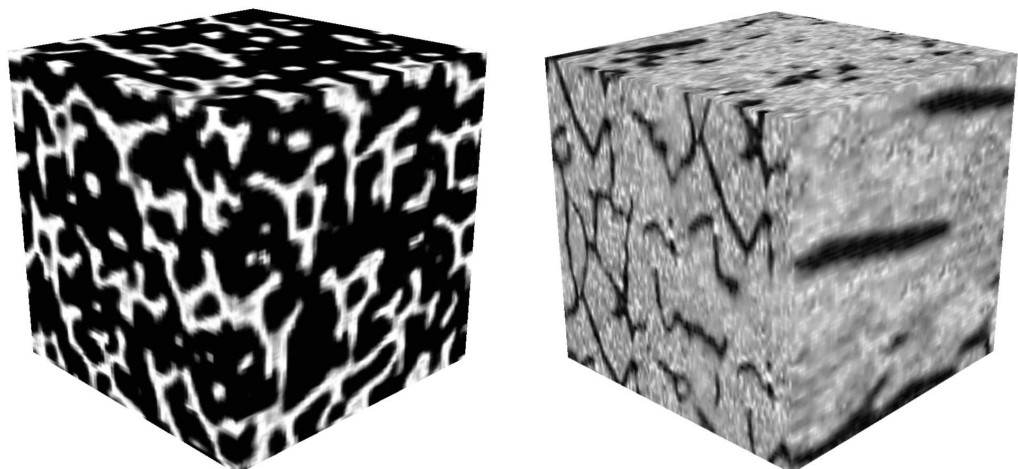
4.5 Evaluation of the synthesized textures

To assess the quality of the synthetic 3D texture, statistical and morphological criteria are used. As the ultimate goal is to produce a 3D texture as close as possible to the reference object, a comparison of statistical and morphological features between the reference and synthetic object is done.

²<http://www1.ic.ac.uk/medicine/people/p.camelliti/>

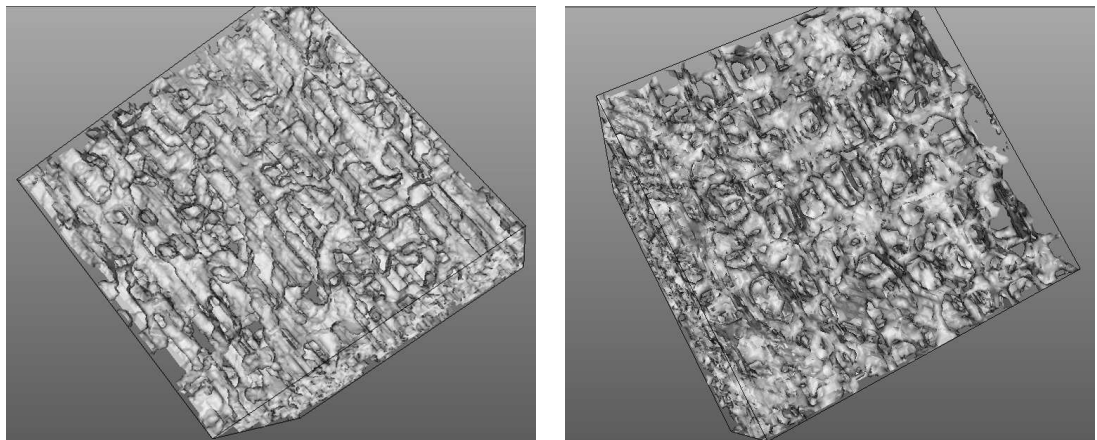


(a) 2D reference textures extracted from real images and binary masks.



(b) 3D virtual images.

Figure 4.8: Results of synthesis for $SR\mu CT$ (left) and μMRI (right) using multiple textures to constrain plans perpendicular to axis-directions and binary masks to enhance the untextured areas.



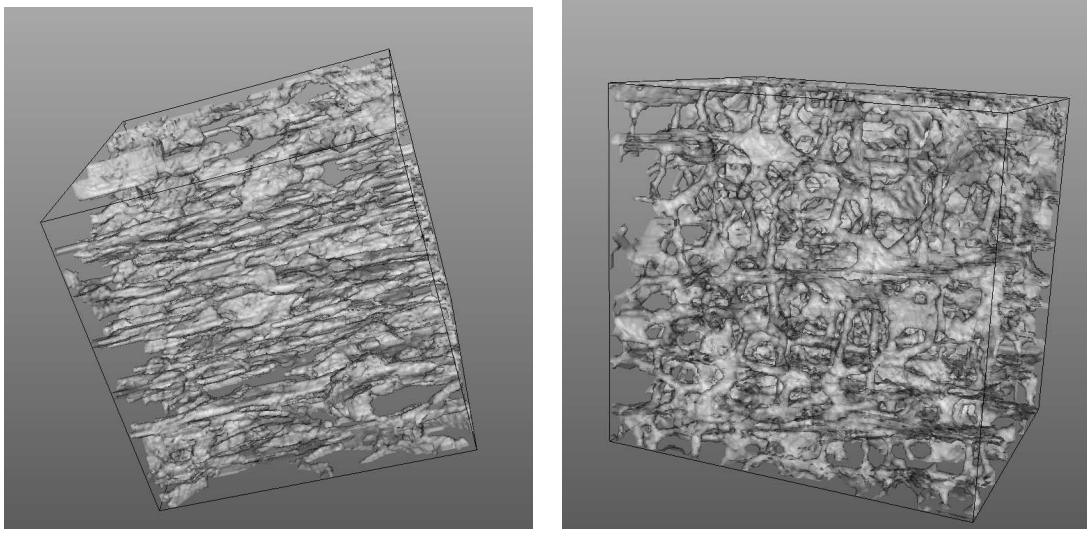
(a) Synthetic volume.

(b) Real volume.

Figure 4.9: Surface rendering of trabecular bone architecture obtained with the synthetic texture and the $SR\mu CT$ image.

4.5.1 Statistical assessment

Figure 4.11 shows the histograms from the muscle exemplar texture and the synthesized object shown in Figure 4.4. The total number of pixels in the texture are $128^2 = 16384$ and $128^3 = 2097152$ for the volume. When a randomly chosen slice is taken from the volume,



(a) Synthetic volume.

(b) Real volume.

Figure 4.10: Surface rendering of trabecular bone architecture obtained with: a) virtual μ MR image, b) real μ MR image.

		Mean	St. Dev	Min	Max	Mode
Red	e	189.6	34.7	45	255	148 (253)
	o	188.7	34.0	48	255	146 (33562)
Green	e	142.4	70.2	21	255	255 (189)
	o	141.4	69.3	21	253	253 (27571)
Blue	e	168.8	48.7	51	254	108 (207)
	o	168.0	48.1	51	252	102 (26765)

Table 4.1: Means and standard deviations for the RGB channels of the exemplar and the object

the global statistics are still preserved except from sampling errors. Table 4.1 contains the means and the standard deviations calculated from the histograms, the values from the object are similar to those of the exemplar with a variation lower than 1% for the means and lower than 2% for the standard deviations.

Figure 4.12 shows the histograms of the exemplar texture and the synthetic 3D μ MR image shown in Figure 4.8.

Thanks to the histogram matching, the grey levels distribution of the marrow and the bone are quite similar in the virtual image and the reference image. The statistics displayed near each histogram (mean, standard deviation, mode) are also very close.

The histograms of the exemplars and solids for the physical parameters are created using 256 bins. Figure 4.13 shows the histograms for the exemplars and synthesized volumes of physical parameters of the hippocampus. Global statistics are similar to the exemplar and shows the flexibility of the method to work with images having multiple components.

4.5.2 Morphological assessment

We propose to quantitatively assess the accuracy of the morphological structure given by the synthetic 3D texture. The method, software and original data sets used in this

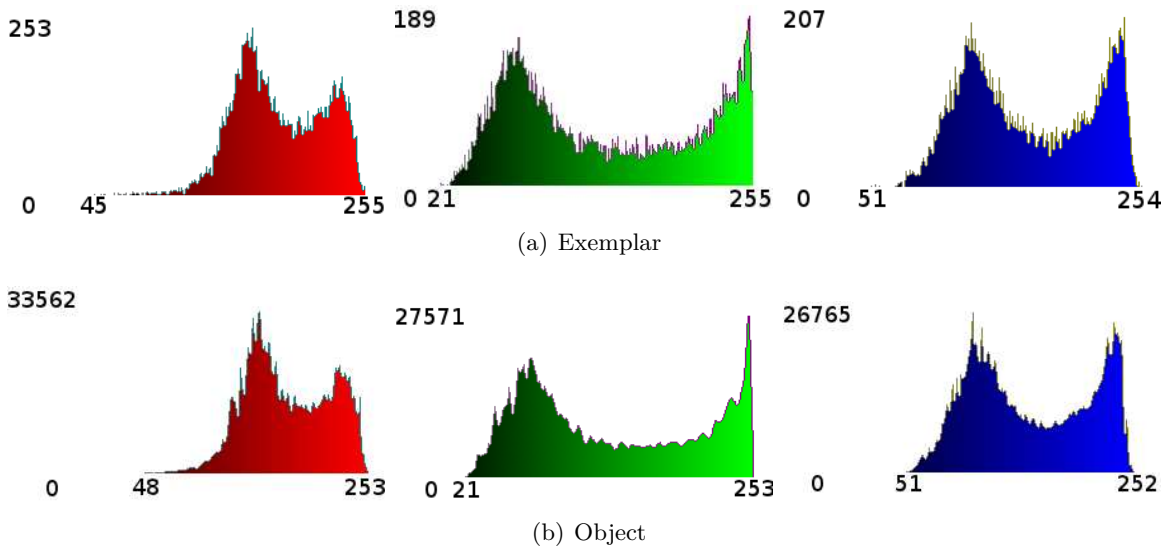


Figure 4.11: RGB histograms of the exemplar and the object for the striated cardiac muscle shown in figure 4.4.

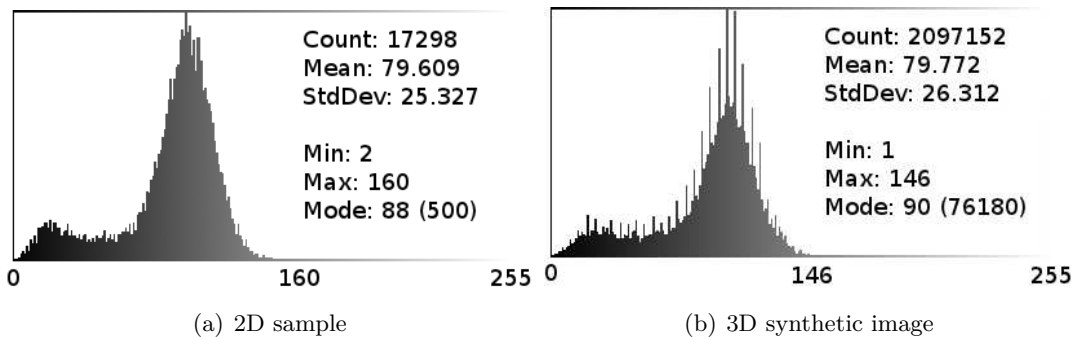


Figure 4.12: Comparison of the histograms obtained from the reference 2D and the 3D synthetic μ MR image.

section were created by [Revol-Muller *et al.* (2002)]. For this study, 3D textured images provided by Synchrotron Radiation Computed Micro-Tomography (SR μ CT) were used. These images were acquired some years ago on beam-line ID19 at the European Synchrotron Radiation Facility (ESRF) in Grenoble for the needs of a study focused on osteoporosis. Osteoporosis is a bone fragility disease leading to spontaneous bone fractures and characterized by a bone mass reduction and a bone structure deterioration. 3D Synchrotron Radiation Computed Micro-Tomography (SR μ CT) provided 3D high resolution images with an isotropic voxel of $10\text{ }\mu\text{m}$ width and a volume size of $330 \times 330 \times 330$ pixels can be used to assess trabecular bone architecture [Revol-Muller *et al.* (2002)]. We have at our disposal a set of twelve 3D SR μ CT images obtained from twelve calcaneus bone samples excavated from deceased human. For the test of my method, we worked on decimated SR μ CT images with a resolution of $80\mu\text{m}$ and a size of $83 \times 83 \times 83$ voxels. At this resolution, the signal to noise ratio is still high enough to extract trabecular bone from the background by simple automated thresholding. This binarizing step is needed for the computation of the bone parameters.

We computed morphologic and topological architecture parameters similar to those used in histomorphometry but computed on three-dimensional images from the set of

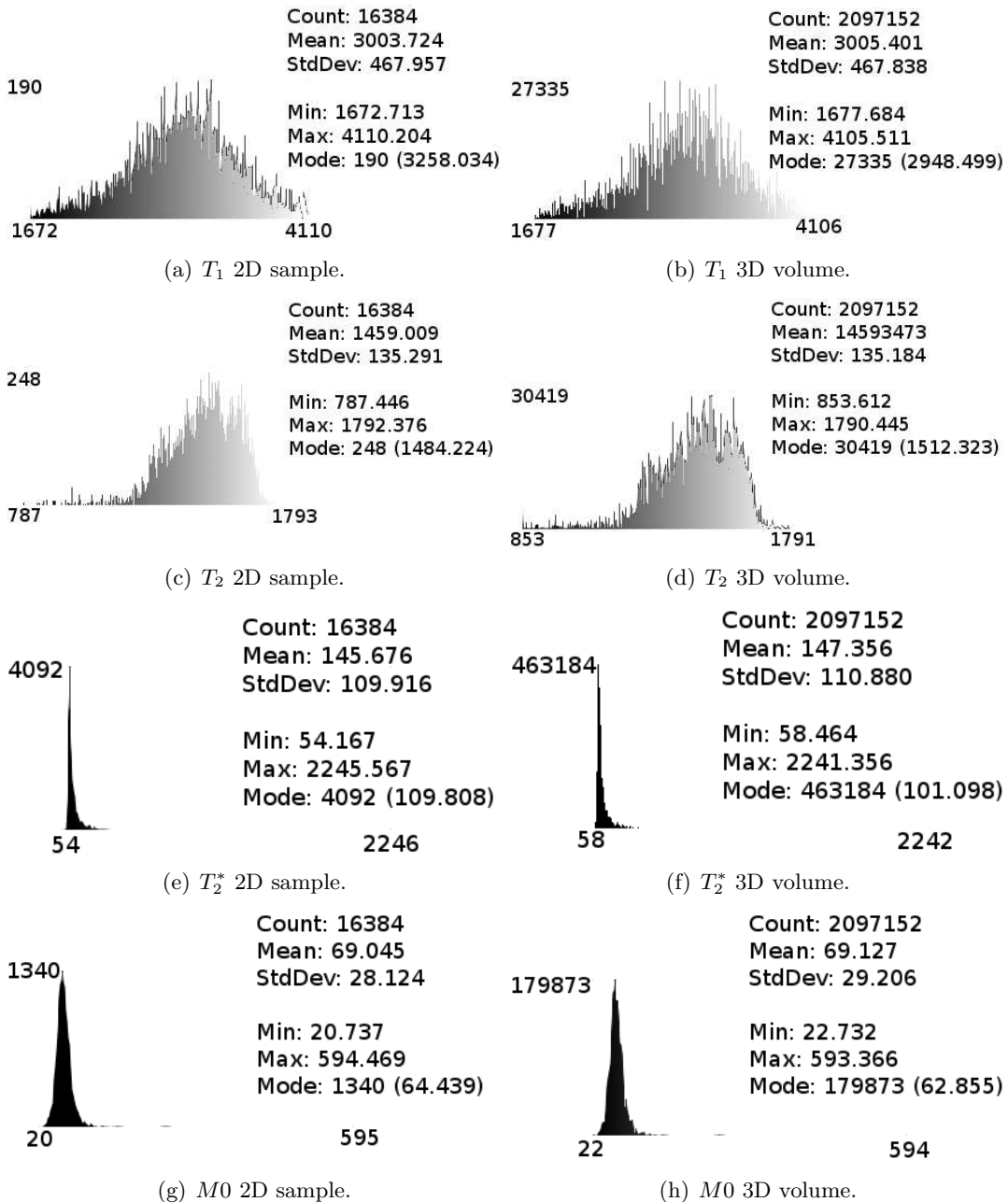


Figure 4.13: Comparison of the histograms obtained from the 2D exemplar (left) and the 3D volume (right) of physical parameters for the hippocampus shown in Figure 4.5.

the twelve volumes. A 3D MIL (Mean Intercept Length) method based on a three-dimensional version of the directed secant algorithm was chosen to produce many parameters related to the trabecular bone morphology [Hipp and Simmons (1997)] and the Euler number was computed to estimate the bone topology. We considered the seven following parameters: Partial Bone Volume (BV/TV), Bone Surface to Bone Volume ratio (BS/BV), Trabecular Thickness (Tb. Th), Trabecular Number (Tb. N), Trabecular Separation (Tb. Sp) and Mean Intercept Length (MIL1). The connectivity was estimated by the Euler number (Euler/mm³) implemented following the method described in [Odgaard and Gundersen (1993)] and normalized by the total volume. The higher the

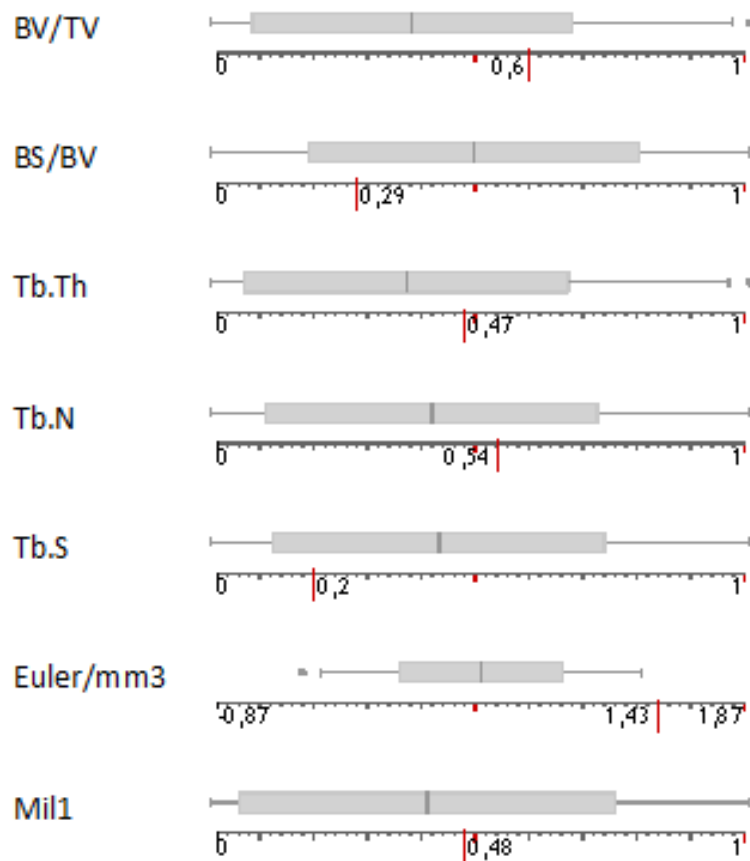


Figure 4.14: Box plots for morphologic and topological architecture of bone samples in SR μ CT images. The synthetic texture is displayed on the scale line under each box plot by a long red line.

Euler number's value, the less connected the bone structure is.

3D SR μ CT-like texture ($128 \times 128 \times 128$ voxels) was generated from two random reference slices (83×83 pixels) taken from one of the twelve SR μ CT volumes. We binarized the texture in order to extract the virtual bone architecture by the same automated thresholding that was used for the set of SR μ CT volumes. We assess the accuracy of the virtual bone structure by comparing the bone parameters computed from the set of SR μ CT images with those computed from the synthetic 3D volume.

Figure 4.14 displays the box plots associated to each bone parameter obtained from the set of SR μ CT images. As our aim is not focused on the analysis or the interpretation of these parameters but only on the comparison of them, we normalized each parameter by the range between their maximum and minimum values. The score of the synthetic texture is displayed on the scale line under each box plot by a long red line. All the morphological parameters of the virtual bone spread in a range lower than +/- one standard deviation from the mean value obtained from the SR μ CT. For the topology parameter (Euler/mm³), the score is higher than the maximum value obtained with the SR μ CT set. It means that the synthetic bone structure has a lower connectivity than the reference set and could represent a high degree of osteoporosis.

Figure 4.9 shows a comparison of the surface of the virtual bone and the 3D SR μ CT image. The surface of the synthetic bone is smoother than the real one.

A similar evaluation of the texture is done using μ MR images.

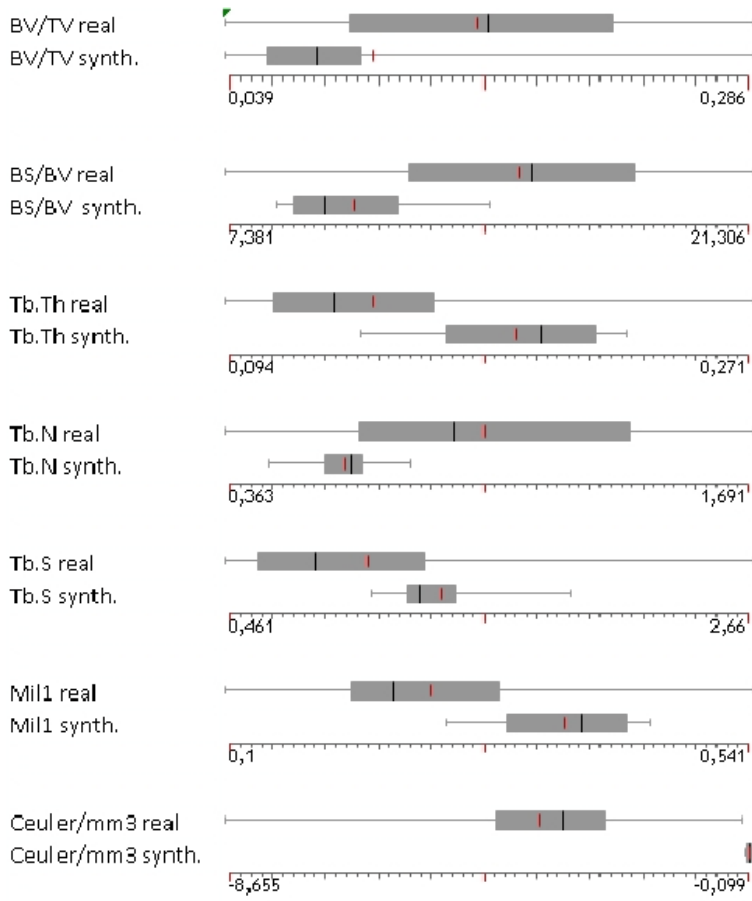


Figure 4.15: Boxplots of morphological and topological bone parameters computed from real and synthetic μ MR images.

The accuracy of the virtual images is assessed by comparing the bone parameters computed from the set of μ MR images with those computed from synthetic ones. Figure 4.15 displays the boxplots associated to each bone parameter obtained from the sets of real and virtual μ MR images.

Figure 4.10 shows the segmented trabecular bones from the 3D virtual μ MR images and those obtained from the 3D μ MR image from which were taken the reference slices for the texture synthesis. Once again the syntetic structure is smoother than the original sample image.

4.6 Conclusion

The method allows one to create organic tissue from small samples acquired by a digital microscope or other image acquisition devices such as SR μ CT, μ MR. The quality of the textures was demonstrated quantitatively from both statistical and morphological points of view. The morphological analysis showed a lower quality of synthesized bone.

This texture synthesis approach is able to preserve the statistical information with accuracy and the morphology of the given sample in a lower degree. Even though the computed morphological parameters were inside the range of plausible values, the quality of the bone is degraded. If the synthesized volumetric object must preserve structure, a procedural approach to synthesize texture might be a better option than the approaches

using 2D samples of texture. As mentioned in the introduction of this chapter, procedural approaches are difficult to parameterize.

The following chapter explains MRI simulation and the procedure to acquire the textured samples for some brain structures. To produce simulated MRI, textured samples containing information of physical parameters are used. These samples of physical parameters do not contain structural information, so the proposed approach can be used to produce volumes of physical parameters.

The solid textures are combined with s-reps (see Section 2.3) to enhance their properties and enable MRI simulation.

5

MRI simulation of the brain using textured s-reps

5.1 Introduction

Medical imaging consists of acquiring details of the interior of the human body with different techniques. Among these techniques we find MRI (magnetic resonance imaging), CT (computed tomography), US (ultrasound) and PET (positron emission tomography). The information acquired using these techniques is widely used in the medical domain to diagnose and plan treatments for patients.

Each technique has complex and expensive imaging devices. They require regular maintenance and are used only by specialized staff. In order to calibrate a device for a specific type of acquisition, there is a large number of parameters that need to be set. There has been research on methods and techniques to optimize these parameters. Depending on the organs in the human body we need to study, varying the input parameters will produce more or less contrast among organ tissues. Acquiring details in the image for specific organs or regions requires understanding the effect of each parameter in the acquisition.

It is not possible to use human patients as imaging targets to optimize an imaging device. This is due to lack of knowledge about the scene. There is no way to know beforehand the disposition of the elements inside a human body. Another option is to use physical phantoms. Unfortunately, they are impractical because they cannot duplicate in-vivo conditions.

Besides the optimization issues, the data produced by these devices might be reserved for medical diagnosis only. This renders the data unavailable for research purposes and poses a challenging problem for calibrating the image acquisition devices.

An image simulation approach could be used to solve both issues. It can be used to optimize a set of image acquisition parameters, or it can be used to produce low cost datasets of an image modality.

There are two basic approaches for image simulation. The first one consists of applying the physics present in the acquisition process to a digital model [Charpigny *et al.* (2009)]. This technique has an advantage because the digital model provides a gold standard that can be used afterwards to validate and improve segmentation or quantification algorithms. The second approach is related to texture synthesis. Texture synthesis is useful to mimic mammograms [Castella *et al.* (2008)] and possibly other types of imaging modalities.

The first type of approach needs two components to produce a simulated image: object model (geometry and physical parameter distribution) and image simulators.

Object models contain information about anatomy, pathology and physiology. They

might be dynamic, and they must be parameterized according to the image modality we wish to obtain. Some physical parameters to perform a simulation could be radioactivity, chemical composition, magnetic properties, etc.

In order to produce convincing simulated images, the virtual object must be as close as possible to a real world object. Some attempts have been made to produce simulated images using deformable models [Segars *et al.* (2008)], [Le Maitre *et al.* (2009)], [Tobon-Gomez *et al.* (2011)]. The challenge of using a deformable model is to estimate the physical parameter distribution inside the object. A second challenge is related to shape modeling of human morphology. As explained in Chapter 2, there has not been a well established methodology to model shape, or to compute statistics that capture shape variability across a population of objects.

An alternative to image simulation with deformable models is to use acquisitions that estimate the physical parameter distribution for the organ tissues; the geometry and physical properties can be used to run the simulation. This approach produces realistic images, but a previous acquisition is always needed to simulate new data. In the case of MRI simulation, the physical parameters are estimated with relaxometry techniques and the acquisitions can be used to produce simulated images.

The *VIP* (Virtual Imaging Platform) is a web platform for multi-modality medical image simulation [Marion *et al.* (2011)], [Glatard *et al.* (2011)]. The objectives of the *VIP* are to provide access to high computing resources; to facilitate access to the simulation software; and to share models created by the users.

The *VIP* provides access to simulators of different medical imaging modalities. The following simulators are available: FIELD-II for Ultrasound imaging (US) [Jensen (2004)]; PET-Sorteo for Positron Emission Tomography (PET) [Reilhac *et al.* (2004)]; Sindbad for Computed Tomography (CT) [Tabary *et al.* (2009)]; SIMRI [Benoit-Cattin *et al.* (2005)] and SimuBloch [Cao *et al.*], both for Magnetic Resonance Imaging (MRI).

In this dissertation, an MRI simulation of the brain is done using a digital model and an image simulator. The deformable model explained in Section 2.3.3 named s-reps is used to model the following brain structures: amygdala, caudate, hippocampus, lateral ventricles, pallidum, putamen and cortex (see Chapter 3 for the procedure to create an srep of the cortex). The texture synthesis algorithm developed in Chapter 4 is used to generate a distribution of physical parameters for each brain structure. Each srep model is textured with the corresponding physical parameters. When all structures are textured, they are merged into a volumetric image that contains the distribution of physical parameters of each structure.

The following section gives an overview of the simulator. Section 5.3 explains how to apply a texture to an srep. Some examples are shown using RGB images followed by examples using images of physical parameters.

After the texturing, the models are merged and provided to *SimuBloch*. The result is a simulated MRI from s-reps and texture synthesis. Section 5.4 evaluates the MRI by running the segmentation pipeline of *Freesurfer* (an automated tool for brain's cortical surface reconstruction using structural MRI data).

5.2 Overview of *SimuBloch*

SimuBloch is an MRI simulator developed by [Cao *et al.*]. The purpose of *SimuBloch* is to validate MRIs of molecular neuro-inflammation within Multiple Sclerosis lesions.

An MR relaxometry technique is used to acquire the values of the four physical parameters needed to produce simulated images. The parameters are as follows:

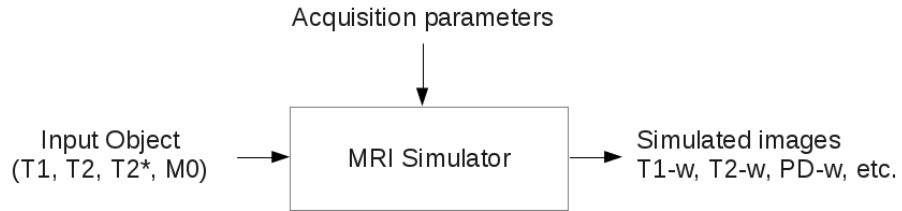


Figure 5.1: Simulation workflow for *SimuBloch*. The input object is composed by image volumes of $T1$, $T2$, $T2^*$ and $M0$. Depending on the acquisition parameters, different outputs can be generated.

- $T1$ or the relaxation constant measuring how fast the spinning nuclei will emit their absorbed RF into the surrounding tissue.
- $T2$ or the relaxation constant measuring the time needed for the protons found in water molecules in biological tissue to return to equilibrium.
- $T2^*$ or field inhomogeneity. The field inhomogeneity is the principal cause of image distortion and signal loss.
- $M0$ or proton density ρ , measuring the mobile hydrogen atoms in the tissue.

SimuBloch uses the physical parameters of materials to produce simulated images. Each of the parameters are provided to *SimuBloch* using 3D images. Each voxel contains the physical parameter needed to compute the local spin magnetization.

Using the physical parameters, the simulator is able to compute various types of acquisitions including $T1$ -weighted, $T2$ -weighted, PD -weighted, FLAIR, etc. similar to the sequences implemented in a real device.

Figure 5.1 explains the workflow of a simulation.

SimuBloch is available to use on the *VIP*¹ platform. A test case is available on the *VIP*. It has three images of physical parameters: $T1$, $T2$, and $M0$. Figure 5.2 shows a slice of the image of physical parameters and the result of *SimuBloch*. The result image is a $T1$ -weighted acquisition with $TR = 500$ and $TE = 8.4$.

The following section explains how to generate simulated physical parameters images from s-reps and solid texture synthesis.

5.3 Texturing s-reps

The texture synthesis algorithm developed in Section 4.3 uses 2D textured images to create solid blocks of texture. The procedure keeps the statistical features of the sample (this was shown in Section 4.5) and some structural features as well.

The solid blocks or cuboids can be warped into an s-rep using an $X2U$ map (see Section 2.4.3 for a review on $X2U$ maps and the object coordinates $U = [u, v, \tau]$). The $X2U$ map parameterizes every position inside the s-rep with the $[u, v, \tau]$ coordinate system. These coordinates can be modified to map the length, width and height of the cuboid. In other words, a function is designed to map every position in the s-rep to a position in the cuboid.

The following section explains how the mapping is done. RGB textures with different patterns are warped into s-reps to help understand the procedure.

¹<http://vip.creatis.insa-lyon.fr/>

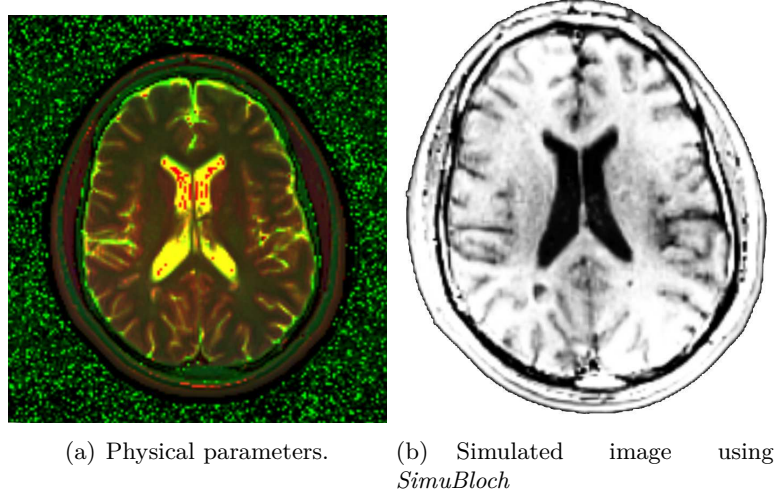


Figure 5.2: The physical parameters from *SimuBloch* are composed into a single image. $T1$ is shown in red, $T2$ in green and $M0$ in blue. All channels are rescaled between $[0 - 255]$ for visualization purposes. The simulated image is a $T1w$ with acquisition parameters of $TR = 500$ $TE = 8.4$.

Section 5.3.2 explains how to extract 2D samples of physical parameters that can be used to synthesize solids. The resulting solids are warped to s-rep models in order to enhance their internal properties with physical parameters.

The s-rep models are from different subcortical structures and the cortex. The enhanced representations are used to produce MRI simulated images with *SimuBloch*.

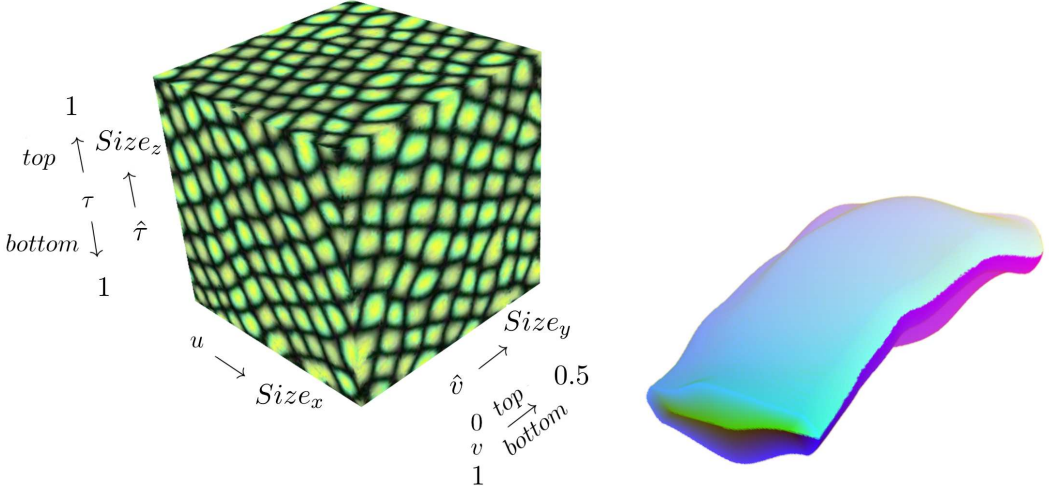
5.3.1 Warping RGB textures

To warp a solid texture, every position inside the s-rep with coordinates $[u, v, \tau]$ is assigned a corresponding position in a solid block of texture. Since the synthesis procedure is done inside a cuboid of arbitrary size $(Size_x, Size_y, Size_z)$, the objective is to design a function $U2C$ such that $U2C(u, v, \tau) = \{[s_x, s_y, s_z] : s_{x,y,z} \in [0, Size_{x,y,z}] \}$. In other words, each internal coordinate of the s-rep has a corresponding position in the cuboid.

As explained in Section 2.4.3, there are two functions that allows going from world coordinates to object coordinates and vice versa, namely $X2U(x, y, z) = [u, v, \tau]$ and $U2X(u, v, \tau) = [x, y, z]$. An $X2U$ map stores the coordinates $[u, v, \tau] \in [0, N], N = 1$ of an s-rep at every world coordinate $[x, y, z]$. Recall that in object coordinates, v wraps around the object ($v \in [0, 0.5]$ for the top side of the s-rep and $v \in [0.5, 1]$ for the bottom side of the s-rep) and τ maps from $\tau = 0$ at the SS (skeletal sheet) to the object's boundary at $\tau = 1$.

The function $U2C$ uses a modified version of the v and τ coordinates in order to provide continuity of the solid texture inside the s-rep. v is modified to map the top and bottom sides of the object to the width of the solid, and τ is modified to start at half the height of the cuboid. The top side of the s-rep will map to the upper part of the cuboid while the bottom side of the s-rep will map to the lower part of the cuboid. This is done in two steps: mapping v and τ to the variables \hat{v} and $\hat{\tau}$ and then mapping $[u, \hat{v}, \hat{\tau}]$ to $[s_x, s_y, s_z]$.

\hat{v} and $\hat{\tau}$ map to the width and height of the cuboid as shown in Equations 5.1 and 5.1 respectively. Both transformations depend on the side of the skeletal sheet parameterized by $v < 0.5$ for the top and $v > 0.5$ for the bottom. The u coordinate is not modified and



(a) Mapping the solid texture to the s-rep with the $X2U$ map. The values of v and τ are modified to enforce the continuity of the solid inside the object.

(b) Volume rendering of an $X2U$ map of the s-rep. The map is sliced to reveal the internal color gradient where the u , v and τ are colored with red, green and blue.

Figure 5.3: The $X2U$ map is used to warp the solid texture inside the object. The $[u, v, \tau]$ coordinates are transformed into $[u, \hat{v}, \hat{\tau}]$ mapping the length, width and height of the cuboid.

maps the length of the cuboid.

Figure 5.3-a shows how to modify the $[u, v, \tau]$ coordinates. Figure 5.3-b shows the volume rendering of the $X2U$ map where the coordinates $[u, v, \tau]$ are colored with red, green and blue respectively (the $X2U$ map is sliced to reveal the internal gradient).

The size ($Size_x, Size_y, Size_z$) of the cuboid should be chosen according to the s-rep physical dimensions. This is done to preserve the structural information of the texture as it might be distorted during the texture warp. This issue arises when the cuboid and the s-rep differ in physical size. Equation 5.3 shows how to modify the coordinates according to the solid's size.

$$\hat{v} = \begin{cases} 2v, & v < 0.5 \\ 2(1-v), & \text{otherwise} \end{cases} \quad (5.1)$$

$$\hat{\tau} = \begin{cases} 0.5 + \tau/2, & v < 0.5 \\ 0.5 - \tau/2, & \text{otherwise} \end{cases} \quad (5.2)$$

$$U2C(u, v, \tau) = (u, \hat{v}, \hat{\tau}) \begin{bmatrix} Size_x & 0 & 0 \\ 0 & Size_y & 0 \\ 0 & 0 & Size_z \end{bmatrix} = [s_x, s_y, s_z]. \quad (5.3)$$

The complete set of functions enables going from world coordinates $[x, y, z] \xrightarrow{X2U} [u, v, \tau]$ to s-rep coordinates and from s-rep coordinates $[u, v, \tau] \xrightarrow{U2C} [s_x, s_y, s_z]$ to the cuboid. Therefore, every s-rep internal position has a corresponding position in the solid. By querying world coordinates, the information in the solid texture can be retrieved allowing the texture warp.

A solid texture of size (256, 128, 64) was synthesized and warped to an s-rep. The structural features are preserved as shown in Figure 5.4 with the volume rendering representation.

Figure 5.5 shows a volume rendering representation of the cortex using a zebra and a dot texture. The size of the solid texture is [4096, 4096, 32]. The tubular structure mimics the cortical columns running perpendicular to the cortical surface (see Chapter 3 for a review of cortical columns).

The following section explains how to extract 2D samples of physical parameters. The exemplars are used to generate solid textures that can be warped into an s-rep with the procedure just explained.

The s-reps are from the following brain structures: amygdala, caudate, hippocampus, lateral ventricles, pallidum, putamen and cortex.

Additionally, the s-rep of the cortex is used to locate the WM (white matter) and cerebral spinal fluid regions in the brain.

Each s-rep and brain region is textured individually, and then they are merged into a single image. The result is a volumetric image with multiple components, $T1$, $T2$ and $M0$, the parameters needed to produce a simulated $T1$ -weighted image.

5.3.2 MRI simulation with textures of physical parameters

The first step towards MRI simulation is to generate 2D samples of physical parameters. The exemplars are extracted from a relaxometry image measuring the physical properties of brain tissues. The brain structures considered are the following: amygdala, caudate, hippocampus, lateral ventricles, pallidum, putamen, cortex, WM and cerebral spinal fluid. Each of the generated 2D samples will be provided to the texture synthesis algorithm in order to create solid textures of physical parameters.

Unfortunately, acquiring accurate exemplars is out of the scope of this dissertation. For the purpose of demonstrating the capabilities of s-reps and the texture synthesis procedure, simple 2D image samples of physical parameters are created from a relaxometry acquisition available at *VIP* [Cao *et al.*].

This image of physical parameters shown in Figure 5.2-a. Figure 5.2-b shows the corresponding simulated image with *SimuBloch*. To locate each brain structure in the image of physical parameters, the simulated MRI is segmented with *Freesurfer*. The segmentation provides binary masks that can be used to locate the subcortical structures, the cortex, the WM and the cerebral spinal fluid.

The 2D samples are created by randomly choosing a position inside the brain structure (with help of the binary mask) and copying neighborhoods of size 3×3 to the image sample. The procedure continues until the exemplar is covered completely.

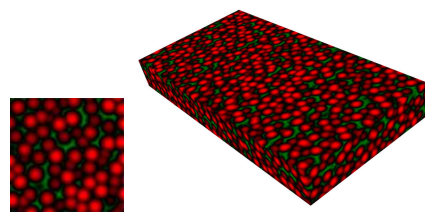
Figure 5.6 shows the exemplars of physical parameters, the size of the images is 128^2 pixels. All the generated exemplars are used to synthesize solid textures.

S-reps of subcortical structures are fitted to three different datasets previously segmented by *Freesurfer*. The fitting procedure is described in Section 2.3.3. The hemispheres of the cortex are generated with the procedure described in Section 3.2.

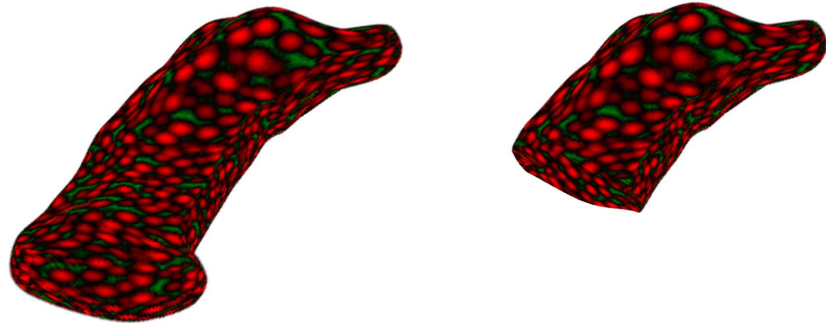
As mentioned before, the s-rep of the cortex is used to locate the region corresponding to the WM. To locate this region, the $X2U$ map of the cortex is extended in the τ direction. In other words, the outside region of the cortex is coded with $\tau > 1$.

Recall that the v coordinate codes the top and bottom regions of the s-rep. For values of $v < 0.5$ and $\tau > 1$ we can reach the folds produced by the GM surface, and for $v > 0.5$ and $\tau > 1$ we can reach the WM region. Using the extended $X2U$ map, the WM region is located and a binary image that has the shape of the WM is generated.

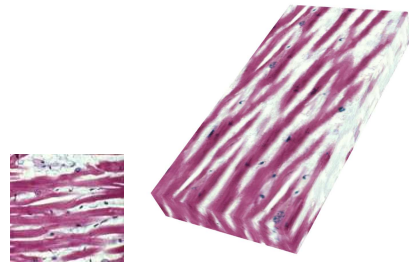
The binary mask can be used to “carve” WM texture out of the cuboid. The cuboid has equal size to the binary image of the WM region and all non-zero voxels are textured



(a) Sample and volume.



(b) Volume rendering

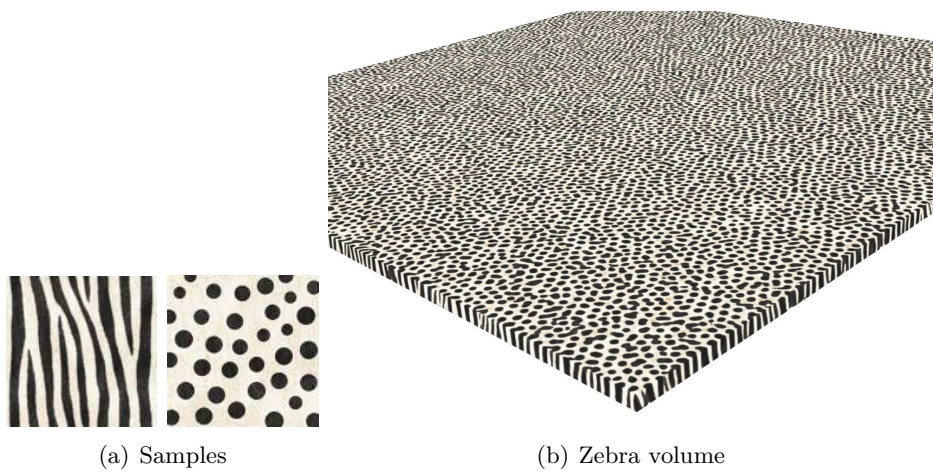


(c) Sample and volume.



(d) Volume rendering

Figure 5.4: Volume rendering of an textured s-rep. The size of the synthesized texture is (256, 128, 64). The texture is warped inside the object using the $X2U$ map of the s-rep and is cut at a random location revealing internal features.



(a) Samples

(b) Zebra volume



(c) Volume rendering of an s-rep of the cortex using the zebra texture.

Figure 5.5: The size of the synthesized solid is [4096, 4096, 32]. The texture is warped inside the object using the $X2U$ map. In this case the cylinders from the texture run perpendicular to the cortical surface. Similar to the cortical columns explained in Chapter 3.

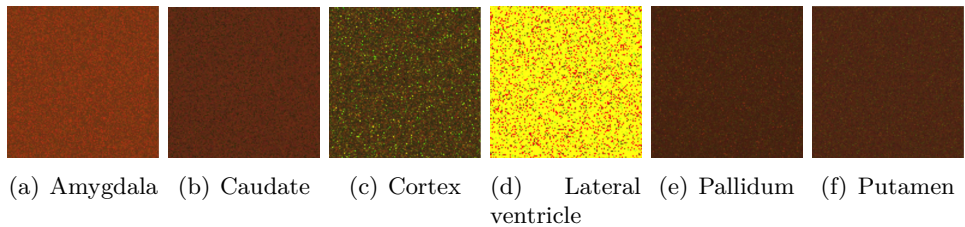


Figure 5.6: Samples of physical parameters for the brain structures. The noise from the samples is reduced with a Gaussian filter ($\sigma = 0.5$).

with the information in the cuboid.

The outer region of the implied GM surface is textured with cerebral spinal fluid in a similar manner.

All textured objects are merged into a single 3D image in the following order: WM, cerebral spinal fluid, cortex and subcortical structures. The resulting volume has three components ($T1, T2$ and $M0$) and the geometry of the brain structures. *SimuBloch* can produce a simulated $T1$ -weighted image using the generated volume of physical parameters.

Figure 5.8 shows three cases to test the simulation procedure. The following section evaluates the quality of the simulated images.

5.4 Evaluation of the simulated image

To evaluate the quality of the images, a segmentation with *Freesurfer* is performed. If these images are close enough to real MRI acquisitions, they should be able to be segmented by *Freesurfer*. Figure 5.9 shows the result of the simulation with *SimuBloch*. The simulation parameters of the acquisition were $TR = 500$ and $TE = 8.4$.

As expected, *Freesurfer* is able to segment the images and produces a cortical parcellation and subcortical labeling of structures. The results of the segmentation are shown in Figure 5.11. The image shows the WM and GM surfaces in yellow and cyan respectively; the labels given to the subcortical structures; and the cortical parcellation.

A curvature map illustrates the degree of curviness in a surface. In the case of the cortex, the map shows in green the areas of high convexity and in red the areas with high concavity. This corresponds to the gyri and sulci respectively.

Figures 5.12, 5.13, and 5.14 show the curvature map of the cortical surfaces for Subjects 1, 2 and 3 respectively. The images on the left column correspond to the simulated data and the images on the right column correspond to the real data (the data used to fit the s-reps). The images are similar but not identical. In some cases, the cortex seems to be thinner or the regions in the cortex are under- or over-segmented by *Freesurfer*. Nevertheless, these disagreements are quite small.

The following section gives a conclusion of the image simulation approach.

5.5 Conclusions

In conclusion, the approach is successful as indicated by the fact that the images can be segmented by *Freesurfer*. The cortical surfaces are reconstructed from the simulated data and globally, the cortical surfaces are similar to the real data but local differences can be detected between the images. Moreover, the simulated images are generated from

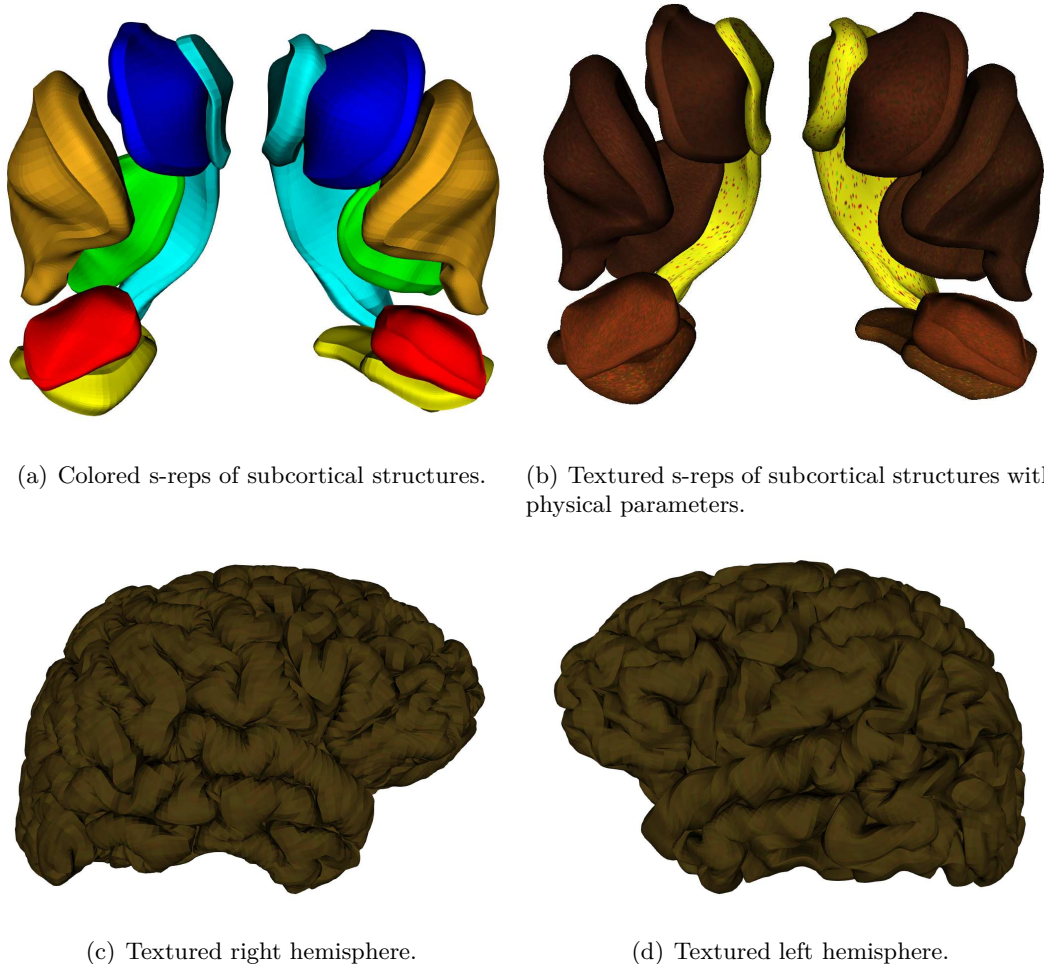


Figure 5.7: Multi-object complex of sub-cortical structures for the left and right hemispheres. The subcortical structures shown are: amygdala, caudate, hippocampus, lateral ventricle, putamen and pallidum. They are shown respectively in Figure (a) in colors: red, blue, yellow, cyan, dark yellow and green. Figure (b) shows the textured s-reps with physical parameters. Figures (c) and (d) show the right and left hemispheres of the cortex.

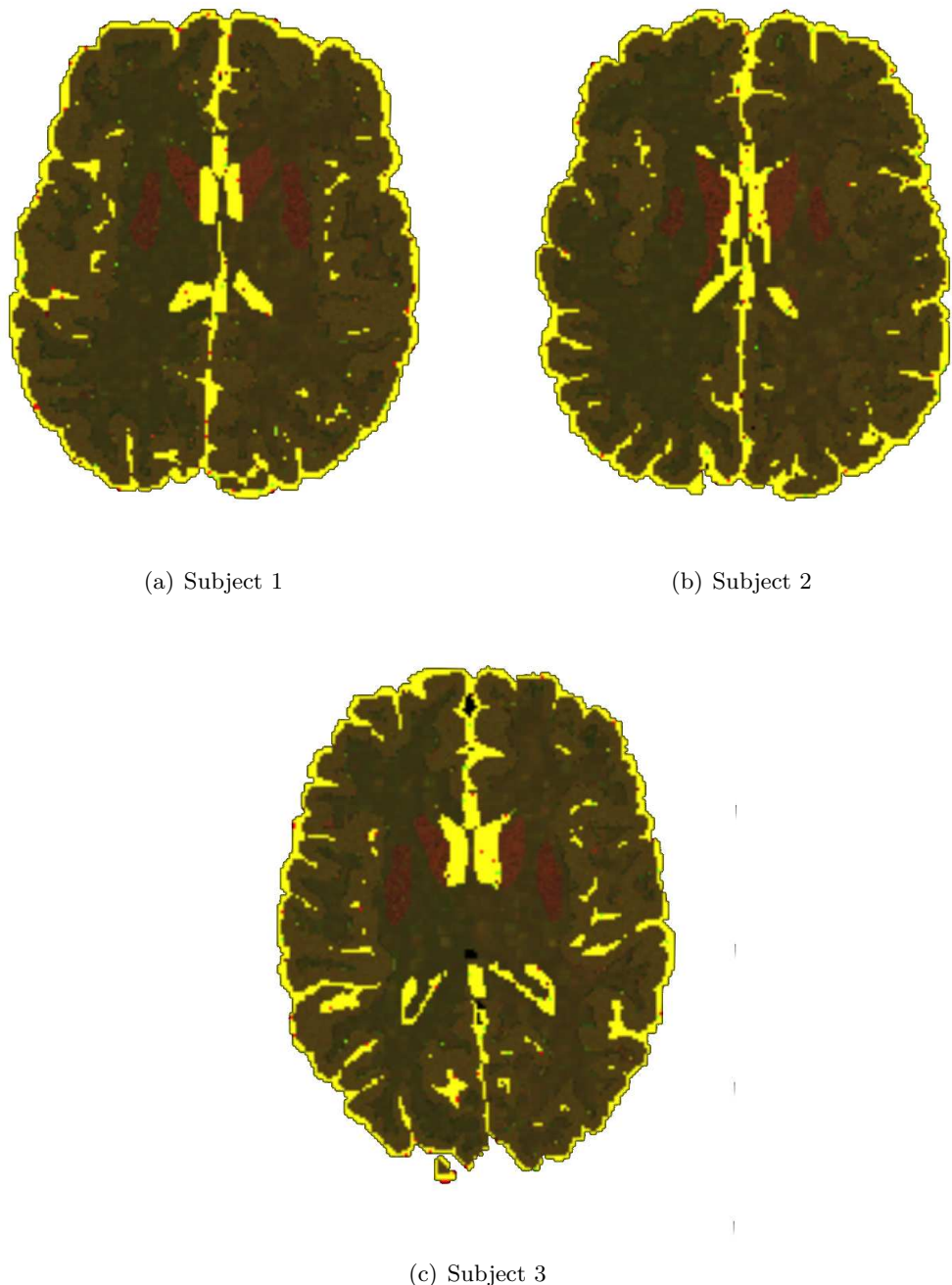
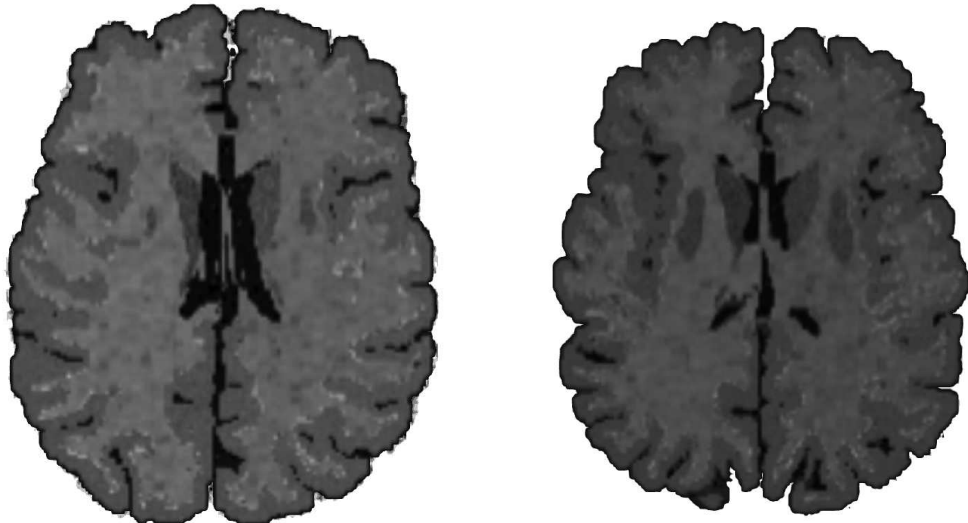
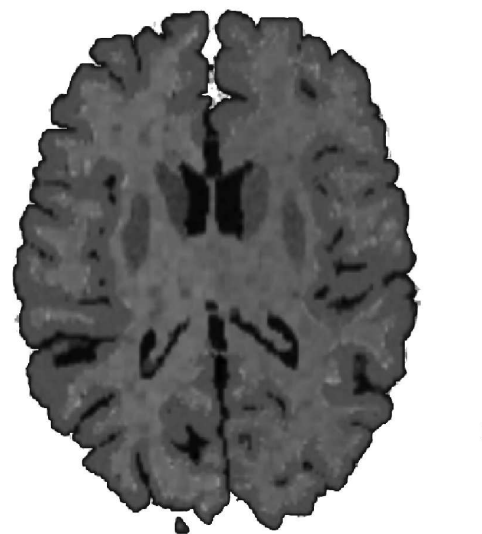


Figure 5.8: The textured s-reps can generate an image of physical parameters by merging the results into a single image. The WM and cerebral spinal fluid regions are textured with the extended $X2U$ map of the cortex. Figures (a) to (c) show the results of merging the solid textures into a single image. $T1$ is shown in red, $T2$ in green and $M0$ in blue. All channels are rescaled between $[0 - 255]$ for visualization purposes.



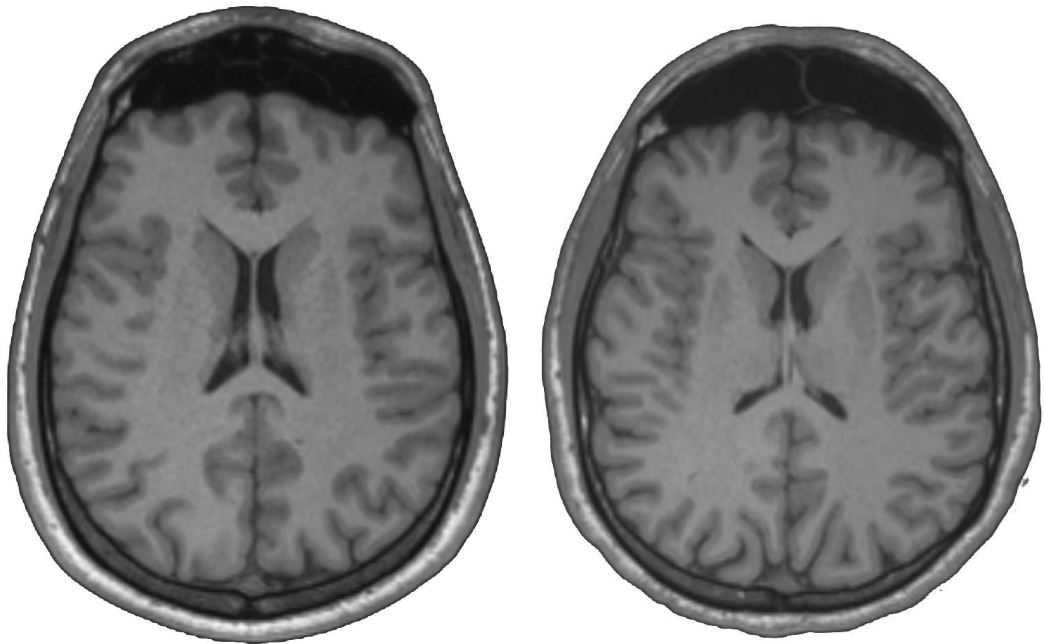
(a) Subject 1

(b) Subject 2



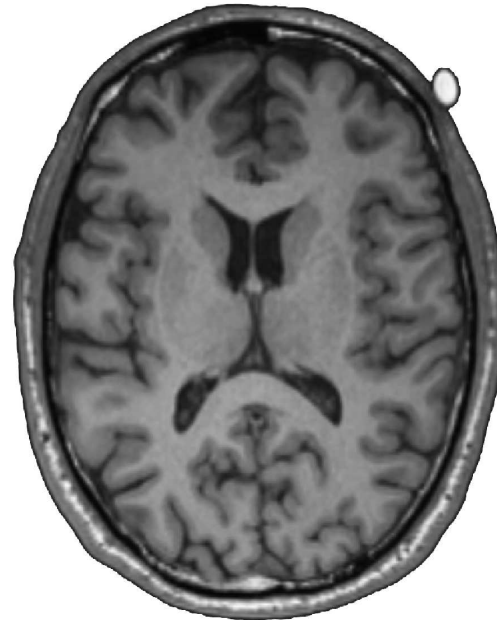
(c) Subject 3

Figure 5.9: Result of *SimuBloch* using the physical parameters image shown in Figure 5.8.



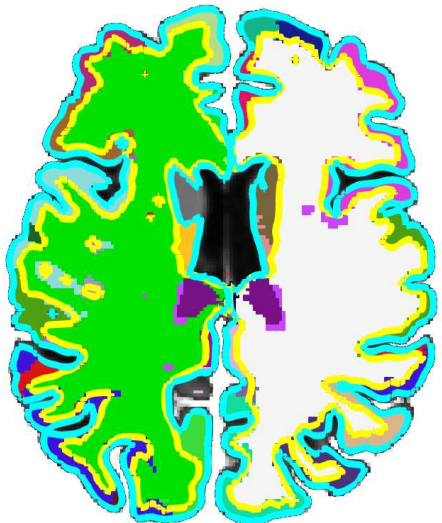
(a) Subject 1

(b) Subject 2

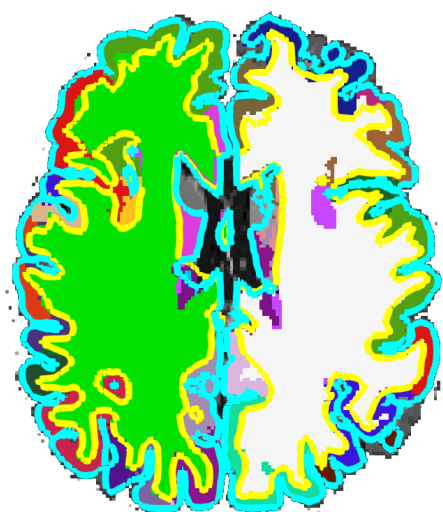


(c) Subject 3

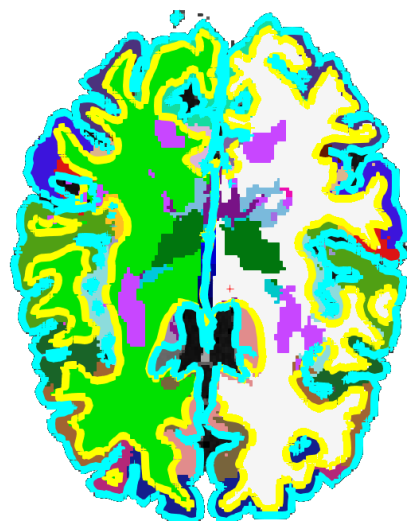
Figure 5.10: The source images used to create the s-rep models. The slices resemble those shown in Figure 5.9, i.e., the simulated images.



(a) Subject 1

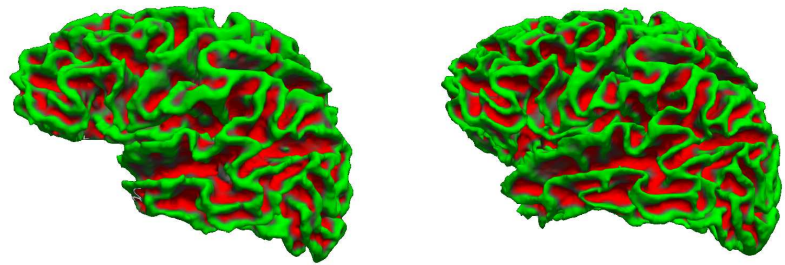


(b) Subject 2

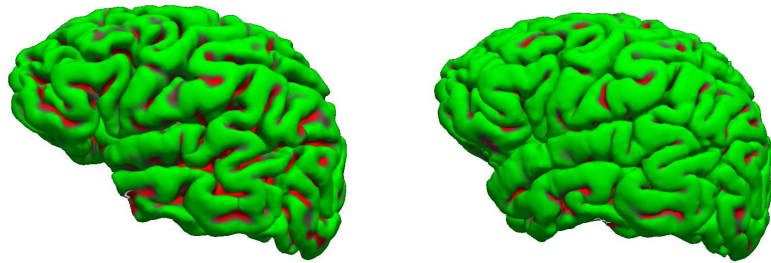


(c) Subject 3

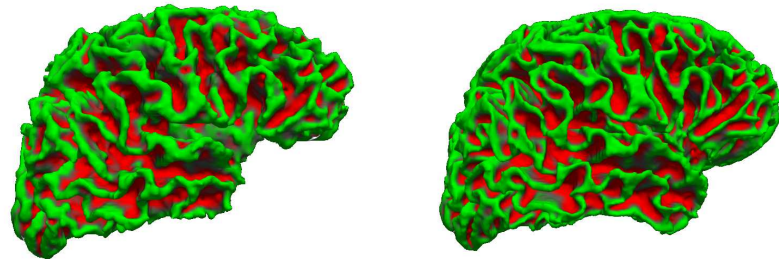
Figure 5.11: Result of *Freesurfer*. Freeview (a visualization tool from *Freesurfer*) is used to visualize the surfaces and the segmented labels of the subcortical structures. The yellow line corresponds to the WM surface and the red line to the GM surface.



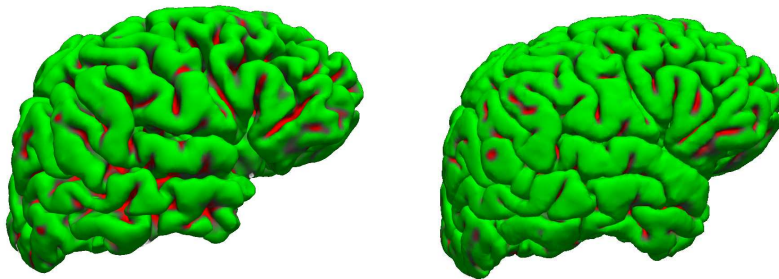
(a) Left hemisphere WM surface.



(b) Left hemisphere GM surface.

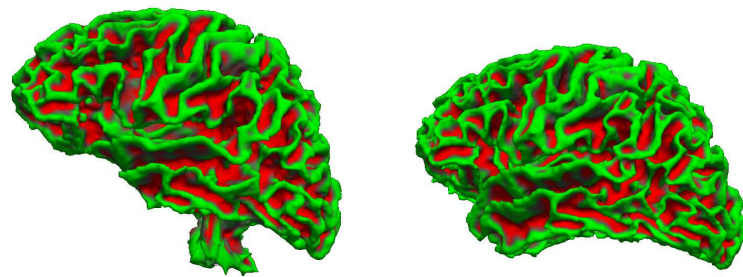


(c) Right hemisphere WM surface.

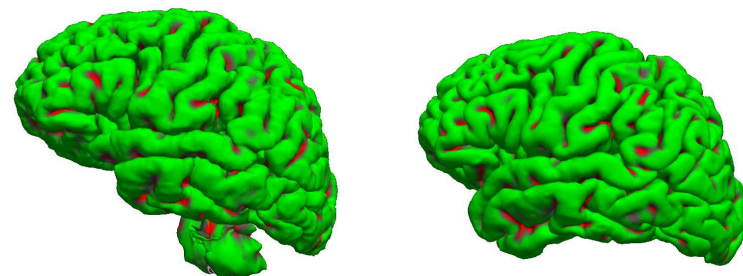


(d) Right hemisphere GM surface.

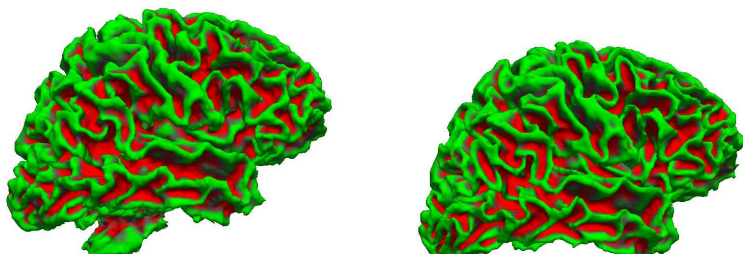
Figure 5.12: Subject 1. Visualisation of curvature map for the WM surface and the GM surface in the left and right hemispheres of the cortex. The images on the left column correspond to the simulated MRI segmented by *Freesurfer*. The images on the right column correspond to the real MRI segmented by *Freesurfer*. The global structure of the cortex is preserved. However, some differences can be seen as the segmentation of the simulated cortex seems thinner. Also, the segmentation does not fully segment the superior temporal and middle temporal regions of the cortex.



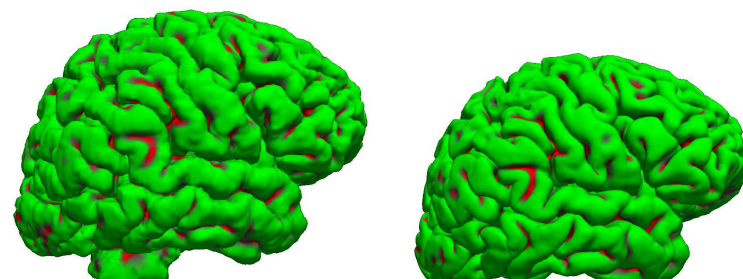
(a) Left hemisphere WM surface.



(b) Left hemisphere GM surface.

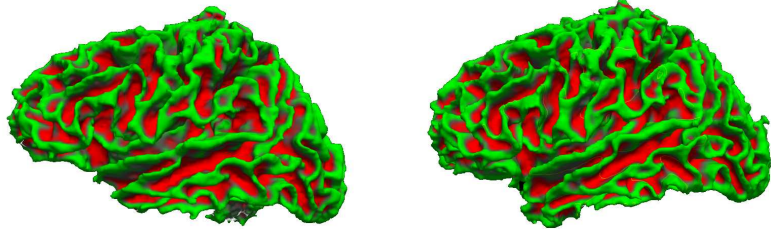


(c) Right hemisphere WM surface.

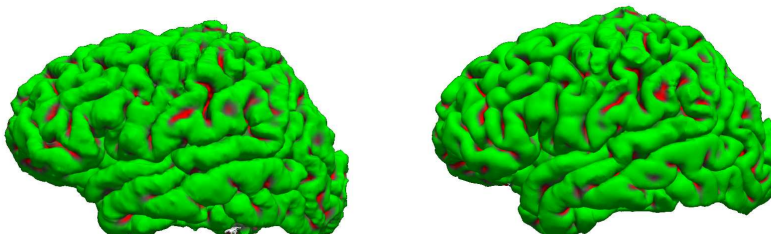


(d) Right hemisphere GM surface.

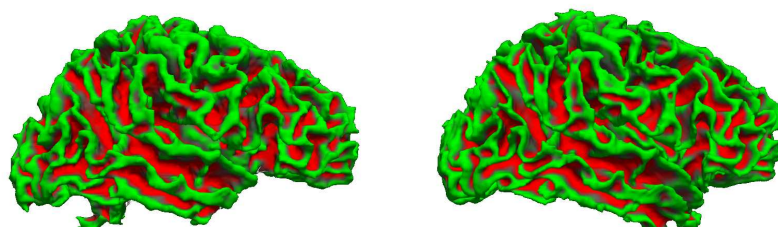
Figure 5.13: Subject 2. Visualisation of curvature map for the WM surface and the GM surface in the left and right hemispheres of the cortex. The images on the left column correspond to the simulated MRI segmented by *Freesurfer*. The images on the right column correspond to the real MRI segmented by *Freesurfer*. The global structure of the cortex is preserved. However, the segmentation produces an artifact at the base of the cortical surfaces.



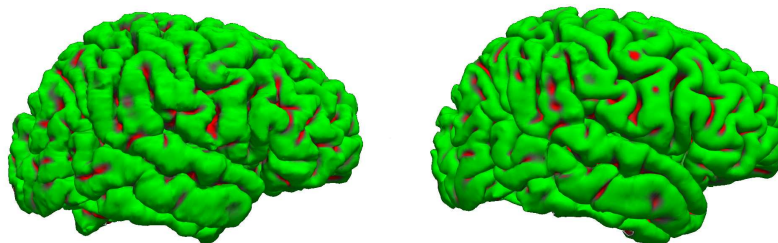
(a) Left hemisphere WM surface.



(b) Left hemisphere GM surface.



(c) Right hemisphere WM surface.



(d) Right hemisphere GM surface.

Figure 5.14: Subject 3. Visualisation of curvature map for the WM surface and the GM surface in the left and right hemispheres of the cortex.

The images on the left column correspond to the simulated MRI segmented by *Freesurfer*. The images on the right column correspond to the real MRI segmented by *Freesurfer*. Some local differences can be detected between the surfaces, but the overall structure of the cortex is preserved.

deformable models and textures lacking structural information. If the samples have structure, the texture synthesis algorithm can be used to its full potential and the results are likely to improve.

A single acquisition of physical parameters suffices to produce three new MRIs, but extracting the textured samples was a difficult task due to low image resolution. [Charpigny *et al.* (2009)] uses a label mask corresponding to the type of organ tissue, an average value and a standard deviation to generate the physical parameter distribution. Following this logic, the image samples of physical parameters were created by sampling voxels inside the brain structures. Each sample is representative of each tissue. As shown by the results, the simulated images with the physical parameters were able to 'trick' the segmentation pipeline of *Freesurfer*.

Future work aims to improve the image samples of physical parameters. This images should have the values of physical parameters and the appropriate texture distribution according to each brain structure being modeled. The $X2U$ map can also be used to texture the objects locally. Instead of having a single sample for a brain structure, different samples can be used to texture the regions in the brain structure accordingly.

A second objective seeks to generate statistical descriptions of shape for the subcortical structures and the cortex using s-reps and CPNS. The statistical descriptions will model healthy and pathological shape variations for the subcortical structures and the cortex. New brain structures can be generated from the statistics allowing the combination of shapes from healthy and disease populations.

The following chapter gives a global conclusion for this dissertation and proposes future work according to the results found in these experiments.

6

Conclusions and perspectives

6.1 Synopsis of the work

The principal objective of this dissertation was to propose a technique able to model internal and external features of organs. Describing internal features and surface characteristics closes the gap between virtual objects and objects in the real world. Objects with such characteristics are needed to improve existent simulation procedures.

After reviewing the state of the art techniques for shape modeling, it can be concluded that s-reps provide features superior to other techniques. One of the most important characteristic of this technique is the possibility to describe the interior of an object. This quality was widely used through this dissertation. It allows including information from different spatial scales or sources such as histology images and/or physical parameters.

To prove the capabilities of s-reps, the human brain became the target organ to be modeled. From this task came the most important contribution of this dissertation, which is the procedure to model the cerebral cortex using s-reps.

The cerebral cortex has never been modeled with techniques describing internal features. From now on, a single non-branching object can be used to describe both cortical surfaces plus the interior. S-reps provide new ways to analyze cortical columns and analyze cortical lesions in a different parametric space.

Besides describing the shape of the cortex, it was proven that a population of cortices can be described by a mean shape, a set of eigenmodes and some coefficients. CPNS and the cortex representation enabled a compact representation or a statistical description of thickness variations in the cortex.

The second objective of this dissertation, *i.e.*, to provide a mechanism to model the volumetric properties of an object, was fulfilled with a method to synthesize solids. This technique is compatible with s-reps and allows describing the interior of the object using parameters from various sources such as: RGB textured images; images from histology; images from μMR and μCT ; and physical parameters.

A simulation of the brain was done using the techniques just described. S-reps of the subcortical structures were fitted to real MRI images segmented with *Freesurfer*. The subcortical structures include: amygdala, caudate, hippocampus, lateral ventricles, pallidum and putamen.

Using this set of s-reps, the internal properties of the objects were enhanced with textures of physical parameters. MRI images were simulated using the virtual object and *SimuBloch*. The MRIs were validated using the automatic segmentation procedure proposed by *Freesurfer*.

6.2 Future work

There are three possibilities identified for future work. Improvement of the statistical shape description of the cortex, improvement of the simulation framework and working towards the establishment of a technique to estimate scalar features based on shape descriptions.

The shape description of the cortex with s-reps and CPNS could provide new research opportunities to analyze shape variability in control and pathological subjects for crosswise (multiple subjects) and longitudinal (same subject but multiple acquisitions) scenarios. The shape description of the cortex could help researchers understand brain development and to identify the principal shape variations as the human brain grows.

The simulation framework can be improved by acquiring better textured samples of physical parameters and generating statistical shape descriptions of the organ structures modeled with s-reps.

As mentioned in Section 5.5 the full potential of the approach to simulate images is not achieved. The textured samples do not contain structural information and they have a low resolution.

With the statistical shape descriptions of organs, a completely different set of structures can be generated using a few coefficients. Control and pathological shapes can be combined to produce new simulated images.

There are two major applications for this framework, the optimization of image acquisition parameters and the validation of segmentation algorithms.

Finally, a methodology to estimate scalar features based on shape description needs to be established. For example, we wish to estimate the gray matter anisotropies in thalamic nuclei based on a fitted srep to the structure and clinical resolution DTI images.

The nuclei are only visible in a high resolution DTI acquisition. Unfortunately, this acquisition cannot be done routinely. In order to identify this feature, a set of patients with DTI and T_1 -weighted image acquisitions will be used in the study.

The procedure will use the T_1 -weighted images to fit s-reps. The fitting produces tight representations of an srep and increases the correspondence between internal positions $[u, v, \tau]$ among thalami.

Shape statistics will be computed using CPNS, and a statistical analysis will be done for the nuclei density using the coordinate system $[u, v, \tau]$. This is possible since the internal positions are in correspondence.

The statistics will contain shape and nuclei density descriptions for each position inside the srep.

To estimate the nuclei density in a new thalamus, the mean shape produced by CPNS is fitted to the structure. The nuclei density can be estimated based on the shape deformation and the density statistical description.

This approach could be used to detect other type of scalar features.

7

Résumé de thèse

7.1 Introduction

Les progrès récents sur les modalités d'imagerie et de calcul numériques ont ouvert un nouveau domaine d'étude de la variabilité biologique de l'anatomie humaine. Ce nouveau domaine est appelé l'*anatomie computationnelle* (CA).

La CA, telle que définie par [Grenander and Miller (1998)], possède trois aspects principaux : construction de formes anatomiques ou modélisation par des points, des courbes, des surfaces et des volumes ; comparaison de ces modèles ; et l'analyse statistique de la variabilité de forme. Les statistiques permettent de déduire et de tester des hypothèses d'états pathologiques. Cela se fait à l'aide de tests statistiques qui déterminent la probabilité qu'une hypothèse soit vraie ou fausse. Par exemple, un nouvel échantillon pourra être classé comme malade ou sain selon son score.

La construction automatique des modèles anatomiques a été le principal intérêt de nombreux groupes de recherche dans le monde entier. Ces modèles sont basés sur des algorithmes et des équations qui capturent le comportement et/ou l'apparence de l'objet. En plus des tests d'hypothèse, ces modèles sont également utilisés dans différents types de procédures de simulation, par exemple, la simulation d'images médicales.

L'imagerie médicale consiste à acquérir des détails de l'intérieur du corps humain en utilisant différents techniques ou modalités. Parmi ces modalités on retrouve entre autre : l'IRM (imagerie par résonance magnétique), le scanner X, les ultrasons (échographie) et la TEP (tomographie par émission de positons). Elles sont employées couramment en clinique pour diagnostiquer et planifier les traitements des patients avec l'information "vue" dans l'image. Ces dispositifs d'imagerie peuvent être très coûteux, ils nécessitent un entretien régulier et ne peuvent être utilisés que par un personnel qualifié.

Dans ce contexte, la simulation d'image médicale est définie comme le processus de production d'une image de synthèse d'une modalité spécifique à l'aide de la géométrie d'un objet virtuel. L'objet virtuel en question pourrait être un organe ou un système d'organes.

L'un des objectifs de la simulation d'image est l'amélioration des dispositifs d'imagerie. Cela peut se faire quand la simulation améliore la compréhension des phénomènes d'acquisition, ou lorsque la simulation permet d'établir un ensemble spécifique de paramètres pour produire un résultat souhaité. Une fois une simulation réussie, l'expérience peut s'effectuer sur l'appareil réel.

Une autre utilisation des images simulées est l'évaluation de la performance des algorithmes de traitement d'image, dont la segmentation. Avec une image simulée, les résultats d'une segmentation peuvent être comparés directement au modèle d'objets virtuels. D'autres types de simulations sont faites pour mieux comprendre les différents processus

biologiques comme : la déformation du muscle, le cycle cardiaque, le cycle respiratoire, le pliage corticale etc.

Sachant toutes les applications possibles dans le domaine médical, le défi d'aujourd'hui est de créer un être humain virtuel. Pour ce faire, il faut un modèle capable d'intégrer les informations anatomique, physiologique, mécanique, biologique et physique. Cet homme virtuel pourrait servir à améliorer les procédures de simulation et aussi les tests d'hypothèse pour les états pathologiques.

Le premier objectif de cette thèse est de fournir une technique assez générique capable de représenter la forme de divers organes. Cette technique doit être capable d'inclure l'information à différentes échelles spatiales. Il existe de nombreuses approches permettant de modéliser la forme d'un objet. Les modèles déformables sont utilisés couramment et ils sont connus pour leur performance. Ils sont notamment en mesure d'automatiser, dans une certaine mesure, la segmentation de structures sur une image, et ils sont capables de produire des statistiques selon les déformations. Malheureusement, ces techniques ne permettent pas intrinsèquement leur utilisation dans un contexte de simulation réaliste d'organes.

Le deuxième objectif de cette thèse est d'offrir une procédure pour synthétiser des solides, c'est à dire les propriétés de la surface et les propriétés internes de l'objet. La procédure de synthèse utilise des échantillons de petites dimensions extraits d'images de référence. Le résultat synthétisé est visuellement et statistiquement similaire à l'image de référence. Les modèles de texture peuvent provenir de différentes sources telle que des images réelles (CT, IRM ...), l'histologie, ou plus complexes tel que des paramètres physiques. Les solides générés peuvent être utilisés pour améliorer la visualisation et/ou les propriétés internes des modèles créés à l'aide de la technique décrite dans la partie 7.2.

Le troisième objectif est d'utiliser la description géométrique couplée avec les propriétés des paramètres physiques et simuler des images IRM. Ces images sont validées avec des algorithmes de segmentation utilisés couramment.

Ce résumé de thèse est organisé de la façon suivante. La partie 7.2 résume les caractéristiques les plus importantes de la méthode utilisée tout au long de cette thèse pour la modélisation de forme. Cette technique est appelée s-rep. La partie 7.3 présente la contribution plus importante de ce travail de thèse. Il s'agit d'une méthodologie permettant de créer une représentation de cortex. Le modèle s'inspire du fait que la forme réelle du cortex est proche de celle d'une "crêpe" pliée. La plupart des méthodes n'utilisent que l'information surfacique. La partie 7.4 résume la procédure pour synthétiser les solides. La partie 7.6 conclut ce résumé et annonce quelques perspectives à suivre.

7.2 Représentation des objets en 3D

Les progrès technologiques ont permis le développement de modèles 3D de haute qualité. Ces modèles sont utilisés dans divers secteurs de l'industrie. Ils décrivent l'apparence de l'objet d'une façon mathématique et ils peuvent être utilisés dans l'animation, le prototypage et la simulation. La géométrie de l'objet est au cœur de ces procédures.

Aujourd'hui, le défi est de créer des modèles d'objets adaptés pour les procédures de simulations réalistes. Ils doivent fournir les mécanismes permettant d'inclure les informations de diverses sources, à différentes échelles spatiales et permettant également de travailler avec plusieurs objets. En plus, leur forme doit être représentative d'une population. Cela implique la mise en place d'une méthodologie pour calculer la moyenne des formes et une description de la variabilité dans une population. Actuellement, il n'y a aucun formalisme bien établi pour manipuler la forme, ni pour calculer une forme moyenne.

Élaborer un modèle avec les caractéristiques mentionnées ci-dessus, ouvre la possibilité d'améliorer les procédures existantes de simulation; d'acquérir une meilleure compréhension des systèmes du corps humain; d'améliorer l'analyse automatisée sur les images médicales et également d'améliorer la médecine personnalisée. Les interventions médicales (non invasives) pourraient être planifiées à l'aide des modèles "patient spécifique" s'ils ont été créés à partir d'information acquise sur des images médicales. La modélisation 3D se divise en deux catégories : modélisation de surfaces et modélisation de volume. Les modèles de surface représentent la couche externe de l'objet uniquement. Ils sont stockés comme un ensemble de primitives telles que des points, des arêtes ou des polygones qui définissent la frontière de l'objet. Au cours des 20 dernières années, la plupart des recherches en représentation ont été faites sur cette catégorie car plus facile à manipuler. La modélisation des surfaces peut être divisée en deux sous-catégories : représentations de points saillants et représentations de frontières ou b-reps.

En revanche, les modèles solides représentent l'extérieur et l'intérieur de l'objet. Ils se divisent principalement en deux sous-catégories: les modèles basés sur la déformation d'un atlas et les représentations médianes. Cette section fait un résumé des représentations médianes car c'est la technique utilisée pour les développements de cette thèse. Cette approche offre aussi des avantages pour décrire l'intérieur d'un objet, ce qui n'est pas le cas de nombreuses autres méthodes. Le chapitre 2 donne une revue complète des techniques de représentations.

7.2.1 Représentations médiane

Pour une notion si simple comme l'emplacement d'un objet, la description par son contour ou périmètre est particulièrement pauvre.

– Harry Blum

Le concept de représentation médiane a commencé avec [Blum *et al.* (1967)]. Blum a remarqué que pour toute forme, il était possible de calculer son axe médian. En le faisant, les objets pouvaient être décrits depuis l'intérieur vers l'extérieur, contrairement aux techniques qui cherchent à modéliser l'extérieur de l'objet uniquement.

Pour expliquer ce concept Blum a utilisé une analogie de "champ en feu", où la formation de l'axe médian se fait en mettant le feu à la couche externe de l'objet. Le feu se propage uniformément vers l'intérieur de l'objet et lorsque les fronts se rencontrent, nous trouvons l'axe médian. Suite à ce concept, la définition d'un axe médian est:

Definition 8. *L'axe médian est la collection de points intérieurs équidistants avec au moins deux points sur la frontière de l'objet.*

Parallèlement au MA (axe médian) une MAT (transformation de l'axe médian) est générée:

Definition 9. *La transformation d'axe médian est la distance de chaque point de l'axe médian à la frontière la plus proche de l'objet.*

Dans le contexte de l'analogie "champ en feu", la MAT ajoute à chaque point de l'axe une valeur équivalente à la durée de combustion depuis la frontière jusqu'à ce que les deux fronts se rencontrent dans le MA. La MAT a été critiquée vu que des petites perturbations sur la frontière produisent des changements significatifs sur le MA, ce qui ne rend pas une description pratique de la forme d'un objet. Cette instabilité a fait l'objet de nombreuses recherches qui visaient à produire un meilleur calcul du MA. L'idée est d'identifier les sous-ensembles significatifs qui composent le MA en échangeant l'exactitude contre la stabilité.

En général, pour accroître la stabilité, un élagage du MA est fait par un seuil et un critère qui détermine la “substance” et la “connexion”. La substance étant la partie concrète de l’objet, et la connexion, comment les pièces sont reliées. Pour avoir une meilleure compréhension de cette notion on peut imaginer une main. Une main est composée par une paume (un bloc) et des doigts (des protubérances) ou considérez-la comme une collection d’objets connexes. La substance est connectée d’une telle manière que nous percevons une main. L’objectif est donc de trouver ces connexions.

Différents auteurs proposent des approches pour calculer un MA stable : voir les méthodes de [Culver *et al.* (1999)], [Amenta *et al.* (2001)], [Katz and Pizer (2003)], [Miklos *et al.* (2010)].

Un MA stable est un descripteur de forme puissant qui produit représentations compactes de la forme et de la surface d’un objet. Les concepts “point central” et positions à l’intérieur et par rapport à l’objet sont décrits plus efficacement à l’aide du MA.

En 2D, le MA est créé à partir des centres des cercles de rayon maximal ayant au moins deux points en commun avec la frontière de l’objet. L’union des centres de ces cercles forme le MA. En 3D le MA est composé des feuilles générées avec les centres des sphères de rayon maximum inscrites dans l’objet. De manière générale, le MA s’étend dans les dimensions supérieures, où il est défini à partir d’hypersurfaces générées avec les hypersphères de rayon maximum inscrites dans l’objet.

Une question importante liée aux représentations médianes est de savoir si les analyses statistiques sont viables sur une population d’objets. La principale difficulté consistera à produire la correspondance des structures. Pour utiliser une représentation médiale pour l’analyse statistique de la forme, la construction du MA s’effectuera d’une manière différente: le MA doit avoir une structure stable pour la population d’objets que nous voulons étudier.

Si nous prenons en considération comment le MA est construite, nous voyons que la procédure est une approche haut-bas. Elle commence à la frontière de l’objet et en utilisant la procédure pour inscrire des sphères, le MA est obtenu. La deuxième alternative consiste à construire le MA dans le sens inverse. [Styner and Gerig (2001)] propose une approche bas-haut pour construire le MA.

Pour résumer, la méthode de Styner calcule un MA moyen d’une population d’objets suivi d’un échantillonnage de la moyenne en utilisant une grille régulière des points. La grille de points est ajustée à la moyenne. Le résultat est utilisé comme le nouveau MA.

Pour calculer la moyenne du MA, une PDM (modèle de distribution de points) est créée à partir des représentations en SPHARM (harmoniques sphériques) des MA calculés pour chaque objet dans la population. Une PCA (analyse des composantes principales, voir Annexe A) est faite sur la PDM. Cette analyse permet de calculer une moyenne, dans ce cas un MA moyen. Enfin, la grille de points ou m-rep (définition donnée ci-après) est ajustée à la moyenne par la minimisation d’une fonction de distance sur les points. Une série de tests est exécutée pour évaluer si le m-rep représente correctement chaque objet, ainsi que la population en général.

Un m-rep est un objet continu qui définit le MA d’un objet comme un ensemble d’espaces topologiques [Pizer *et al.* (1999)], [Yushkevich *et al.* (2003)], [Pizer *et al.* (2003)]. La MS (feuille médiale en 3D, équivalent à MA en 2D) est paramétrée par $MS(u, v)$ où u et v peuvent prendre toutes valeurs comprises entre $[0, 1] \in R$. La MS est un ensemble continu C^2 d’atomes médians avec une surface implicite y_0 pour la surface supérieure et y_1 pour la surface inférieure.

$$MS(u, v) = \{x, r, n_0, n_1\} \quad (7.1)$$

L'équation 7.1 définit un atome pour chaque (u, v) sur la MS, x correspond à la position sur la MS, n_0 et n_1 sont des vecteurs et r est la longueur de ces deux vecteurs ($n_{0,1}$ sont des vecteurs normalisés).

Un autre type d'atome se trouve sur les bords de l'objet, nommé atome de crête. La crête est chargée de joindre les surfaces supérieures et inférieures pour produire un contour fermé.

Pour décrire un m-rep informatiquement, un ensemble discret d'atomes est utilisé. Par la suite, le mot m-rep fait référence à la version discrète de l'objet. Les m-reps utilisent les mécanismes d'interpolation décrits dans [Thall (2004)], pour reconstruire la surface de l'objet. La surface interpolée est en correspondance aux normales décrites par les vecteurs n_0 et n_1 . La surface est C^2 continue partout.

En résumé, les m-reps sont des structures qui décrivent efficacement la géométrie d'un objet d'une manière multi-échelle. Ils peuvent être utilisés pour la segmentation des images médicales [Pizer *et al.* (2005)] et pour effectuer des analyses statistiques sur la variabilité de forme [Fletcher *et al.* (2004)]. La méthode employée par m-reps pour produire des statistiques est appelée PGA (analyse des géodésiques principales) une généralisation de la PCA (analyse en composantes principales).

La PGA décrit les variations sur les espaces sphériques avec des grands cercles. Malheureusement, les données portées par un modèle m-rep sont décrites sur des petits cercles et la description de la variabilité avec une PGA n'est pas optimale. Une méthode plus appropriée peut être développée en prenant en compte cette information.

La section suivante fait un résumé des s-reps, la technique développée et utilisée tout au long de cette thèse.

7.2.2 Représentations quasi-médianes

Les représentations quasi-médianes [Pizer *et al.* (2012)] ou s-reps, diffèrent des représentations médiane dans le critère strictement médial imposé sur chaque atome. C'est-à-dire, la position d'un atome n'est pas nécessairement le centre d'une sphère maximal inscrite dans la forme. Dans un s-rep, les atomes situés au centre d'une sphère maximale sont favorisés dans le processus d'optimisation mais des petits écarts sont tolérés, ce qui signifie que les rayons (vecteurs vers la surface) peuvent avoir différentes longueurs; Cela se fait dans l'objectif d'améliorer l'ajustement du s-rep à un objet donné.

Les s-reps sont des objets continus, définies comme un locus (lieu central) de vecteurs (p, S) avec la queue situé à p et une direction qui pointe vers $p + S$. Ils sont paramétrés par (u, v) tels que la feuille squelettique ($SS = \text{Skeletal Sheet}$) est définie comme $SS = \{p(u, v) : \forall (u, v) [0, 1]\}$, les vecteurs $SP = \{S(u, v) : \forall (u, v) [0, 1]\}$ et la frontière de l'objet est $BO = \{p(u, v) + S(u, v) : \forall (u, v) [0, 1]\}$. L'union des queues des vecteur forme le locus squelettique comme un feuille entièrement plié, c'est-à-dire, la partie supérieure de la feuille est paramétrée par $v \in [0, 0.5]$ et la face inférieure par $v \in [0, 5; 1]$. Selon cette définition, tous les points à l'intérieur de l'objet sont accessibles par au moins un vecteur; il faut faire attention aux coins de l'objet car ils sont atteints par plusieurs vecteurs mais ils permettent à la SS de se plier et créer cette représentation d'objet avec une description interne.

Les longueurs des vecteurs sont définis comme $r(u, v) = |S(u, v)|$ et les directions des rayons comme $U(u, v) = S(u, v)/r(u, v)$.

La section 2.4.3 explique en détail les notions sur la description interne d'un objet et la génération des cartes $X2U$, qui permettent le passage d'une coordonnée physique à une coordonnées s-rep. Ces cartes seront utilisées dans la section 7.5 pour améliorer les

propriétés des s-reps avec de l'information volumétrique.

D'une façon similaire aux m-reps, les s-reps sont représentés avec un ensemble discret d'atomes. Par la suite, srep fait référence à la version discrète de l'objet. Les s-reps utilisent les mécanismes d'interpolation décrits dans [Damon (2003)], [Han *et al.* (2006)], [Damon (2008)]. Avec ces mécanismes d'interpolation, la surface de l'objet ainsi que tous les positions internes de l'objet peuvent être trouvées.

En plus de la modélisation de forme en utilisant les mécanismes d'interpolation, le but est de produire des s-reps utilisables pour des analyses statistiques. Pour calculer des statistiques sur un ensemble d'objets, la SS d'un srep doit rester stable dans chaque instance de la population d'objets.

Les résultats statistiques sont robustes quand les points saillants des objets sont en correspondance dans la population.

Tout d'abord, un srep est créé à partir d'une image binaire. Cela est obtenu par des méthodes de segmentation automatiques ou manuelles appliquées à des images médicales d'une certaine modalité.

Avec cette image binaire, une transformé de distance est calculé. La transformé de distance associe une valeur de distance à chaque point de l'image au point plus proche de la frontière de l'objet. Les points à l'intérieur de l'objet ont des valeurs négatives, les points à l'extérieur de l'objet ont des valeurs positives, et les points dans la frontière sont égaux à 0.

Un processus d'ajustement est utilisé pour aligner le srep à l'image binaire. Ce processus est guidée par le calcul des gradients dans la transformé de distance. L'ajustement a principalement 3 étapes: la première étape consiste à aligner le srep sur l'image ; la deuxièmement étape consiste à déplacer chaque atome séparément (le mouvement d'un atome modifie la surface) ; la troisième étape consiste à modifier les longueurs des vecteurs vers la surface.

Avec cette procédure, une figure squelettique de base peut être placée sur un ensemble d'images binaires. Le processus d'ajustement crée la meilleure représentation pour l'image binaire et augmente la correspondance des positions d'objet à travers la population.

L'ensemble des s-reps contient un squelette stable et modélise les objets dans la population, La méthode CPNS (composite principal nested spheres, voir annexe B) est utilisé pour le calcul de statistiques de forme.

CPNS produit une forme moyenne et un ensemble de modes propres. Toutes les formes dans la population peuvent être modélisées avec la forme moyenne, les modes propres et un ensemble de coefficients. En général, il est possible d'obtenir des statistiques robustes pour la forme des objets en 3D à l'aide des représentations médianes.

La section suivante fait un résumé pour expliquer la mise en œuvre de représentations médiales.

7.2.3 Modélisation d'objet avec s-reps

Interpolation de la feuille médiane

L'interpolation de la feuille médiane est faite avec splines cubiques d'Hermite. Pour produire l'interpolation, les dérivées partielles pour chaque atome sur la SS, et la normale doivent être définies.

Sois $s_{rep} = \{(p_i, S_i) : i \in N\}$ et $N = m \times n$, un srep est représenté par une grille discrète d'atomes. L'interpolation utilise les quatre points de contrôle dans chaque quadrangle de la grille.

Les équations 7.2 et 7.3 indiquent comment calculer la dérivée partielle pour un atome dans le sens de u et de v sur la SS. $\Delta u = 1/m$ et $\Delta v = 1/n$ correspondent à la longueur de déplacement. Δu est le déplacement le long de la direction u vers le prochain atome sur la grille des atomes discrets, de même pour la direction v .

$$\partial p(u, v)_u = \begin{cases} p(u + \Delta u, v) - p(u, v) & u = 0 \\ (p(u + \Delta u, v) - p(u - \Delta u, v))/2 & 0 < u < 1 \\ p(u, v) - p(u - \Delta u, v) & u = 1 \end{cases} \quad (7.2)$$

$$\partial p(u, v)_v = \begin{cases} p(u, v + \Delta v) - p(u, v) & v = 0 \\ (p(u, v + \Delta v) - p(u, v - \Delta v))/2 & 0 < v < 1 \\ p(u, v) - p(u, v - \Delta v) & v = 1 \end{cases} \quad (7.3)$$

L'équation 7.4 donne une approximation à la normale d'un atome à la SS. La normale est calculée à partir des vecteurs situés à la même position sur la SS mais directions opposées.

$$N(u, v) \approx \frac{S(u, v) - S(u, 1-v)}{\|S(u, v) - S(u, 1-v)\|} \quad u \in [0, 1], v \in [0, 0.5] \quad (7.4)$$

$$H_{control} = \begin{bmatrix} p_{11} & p_{12} & \partial p_{11}^T & \partial p_{12}^T \\ p_{21} & p_{22} & \partial p_{21}^T & \partial p_{22}^T \\ \partial p_{11}^T & \partial p_{12}^T & h_0 & h_0 \\ \partial p_{21}^T & \partial p_{22}^T & h_0 & h_0 \end{bmatrix} \quad (7.5)$$

Pour interpoler la SS, un matrice d'Hermite est défini dans l'équation 7.5, où $\partial p(u, v)^T = \partial p(u, v) - (\partial p(u, v) \cdot N(u, v))N(u, v)$ est la projection des dérivés discrets dans les directions u où v sur les plans de la tangente qui sont déterminés par les normales $N(u, v)$. L'interpolation de la SS dépend des normales et des dérivés discrets; h_0 est un vecteur rempli de 0.

$$\begin{aligned} H_1(s) &= 2s^3 - 3s^2 + 1 \\ H_2(s) &= -2s^3 + 3s^2 \\ H_3(s) &= s^3 - 2s^2 + s \\ H_4(s) &= s^3 - s^2 \end{aligned} \quad (7.6)$$

$$p(u, v) = \begin{bmatrix} H_1(\hat{u}) & H_2(\hat{u}) & H_3(\hat{u}) & H_4(\hat{u}) \end{bmatrix} H_{control} \begin{bmatrix} H_1(\hat{v}) \\ H_2(\hat{v}) \\ H_3(\hat{v}) \\ H_4(\hat{v}) \end{bmatrix} \quad (7.7)$$

La position interpolée d'un atome quelconque sur la SS est indiquée dans l'Équation 7.7, en utilisant un patch de contrôle de matrice de Hermite et les fonctions de poids définies dans l'Équation 7.6. $\hat{u} = (u - floor(u))/\Delta u$, où $floor(u)$ retourne la coordonnée u de l'atome à p_{11} , de même pour \hat{v} .

De manière similaire, l'interpolation des vecteurs peut être faite à l'aide de fonctions d'Hermite. Au lieu d'utiliser les points de contrôle $p(u, v)$, les vecteurs $S(u, v)$ sont utilisés. En conséquence, les dérivés discrètes sont calculées pour chaque vecteur, aucune projection n'est faite en utilisant les normales à la SS ; l'interpolation des vecteurs ne dépend que des dérivés discrètes.

La surface supérieure et inférieure peut être générée à l'aide des mécanismes décrits ci-dessus. Les surfaces supérieures et inférieures se rencontrent à la crête de l'objet. La section suivant explique comment effectuer l'interpolation de la crête pour produire la surface complète de l'objet.

Interpolation de crête

Pour interpoler la crête, nous voulons créer une surface qui ne s'effondre pas vers l'intérieur de l'objet, *i.e.*, sa section doit être convexe dans la direction principale et préserver la continuité C^2 . La surface doit aussi correspondre aux dérivés partiels afin de produire une surface lisse.

La méthode d'interpolation de crête est expliquée en montrant comment interpoler les longueurs r entre deux vecteurs selon un angle θ . La fonction $r(\theta)$ renvoie la longueur à un angle donné. De façon similaire, nous voulons interpoler la section transversale de la crête avec l'angle θ qui paramètre le parcours du vecteur qui pointe vers la surface supérieure jusqu'au vecteur qui pointe vers la surface inférieure.

La même problématique peut être étendue à trois dimensions où l'interpolation produit une courbe dans l'espace. Afin de produire une surface interpolée, la section transversale se déplace le long de la crête où se situe le bord de la SS.

$$\frac{\partial^2 r(\theta)}{\partial \theta} = q_0 + q_1 \theta + q_2 \theta^2 \quad (7.8)$$

La première étape consiste à définir une fonction quadratique de la courbure, comme montré dans l'équation 7.8, nous voulons avoir une courbe convexe interpolée. En intégrant cette équation deux fois, nous trouvons la fonction qui donne la longueur pour $\theta \in [0, \theta_{max}]$.

$$\frac{\partial r(\theta)}{\partial \theta} = \int_0^{\theta_{max}} \frac{\partial^2 r(\theta)}{\partial \theta} \partial \theta \quad (7.9)$$

$$\frac{\partial r(\theta)}{\partial \theta} = \frac{\partial r_0}{\partial \theta} + q_0 \theta + \frac{1}{2} q_1 \theta^2 + \frac{1}{3} q_2 \theta^3 \quad (7.10)$$

$$r(\theta) = \int_0^{\theta_{max}} \frac{\partial r(\theta)}{\partial \theta} \partial \theta \quad (7.11)$$

$$r(\theta) = r_0 + \frac{\partial r_0}{\partial \theta} \theta + \frac{1}{2} q_0 \theta^2 + \frac{1}{6} q_1 \theta^3 + \frac{1}{12} q_2 \theta^4 \quad (7.12)$$

Nous allons commencer par résoudre les coefficients de q_1 et q_2 , en utilisant le système d'équations $r(\theta)$, $\partial r(\theta)/\partial \theta$ et $\partial^2 r(\theta)/\partial \theta$, comme indiqué dans l'équation 7.14.

$$q_2 = \frac{6}{\theta_{max}^4} (2\partial r_{end} \theta_{max} + q_0 \theta_{max}^2 - 6r_{end} + 6r_0 + 4\partial r_0 \theta_{max}) \quad (7.13)$$

$$q_1 = \frac{-6}{\theta_{max}^3} (-\partial r_{end} + r_0 + \partial r_0 \theta_{max} + \frac{q_0}{2} \theta_{max} + \frac{q_2}{12} \theta_{max}^4) \quad (7.14)$$

Il existe une solution au problème pour chaque q_0 , mais la solution optimale se trouve lorsque q_0 minimise tel qu'indiqué dans l'équation 7.16.

$$\partial r_{end} = -1\partial r_{end} = 0\partial r_{end} = 1r_0\theta\partial r_0 \quad (7.15)$$

$$\hat{q}_0 = \arg \min_{q_0} \sum_{\theta=0}^{\theta_{max}} \frac{\partial^2 r(\theta)}{\partial \theta} \quad (7.16)$$

Pour produire un courbe dans l'espace, la méthode est appliquée séparément aux coordonnées $[x, y, z]$. En utilisant l'information discrète donnée par le s-rep, il est possible de récupérer les positions p_0 , p_{fin} et calculer les dérivées discrètes ∂p_0 et ∂p_{fin} qui sont

les paramètres nécessaires pour l'ajustement de la courbe. Les atomes de crête du s-rep forment une boucle autour de l'objet où les positions de crête sont données par cp_n et n est le nombre de positions de crête. Les dérivées directionnelles sont calculées comme $\partial cp_j = (cp_{j+1} - cp_{j-1})/2$ qui sont projetés sur le plan tangent, donné par les normales de la SS à chaque atome $\partial \hat{cp}_j = \partial cp_j - (\partial cp_j \cdot N_{cp_j})N_{cp_j}$.

Le même mécanisme d'interpolation est utilisé pour les vecteurs en haut, crête et en bas, par conséquence, pour un t donnée, il est possible de trouver le vecteur de haut $CS(t)^1$, le vecteur de crête $CS(t)^0$ et le vecteur de bas $CS(t)^{-1}$; plus la position sur la crête de l'objet.

Enfin l'interpolation est faite pour cet ensemble de vecteurs, ce qui permet de produire la surface de crête interpolée de haut vers le bas.

La section suivante expose la représentation des coordonnées internes d'un s-rep afin de permettre l'inclusion des propriétés internes volumiques.

Coordonnées internes d'un s-rep

Les coordonnées internes d'un objet sont décrits par des cartes $X2U$. Ces cartes permettent la requête des coordonnées spatiales $[x, y, z]$ et retourne des coordonnées relative à l'objet $[u, v, \tau]$. Les cartes $X2U$ serviront dans la section 7.5 pour mapper les solides générés avec la méthode décrit dans la section 7.4. Cela est possible parce que les solides sont synthétisés dans un cube. Chaque point dans le cube peut être lié à $[u, v, \tau]$, fourni ainsi, un mécanisme pour mapper un solide dans un s-rep.

Pour créer une carte $X2U$, chaque vecteur dans la SS (la feuille squelettique) du s-rep est représenté par une coordonnée $[u, v]$. τ est utilisé pour représenter la longueur du vecteur jusqu'à la surface.

Grâce aux mécanismes d'interpolation de la SS et des vecteurs (haut, bas et crête), la fonction $U2X(u, v, \tau) = [x, y, z]|(u, v, \tau) \in [0, 1])$ donne la position en coordonnées physiques $[x, y, z]$ correspondant aux coordonnées $[u, v, \tau]$ de l'objet. $v \in [0, 0.5]$ fait référence aux vecteurs dans la face supérieure et $v \in [0, 5; 1]$ fait référence aux vecteurs dans la face inférieure du s-rep par rapport à la SS.

En utilisant la fonction $U2X$, la carte $X2U$ de l'objet est créée. Avec une carte $X2U$, l'accès aux coordonnées d'objet est fait avec une complexité de $O(1)$.

7.2.4 Conclusions

Les s-reps sont capables de modéliser l'espace continu dans un objet. Il est donc possible d'inclure de l'information volumique à la représentation géométrique. On pourrait envisager des représentations multi-échelle de cette information. Cette caractéristique est utilisée pour inclure les paramètres nécessaires pour effectuer une simulation d'IRM.

En plus des possibilités de description interne d'un objet, les s-reps sont adaptés pour le calcul de la variabilité statistique de forme sur une population d'objets modélisée avec la même SS. Ce calcul de variabilité statistique est fait avec CPNS. Par conséquent, tous les objets dans la population peuvent être décrits avec quelques coefficients, et la forme moyenne et les modes propres obtenus avec l'analyse via CPNS.

La section suivante explique une nouvelle méthodologie pour modéliser le cortex du cerveau avec s-reps. Avec cette structure une analyse statistique est menée à l'aide du CPNS, ce qui prouve que les s-reps sont bien adaptées pour modéliser des structures complexes.

7.3 Modélisation du cortex par de s-reps

7.3.1 Introduction

Le cortex cérébral à la forme d'une feuille pliée de tissu neuronal avec des interconnexions compactes qui permettent le traitement de l'information par le cerveau. Il joue un rôle important dans la mémoire, l'attention, la perception, la pensée, le langage et la conscience. Des avancées ont été réalisées pour comprendre la structure et la fonction du cortex. [Lorente de Nò (1934)] suggère que le cortex est formé par des petits cylindres qui contiennent des chaînes verticales des neurones ; Ces structures ont été appelées colonnes, et correspondent aux groupes de cellules perpendiculaires à la surface corticale. Cette hypothèse a été confirmée dans les études physiologiques faites par [Mountcastle (1998)].

Le cortex est une feuille stratifiée avec une structure cellulaire plus ou moins uniforme. Aujourd'hui, l'organisation en colonne est le modèle établi pour expliquer le traitement de l'information dans le cortex.

Presque deux tiers de la surface corticale est caché dans les sillons. Il est difficile d'effectuer des analyses statistiques et la visualisation du cortex. Différentes procédures ont été élaborées pour déplier et mapper la surface corticale sur différents espaces (gonflés, sphériques ou aplatis) [Drury *et al.* (1996)], [Hermosillo *et al.* (1999)], [Fischl *et al.* (1999)], [Pons *et al.* (2004)]. Cela permet à la surface corticale d'être analysée et visualisée. Des méthodes statistiques peuvent aussi être appliquées sur ces espaces. *Freesurfer* (un outil automatisé pour la reconstruction de la surface corticale du cerveau à l'aide des données d'IRM structurelles) utilise la procédure de gonflement et d'aplatissement de [Fischl *et al.* (1999)].

De la même façon, l'évolution du cortex a été un sujet de grand intérêt. Une grande partie des efforts a aidé à comprendre comment le processus de pliage se produit. Les pliages sont uniques à chaque cerveau et un repliement anormal est lié aux problèmes neurologiques comme la schizophrénie, l'épilepsie, l'autisme et le syndrome de Down. Pour une revue récente sur les théories de pliage voir [Filas *et al.* (2013)].

Il y a de nombreuses possibilités ouvertes de recherche dans le développement des modèles du cortex. Comme indiqué par Javier de Felipe [Defelipe *et al.* (2012)], “il est encore nécessaire d'atteindre une meilleure compréhension fondamentale sur les colonnes corticales et comment elles sont utilisées dans les processus du cortex. En conséquence, il est important de traduire ces dernières avancées techniques et découvertes en neurosciences en applications pratiques pour les neuroscientifiques, les cliniciens et pour ceux qui s'intéressent à l'anatomie comparative et évolutive du cerveau”.

Compte tenu de ces faits, l'un des objectifs de cette thèse est de fournir un outil qui modélise la forme du cortex et se rapporte à la structure physique réelle. La section 7.2.3 définit un srep avec les mécanismes d'interpolation correspondants pour paramétriser l'intérieur de l'objet en $[u, v, \tau]$. Les s-reps peuvent être utilisés pour modéliser les informations anatomiques et physiologiques des différentes couches du cortex. Cette information peut être incluse naturellement à l'aide de la coordonnée τ .

En plus de fournir une description de forme, les s-reps ont été utilisés avec succès pour le calcul statistique sur la forme et le calcul de la forme moyenne sur une population d'objets. Avec cette description statistique, il semble possible de classifier des objets selon sa forme. Les objets modélisés avec s-reps jusqu'à présent sont simples. La plupart d'entre eux ont une forme de type arrondi ou allongé comme celle de l'hippocampe [Pizer *et al.* (2012)].

Il est démontré que les s-reps sont capables de représenter une structure pliée et complexe comme le cortex. La feuille de l'objet ne crée pas de branches et capture la majorité des plis du cortex. Avec cette structure, une analyse statistique de la variabilité de la

forme est faite sur le cortex.

La section suivante fait un résumé qui explique comment créer un s-rep du cortex. La procédure utilise une représentation sphérique du cortex [Fischl *et al.* (1999)] où la surface de la matière blanche (WM) et la surface de la matière gris sont liées à une sphère. Le pliage du s-rep dans le cortex est fait avec la projection de la SS (feuille squelettique du s-rep) dans une sphère et l'ajustement de cette SS à la représentation sphérique du cortex. Grâce à la relation entre la sphère et les surface corticales, le s-rep est plié à l'intérieur du cortex. Avec la figure squelettique à l'intérieur du cortex, les méthodes d'interpolation indiquées dans la section précédente peuvent reconstruire la surface de la GM et la surface de la WM. La section 3.3 évalue la qualité des surfaces interpolées. La section 3.4 à l'aide du CPNS (décrit dans l'annexe B), fait une analyse statistique sur une population d'objets.

7.3.2 La véritable forme du cortex

Le cortex est une feuille très pliée. Son épaisseur varie à travers des régions corticales. Malheureusement, le cortex est souvent représenté à l'aide de surfaces et il est difficile de représenter les caractéristiques internes. Pour reconnaître la vraie forme du cortex qui ressemble à une crêpe pliée, Nous proposons une procédure pour créer un s-rep du cortex.

La procédure comprend cinq étapes :

- (a) Une cartographie du cortex sur une sphère s'effectue à l'aide de la méthode de [Fischl *et al.* (1999)]. Cette sphère est tournée vers le Nord en utilisant le corps calleux.
- (b) La grille régulière ou la SS d'une s-rep de base est transformée en une « grille circulaire logarithmique ».
- (c) La « grille circulaire logarithmique » est transformée en une sphère (avec un trou au pôle Nord).
- (d) La SS sur la sphère est ajustée à la cartographie du cortex sur la sphère.
- (e) La SS est repliée dans la forme du cortex. Au cours de la procédure de pliage, l'épaisseur du cortex (longueur de chaque vecteur du s-rep) est déterminée.

Les détails de chaque étape sont décrites dans la section 3.2.

Une fois le s-rep du cortex est créée, les surfaces corticales peuvent être reconstruites à l'aide des mécanismes d'interpolation. La qualité des surfaces est évaluée dans la section 3.3.

La section 3.4 utilise CPNS sur le s-rep du cortex et vise à déterminer si une variation d'épaisseur corticale peut être détectée. Un cas de test est fait à l'aide d'une s-rep de base et 60 modèles dérivés de celle-la. L'épaisseur corticale est réduite dans certaines régions du cortex. L'ensemble de données est créé en ajoutant un peu de bruit gaussien à la position du modèle et à chaque direction des vecteurs du s-rep. Chaque échantillon va être modifié avec une variation linéaire de l'épaisseur corticale, plus précisément sur la région frontale supérieure et la région temporelle supérieure du cortex. Si CPNS produit des modes de variation, le premier mode devrait être lié à la réduction de l'épaisseur corticale.

Comme prévu, après l'analyse statistique il est déterminé que le premier mode propre correspond à la variation de l'épaisseur corticale. D'une façon similaire à PCA, une modèle du cortex dans la population peut être modélisée avec une liste des coefficients b_n et les vecteurs propres P_n produit par CPNS.

Le modèle du cortex est déformé uniquement dans le premier mode de variation avec

$$b_n = \begin{cases} c \in [-1.5, 1.5], & n = 1 \\ 0, & otherwise \end{cases} \quad (7.17)$$

Quand ce nouveau modèle est comparé contre le modèle de base, on retrouve des variations dans la zone supérieure frontale et temporale supérieure du cortex.

La section suivante fait un résumé sur la représentation du cortex avec s-reps et les résultats obtenus.

7.3.3 Conclusions

L'apport principal de ce travail est de représenter le cortex par la méthode de s-reps comme une feuille épaisse et pliée. Les s-reps ont des caractéristiques qui permettent d'inclure de l'information à une échelle donnée, de fournir une nouvelle façon d'analyser les colonnes corticales et d'analyser les lésions corticales dans un espace topologique différent. Ceci est permis par le système de coordonnées volumique $[u, v, \tau]$ porté par les s-reps.

Une deuxième contribution consiste à fournir une représentation compacte du cortex à l'aide de la méthode CPNS. Cette description statistique modélise les variations d'épaisseur corticale avec une forme moyenne, certains modes propres et quelques coefficients. CPNS est capable de détecter des variations d'épaisseur localisée dans les régions du cortex supérieur-frontale et supérieur-temporale. Ceci suggère que l'approche peut produire des statistiques pour les cas cliniques longitudinal (même patient, plusieurs acquisitions dans le temps) caractérisées par les variations d'épaisseur corticale [Kaplan *et al.* (2009)]. D'autres cas cliniques tels que la psychose, la schizophrénie, l'hyperactivité chez les enfants et l'autisme présentent des variations anormales de l'épaisseur corticale.

Il a été prouvé que les s-reps sont adaptés à la modélisation de formes complexe comme celle du cortex et de fournir un nouveau moyen d'analyse.

Le travail présenté montre que la méthode CPNS peut détecter un amincissement cortical sur un ensemble de modèle srep du cortex.

La section suivant décrit une technique de synthèse de texture permettant de créer des représentations volumique à partir d'échantillons d'images 2D. Les texture 3D peuvent être utilisés avec les s-reps pour créer des modèles volumiques.

7.4 Synthèse de texture pour la représentation d'objets en 3D

7.4.1 Introduction

L'objectif est de produire des volumes de paramètres physiques. Ces volumes peuvent être placés à l'intérieur d'un srep pour représenter ses propriétés physiques. Avec un simulateur d'image et une description des objets, des images simulées peuvent être générées. Pour comprendre la méthode de synthèse de la texture 3D, il est nécessaire de comprendre les propriétés de texture que l'on cherche à modéliser.

Les objets dans le monde réel ont un grand nombre de propriétés visuelles. Parmi ces propriétés il y a la luminance, la couleur et les caractéristiques de surface comme la reflectivité et la rugosité. Les variations spatiales plus ou moins rapides et régulières de ces caractéristiques produisent des images dites texturées.

Le système visuel humaine a la capacité de distinguer les régions texturées. Ce phénomène est connu comme la ségrégation de texture ; Il nous permet de distinguer une grande variété d'objets et matériaux avec peu d'effort.

On peut distinguer des régions texturées même s'il n'y a aucune frontière visible dans l'image. Ce type d'observations ont conduit à la *conjecture de Julesz*, une hypothèse qui cherche à déterminer si la perception humaine de textures est sensible aux différences dans les statistiques de première et de seconde ordre. Julesz a conclut que des images avec des statistiques identiques jusqu'au troisième ordre pouvaient être distinguées par notre système visuel [Julész *et al.* (1978)].

Cependant des contre-exemples à la conjecture de Julesz ont conduit à utiliser essentiellement les statistiques du premier et deuxième ordre dans les méthodes d'analyse et de synthèse de texture.

Definition 10. *Les textons sont des microstructures fondamentales dans les images naturelles et ils sont les éléments de base dans la perception visuelle (pré-attentive).*

L'analyse de texture par les textons a permis de réduire l'information redondante et de produire des représentations compactes de texture plus facile à manipuler. Cette technique a été appliquée dans une grande variété de domaines qui incluent la segmentation et la reconnaissance d'objets [Leung and Malik (2001)], l'édition d'image et de vidéo, la fusion et la complétion [Wexler *et al.* (2004)]. Elle a fourni des éléments pour aider à comprendre la fonction des neurones dans les systèmes biologiques de vision. Elle a permis des progrès dans la neurophysiologie de la perception de texture [Olshausen and Field (1997)], [Landy and Graham (2004)].

En informatique, appliquer des textures aux modèles géométriques est la clé pour améliorer la représentation d'objets en 3D. Les objets texturés deviennent plus réalistes et ils sont plus agréables pour notre système visuel.

Pour appliquer une texture à un objet 3D, la première étape est d'acquérir des échantillons suffisamment larges pour couvrir toute la surface de l'objet. Pour atteindre cet objectif, il faut des méthodes capables de synthétiser une texture sur des grands surfaces.

Une texture peut être modélisée par un mélange d'approche stochastique et d'approche structurelle. Les textures naturelles se trouvent quelque part entre les deux car elles contiennent des aspects stochastiques et réguliers. Les textures structurelles ont des motifs réguliers quasi périodique comme un sol pavé. Les textures stochastiques n'ont pas une structure régulière identifiable. Il y a deux approches pour synthétiser une texture, les méthodes procédurales et les méthodes basées sur un motif de base.

Les approches procédurales cherchent à modéliser la texture à l'aide de fonctions de bruit. Ces méthodes exploitent les caractéristiques stochastiques des textures. Il est possible d'atteindre une grande variété de résultats par la "structuration" du bruit.

Les approches basées sur de motifs dépendent de l'hypothèse de localité et de stationnarité de la texture. Supposons que nous pouvons analyser une image texturée avec une petite fenêtre de taille fixe. La localité signifie qu'un nouveau pixel peut être prédit à partir des informations sur une seule fenêtre spatiale et la stationnarité de texture signifie que les statistiques spatiales de la texture sont invariantes sur plusieurs fenêtres. Ce type de méthodes possède de nombreuses propriétés souhaitables. Il suggère qu'un petit échantillon de texture peut être utilisé pour reproduire les caractéristiques stochastiques et structurelles sur une image plus grande. L'inconvénient est le temps de synthèse du résultat.

Le premier défi d'une approche stochastique consiste à préserver l'aspect initial du motif. Cela peut être fait en reproduisant les caractéristiques de la texture à des endroits

aléatoires dans une image et les discontinuités non réalistes. Un deuxième défi consiste à synthétiser la texture sur une surface à l'aide des propriétés comme l'orientation ou l'échelle.

Dans cette thèse, une approche stochastique pour synthétiser des textures volumiques est utilisée. Les textures 3D portent l'information volumique et modélisent les propriétés internes d'un objet. Elles peuvent être utilisées pour effectuer des simulations de dispersion, améliorer le rendu volumique d'un objet ou révéler des caractéristiques internes. La méthode de synthèse utilise des échantillons d'images 2D texturées et produit un texture 3D avec les mêmes caractéristiques.

Les textures 3D seront utilisées sur des modèles d'organes pour générer la géométrie et la distribution des paramètres nécessaires pour la simulation d'IRM. Ces paramètres sont obtenus à l'aide de la relaxométrie, une technique qui mesure les propriétés physiques et chimiques des matériaux. En plus de générer des distributions des paramètres physiques, la méthode de synthèse peut être utilisée pour améliorer les propriétés visuelles des objets.

Quelques textures sont générées pour certaines structures du cerveau. Elles contiennent les paramètres physiques correspondants à chaque tissu acquis dans les images de relaxométrie. Les textures ont quatre canaux : T_1 , T_2 , T_2^* et $M0$ (deux constantes de relaxation, l'inhomogénéité du champ local et la densité des protons). Les textures générées sont appliquées sur les modèles de structures cérébrales. Ces modèles seront utilisés pour simuler une image d'IRM, comme expliquée dans la section 7.5.

La section suivante explique la technique de synthèse de texture utilisée dans cette thèse.

7.4.2 Synthèse de texture solide basé sur optimisation

La synthèse de texture par optimisation a été proposée par [Kwatra *et al.* (2005)]. La méthode par optimisation est basée sur le modèle MRF (Markov Random Field). Si la localité et la stationnarité sont satisfaites, une mesure globale d'énergie peut être conçue en comparant les voisinages de la texture d'entrée et de sortie. L'énergie est définie à partir de la distance des voisinages dans le volume 3D aux voisinages les plus proches dans le motif de base.

La somme sur tous les voisinages définit l'énergie totale de la texture de sortie. La solution de la procédure de synthèse est trouvée quand l'énergie est minimale.

La synthèse de texture par optimisation est très flexible. Elle a l'avantage de créer des modèles à l'aide d'un ou plusieurs échantillons, car un échantillon différent peut être utile pour contraindre la vue perpendiculaire à un axe ($[x, y, z]$). L'approche peut utiliser des textures multicanal comme RVB (rouge, vert et bleu) et de cartes de distance pour coder les régions non structurées [Lefebvre and Hoppe (2006)].

L'approche est définie par l'équation suivante :

$$E(o, \{e\}) = \sum_t \sum_{i \in \{x, y, z\}} \sum_{u \in N_i(t)} w_{t,i} (o_{t,i,u} - e_{t,i,u})^2 \quad (7.18)$$

$$w_{t,i} = ||o_{t,i} - e_{t,i}||^{-1.2} \quad (7.19)$$

La mesure de distance compare les voisinages x y et z d'un texel t dans l'objet o contre les voisinages de l'échantillon de texture e . Quand cette distance est minimisée à l'aide d'une méthode de moindres carrés pondérés itératifs (IRLS), le résultat est une augmentation de la similitude entre l'échantillon et l'objet synthétique.

La procédure commence avec une résolution grossière et assigne des valeurs aléatoires de l'échantillon à l'objet synthétique. Ensuite, il alterne entre une phase de recherche où les

voisinages plus proches sont trouvés et une phase d'optimisation où la moyenne pondérée de chaque texel est calculée. Lorsque l'optimisation converge, il passe à un niveau de résolution plus fin à l'aide d'une interpolation linéaire.

Pour les détails d'implémentation voir la section 4.3. La qualité des textures est évaluée dans la section 4.3. La section suivante donne une conclusion de l'approche.

7.4.3 Conclusion

La méthode de synthèse permet de créer des tissus organiques réalistes à partir des petits échantillons acquis par un microscope ou d'autres sources d'acquisition comme l'imagerie SR μ CT, μ MR ou relaxométrie. La qualité des textures est démontrée quantitativement du point de vue statistique et morphologique.

Le chapitre suivant explique la simulation d'IRM. Les textures solides sont mises à l'intérieur des s-reps (voir section 2.3) pour représenter leurs propriétés physiques. En utilisant les échantillons texturés, des textures 3D sont synthétisées et appliqués aux différentes s-reps. Les nouvelles représentations sont utilisées pour créer une IRM simulée.

7.5 Simulation d'IRM du cerveau à l'aide des s-reps texturés

7.5.1 Introduction

L'imagerie médicale consiste à acquérir des détails de l'intérieur du corps humain avec différentes techniques. Parmi ces techniques on retrouve l'imagerie par résonance magnétique (IRM), tomodensitométrie (CT), ultrason (US) et tomographie par émission de positons (TEP). L'information acquise avec ces techniques est largement utilisée dans le domaine médical pour diagnostiquer et planifier les traitements des patients.

Chaque technique est complexe et possède des appareils d'imagerie coûteux. Ils nécessitent un entretien régulier et ils sont utilisés uniquement par du personnel spécialisé. Afin de calibrer un appareil pour un type spécifique d'acquisition, il y a un grand nombre de paramètres qui doivent être définis.

Selon les organes dans le corps humain à observer, la variation des paramètres produira plus ou moins de contraste entre les tissus du corps humain. Pour acquérir des détails dans l'image pour certains organes ou régions, il faut comprendre l'effet de chaque paramètre sur l'acquisition.

L'utilisation des patients humains pour optimiser un dispositif d'imagerie n'est pas possible car la disposition des tissus et des organes n'est pas connu. Les fantômes physiques ne sont pas pratiques car ils ne peuvent pas reproduire les conditions in-vivo.

La simulation d'image peut être utilisée pour résoudre cette problématique. Elle peut être utilisée pour optimiser un ensemble de paramètres d'acquisition d'image, ou pour produire des ensembles de données à faible coût pour une modalité d'image.

Il y a deux approches de base pour la simulation d'image. La première consiste à appliquer un modèle physique du processus d'acquisition sur un modèle numérique d'organe [Charpigny *et al.* (2009)]. Cette technique a un avantage car le modèle numérique peut être utilisé pour valider et améliorer les algorithmes de segmentation ou de quantification. La deuxième approche est liée à la synthèse de texture. La synthèse de texture est, par exemple, utile pour imiter les mammographies [Castella *et al.* (2008)] et peut-être d'autres types de modalités d'imagerie.

Dans ce mémoire de thèse, le premier type d'approche est utilisé pour simuler des images médicales. Il y a deux composants nécessaires pour créer une image simulée: un modèle d'objet (géométrie d'objet et distribution des paramètres physiques) et un simulateur d'image.

Les modèles d'objets contiennent de l'information sur l'anatomie, la physiologie et la pathologie. Ils peuvent être dynamiques et ils doivent être paramétrés selon la modalité de l'image que nous voulons obtenir.

Afin de produire des images simulées réalistes, l'objet virtuel doit être proche de l'objet du monde réel. Quelques tentatives ont été faites pour produire des images simulées à l'aide de modèles déformables [Segars *et al.* (2008)], [Le Maitre *et al.* (2009)], [Tobon-Gomez *et al.* (2011)]. La difficulté dans l'utilisation d'un modèle déformable est d'estimer la distribution des paramètres physiques à l'intérieur de l'objet. Une deuxième difficulté est liée à la modélisation de la forme de la morphologie humaine. Comme expliqué dans le chapitre 2, il n'y a pas une méthodologie bien établie pour modéliser la forme, ou pour calculer des statistiques qui tiennent compte de la variabilité de forme dans l'ensemble d'une population d'objets.

Dans cette thèse, une simulation d'IRM du cerveau est faite. Le modèle déformable expliqué dans la section 2.3.3 basé sur la méthode s-rep est utilisé pour modéliser les structures cérébrales suivantes: l'amygdale, le noyau caudé, l'hippocampe, les ventricules latéraux, le pallidum, le putamen et le cortex (voir chapitre 3 pour la méthode de création d'un s-rep du cortex). L'algorithme de synthèse de texture développé dans le chapitre 4 est utilisé pour générer de nouvelles distributions des paramètres physiques pour les structures cérébrales. Chaque modèle s-rep est texturé avec les paramètres physiques correspondants. Une image texturée contenant les structures est générée et utilisée comme entrée du simulateur. Le résultat est une image IRM simulée à partir des s-reps.

La section 5.4 évalue les images simulées en exécutant le pipeline de segmentation de *Freesurfer* (un outil automatisé pour la reconstruction de surface corticale du cerveau à l'aide de données de l'IRM structurelles).

La section suivante fait un résumé du processus de simulation.

7.5.2 Simulation d'IRM avec s-reps texturés

Le simulateur utilisé (*SimuBloch*) utilise les paramètres physiques des matériaux pour produire des images simulées. Chaque paramètre est fourni à *SimuBloch* à l'aide des images 3D. Chaque voxel contient les paramètres physiques nécessaires pour calculer le spin local de magnétisation.

En utilisant les paramètres physiques, le simulateur est en mesure de calculer divers types d'acquisitions dont *T1*-pondéré, *T2*-pondéré, *PD*-pondéré, FLAIR, etc. similaires aux séquences existantes dans un appareil réel.

SimuBloch est accessible sur la plate-forme *VIP*¹.

L'algorithme de synthèse de texture développé dans la section 4.4 est capable de préserver la structure et les caractéristiques statistiques d'un échantillon d'image 2D (cela est démontré dans la section 4.5). Les textures solides peuvent être appliquées aux s-reps en utilisant les coordonnées d'objet (voir section 2.4.3 pour les coordonnées d'objet). La section 5.3.1 explique en détail comment appliquer ou déformer une texture à un s-rep. La section 5.3.2 explique le procès pour obtenir des échantillons de texture des paramètres physiques et montre un ensemble de structures cérébrales texturées. La section 5.4 montre l'évaluation des images simulées en utilisant des algorithmes de segmentation connu.

¹<http://vip.creatis.insa-lyon.fr/>

La section suivante donne une conclusion de l'approche de simulation.

7.5.3 Conclusion

La capacité de l'algorithme de synthèse de texture n'est pas utilisée entièrement. Les échantillons d'image utilisés pour créer les données simulées ne contiennent pas d'information structurelle. Ce type d'information peut être conservé par l'approche de synthèse de texture. L'extraction de texture à partir des images des paramètres physiques a été une tâche difficile en raison de la résolution d'image. [Charpigny *et al.* (2009)] utilise une moyenne et un écart-type pour générer la distribution de paramètres physiques. Dans cette logique, les échantillons d'image des paramètres physiques ont été créés en choisissant des voxels dans les structures cérébrales. Les échantillons sont représentatifs de chaque tissu mais ils ne contiennent aucune information structurelle. Les résultats montrent que les images simulées ont été correctement segmentées par *Freesurfer* car les surfaces corticales sont bien reconstruites. Globalement, les surfaces corticales sont similaires aux données réelles mais quelques différences locales peuvent être détectées entre les images.

Le travail futur vise à améliorer les échantillons d'image des paramètres physiques. Ces images doivent avoir la texture correspondant à la structure du cerveau.

Un deuxième objectif vise à générer une description statistique de forme pour les structures sous-corticales et le cortex à l'aide des s-reps et CPNS. Les descriptions statistiques vont permettre modéliser des variations sur les sujets sains et pathologiques pour les structures sous-corticales et le cortex.

Avec les descriptions statistiques de forme et de texture, l'objectif est de produire des nouvelles images sans avoir besoin des acquisitions pour évaluer les paramètres physiques et la géométrie d'objet. Les structures de l'image simulée pourront avoir la forme caractéristique de pathologies décrites par les statistiques.

7.6 Conclusions et perspectives

7.6.1 Conclusions

L'objectif principal de cette thèse était de proposer une technique capable de modéliser les caractéristiques structurelles internes et externes des organes.

Après avoir examiné les techniques existantes pour modéliser la forme, on peut conclure que les s-reps fournissent des fonctionnalités supérieures à d'autres techniques. Une caractéristique très importante est la possibilité de décrire facilement l'intérieur d'un objet en cohérence avec la forme. Cela permet d'inclure des informations provenant de différentes échelles spatiales ou sources telles que des images d'histologie et/ou des paramètres physiques.

Pour prouver les capacités des s-reps, le cerveau humain a été choisi comme organe à modéliser. Il en ressort la contribution la plus importante de cette thèse, qui est la procédure pour modéliser le cortex cérébral avec un s-rep.

Le cortex cérébral n'a jamais été modélisé avec des techniques décrivant les caractéristiques internes. Maintenant, un seul objet non ramifié peut être utilisé pour décrire les deux surfaces corticales plus l'intérieur du cortex. La méthode s-rep fournit de nouvelles façons d'analyser les colonnes corticales et d'analyser les lésions corticales dans un espace paramétrique différent.

En plus de décrire la forme du cortex, il a été prouvé qu'une population de cortex peut être décrite par une forme moyenne, un ensemble de modes propres et quelque coefficient.

La méthode CPNS (composite principal nested spheres, voir annexe B) et la représentation du cortex a permis la création d'une représentation compacte avec une description statistique d'épaisseur dans le cortex.

Le deuxième contribution de cette thèse est de fournir une méthode pour modéliser les propriétés volumétriques d'un objet par une méthode de synthèse des textures 3D. Cette technique est compatible avec s-reps et permet de décrire l'intérieur d'un objet à l'aide de paramètres provenant de diverses sources.

Une simulation d'IRM du cerveau a été faite en utilisant les techniques décrites. Les s-reps ont été utilisés pour la modélisation des structures sous-corticales mises en correspondance avec des IRM segmentés avec *Freesurfer*. Les structures sous-corticales incluent : l'hippocampe, les ventricules latéraux, le pallidum, l'amygdale, le noyau caudé et le putamen.

Les propriétés internes des objets ont été modélisé avec des textures basées sur des paramètres physiques. Les structures sous-corticales et le cortex ont été fusionnées dans une image 3D contenant l'information des paramètres physiques. Cette image est fourni à un simulateur (*SimuBloch*) et le résultat est des images simulées d'IRM. Ces images ont été correctement segmentés par les algorithmes de segmentation automatique de *Freesurfer*.

7.6.2 Perspectives

Des travaux futurs pourraient améliorer les descriptions statistiques du cortex à l'aide des s-reps et CPNS. Ces méthodes proposent de nouvelles possibilités pour décrire la variabilité de forme dans des groupes de patients normaux où pathologiques, pour différents sujets lors d'un suivi longitudinal.

Aujourd'hui, le processus de pliage du cortex n'est pas bien compris. Décrivant les variabilités de forme du cortex d'un point de vue statistique, la méthode s-reps peut aider les chercheurs à comprendre quelles sont les variations de forme principales et comment le cerveau humain se développe.

Un deuxième objectif serait d'améliorer les procédures de simulation d'images en créant un atlas du cerveau à l'aide de s-reps. Une première étape devrait être d'acquérir les meilleurs échantillons de paramètres physiques. Les échantillons texturés ne contiennent pas d'information structurelle et ils ont une faible résolution. La prochaine étape serait de générer les descriptions statistiques des structures sous-corticales et du cortex, pour les sujets de normaux et les sujets pathologiques. Avec les descriptions statistiques et quelques coefficients, un jeu complètement différent des structures peut être généré.

Un troisième objectif serait de créer une méthodologie capable d'estimer des fonctions scalaires basées sur la description de la forme d'un objet. Par exemple, il serait possible d'estimer la densité des noyaux dans le thalamus à partir de sa forme modélisé avec un srep. La densité des noyaux dans le thalamus n'est visible que dans des séquences d'acquisition IRM particulières. Malheureusement, cette acquisition n'est pas faite systématiquement.

La procédure utilisera les images *T1*-pondérées segmentées pour l'ajustement d'un srep au thalamus. L'ajustement produit des représentations précises du thalamus et augmente la correspondance entre les positions internes $[u, v, \tau]$ entre deux patient.

Des statistiques de forme seront calculées à l'aide de CPNS, et une analyse statistique faite pour la densité des noyaux en utilisant le système de coordonnées $[u, v, \tau]$. Cela est possible puisque les positions internes sont en correspondance.

Les statistiques contiendront des informations sur la forme et la densité des noyaux à chaque position interne du srep.

Pour estimer la densité des noyaux dans un nouveau thalamus, la forme moyenne produite par le CPNS est ajusté sur la structure segmentée. La densité des noyaux peut être estimée sur la base de la déformation et la description statistique de densité.

Cette approche pourrait être utilisée pour détecter d'autres types de fonctions scalaires.

Appendices

Appendix A

Principal Component Analysis

Principal Component Analysis (PCA) is a way of identifying patterns in the data. PCA is able to detect the principal directions of variation and is a powerful tool for analysing data that lives in high dimensional spaces. Common uses of PCA are to produce compress or compact datasets by finding and removing redundant information. After the compression, any of the points in the original dataset can be represented using a small number of parameters.

The following sections explains how to use PCA.

A.1 Computing PCA

The mean of the data must be substracted from each dimension for PCA to work properly. By doing this, the data set has mean zero.

A.1.1 Compute the mean

$$\bar{x} = \frac{1}{s} \sum_{i=1}^s x_i \quad (\text{A.1})$$

x is a dataset where each column represents an object from the population. s is the number of objects in x , \bar{x} is a vector with the mean of the data calculated for each dimension.

A.1.2 Compute the covariance of the data

$$cov(X, Y) = \frac{1}{s-1} \sum_{i=1}^s (X_i - \bar{X})(Y_i - \bar{Y}) \quad (\text{A.2})$$

$$C = C_{ab} = cov(Row(x, a), Row(x, b)) \quad (\text{A.3})$$

The covariance matrix C A.3 is a square matrix that contains at each position the covariance A.2 between the a and b dimension of the dataset x . Notice that when $a = b$ we get the regular variance. $Row(x, a)$ retrieves row a from the data.

A.1.3 Perform eigenanalysis on the covariance

$$C = Q\Lambda Q^{-1} \quad (\text{A.4})$$

Equation A.4 shows how to perform an eigenanalysis where Q is a square matrix whose i^{th} column is the eigenvector q_i of C and Λ is the diagonal matrix whose diagonal elements are the corresponding eigenvalues λ_i , i.e., $\Lambda_{ii} = \lambda_i$. All eigenvectors must satisfy the following:

$$Cq_i = \lambda_i q_i \quad (\text{A.5})$$

where λ_i is the eigenvalue associated to the eigenvector q_i . The eigenvectors have unit length, and the eigenvalues are sorted so that $\lambda_i \geq \lambda_{i+1}$.

A.1.4 Compute the total variance

$$V_t = \sum_t \lambda_i \quad (\text{A.6})$$

Each eigenvalue gives the variance of the data about the mean in the direction of the corresponding eigenvector.

A.1.5 Use a number of eigenvalues

$$\sum_{i=1}^t \lambda_i \geq f_v V_t \quad (\text{A.7})$$

To represent the data with the most significative information a number of eigenvectors P is chosen by using their corresponding eigenvalues. As show in equation A.7, $f_v \in [0, 1]$ defines the proportion of the total variation in the data that is going to be explained. For example: in order to explain 95% of the information, $f_v = 0.95$, this means that the first n eigenvectors are used whose eigenvalues add up to $0.95V$.

A.2 Producing a compact data set

To produce the compressed data set, a matrix $P_t = (p_1|p_2|\dots|p_t)$ of the eigenvectors chosen to describe the dataset is used, as shown in equation A.7. The matrix P_t is multiplied by the adjusted data set, yielding x_c , a compact representation of the data, as shown in equation A.8.

$$x_c = P_t^T(x - \bar{x}) \quad (\text{A.8})$$

A.3 Recovering the original data

In some situations such as compression, getting the original data back is important. When a reduced number of eigenvectors is used, the transformation to get the original data, loses some information. Notice that the only way to get the original data back is by using all the eigenvectors.

$$(x - \bar{x}) = (P_{t=n}^T)^{-1} x_c \quad (\text{A.9})$$

In the case where all the eigenvectors are used, it turns out that the inverse of P_n is equal to the transpose, so $(P_t^T)^{-1} = P_t$. This step also applies even when a set of eigenvectors is used, but as mentioned before some data is lost during the final transformation, as shown in Equation A.10

$$x = P_n x_c + \bar{x} \quad (\text{A.10})$$

Appendix B

Principal Nested Spheres

PNS (Principal Nested Spheres) is an extension of PCA proposed to analyze data that lives on spherical manifolds. Examples of such data are directions like the spokes in s-reps (see Section 2.3.3). Similarly to principal directions in PCA, PNS finds principal arcs through the data and gives a mechanism for dimension reduction. The term principal arc is defined by [Jung *et al.* (2011)].

This appendix is an overview of PNS, highlighting the construction of the Nested Spheres and decomposition onto principal arcs. For details on the approach see [Jung *et al.* (2012)].

PNS gives a more suited description of the data when major variations can be best described by potential arcs that are either small circles or great circles. This is in contrast to PGA (principal geodesic analysis), which describes data variations using geodesics [Fletcher *et al.* (2004)], [Huckemann *et al.* (2010)].

PNS decomposes the data space so that the major one-dimensional variation becomes linearly represented. For a unit *d-sphere* S^d , which is the set of unit vectors in R^{d+1} . The analysis gives a decomposition of S^d that captures the variation in a lower dimensional subsphere. The subspheres are small spheres or great spheres depending on the type of analysis, *i.e.*, by small circles or great circles. The type of analysis can be set by default or selected automatically with a hypothesis test that decides which type of subsphere to use.

The sequential decomposition provides the best k-dimensional approximation Ψ_k of the data for each $k = \{0, 1, \dots, d - 1\}$. The sphere Ψ_k is called the k-dimensional principal nested sphere and is a submanifold of the higher dimensional principal nested spheres. The sequence of principal nested spheres is

$$\Psi_0 \subset \Psi_1 \subset \dots \subset \Psi_{d-1} \subset S^d. \quad (\text{B.1})$$

The procedure of fitting principal nested spheres involves iterative reduction of the data dimension. The following section explains how to analyze the data using PNS.

B.1 Computing PNS

B.1.1 Arc distance

Equation B.2 shows the arc distance function between two points x and y . The solution is unique unless the points are antipodal, *i.e.*, $x^T y = -1$.

$$\rho_d(x, y) = \cos^{-1}(x^T y) \quad (\text{B.2})$$

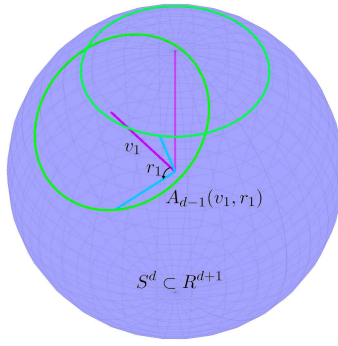


Figure B.1: Rotation of the sub-sphere A_{d-1} to the northpole.

B.1.2 Subsphere

Equation B.3 shows the definition of a subsphere A_{d-1} of S^d , defined by an axis $v \in S^d$ and a distance $r \in (0, \pi/2]$.

$$A_{d-1}(v, r) = \{x \in S^d : \rho_d(v, x) = r\} \quad (\text{B.3})$$

The subsphere A_{d-1} is an intersection of $S^d \subset R^{d+1}$ with a d -dimensional hyperplane such that $\{x \in R^{d+1} : v^T x - \cos(r) = 0\}$.

B.1.3 Rotation to the north pole

Suppose that a and b are unit vectors in R^m , the rotation matrix $\Omega(a, b)$ moves a to b along a minimal path on the unit sphere. [Amaral *et al.* (2007)] defined a rotation matrix as

$$\begin{aligned} A &= ac^T - ca^T \\ c &= b - a(a^T b)/\|b - a(a^T b)\| \\ \theta &= \rho_d(a, b) \\ \Omega(a, b) &= I_d + \sin(\theta)A + \cos(\theta) - 1(aa^T + cc^T). \end{aligned} \quad (\text{B.4})$$

B.1.4 Transformation of subsphere

$$\begin{aligned} f_k(x) &= \frac{1}{\sin(r_k)} R^-(v_k)x, x \in A_{d-k} \\ f_k^{-1}(x^\dagger) &= R^T(v_k) \begin{bmatrix} \sin(r_k) \cdot x^\dagger \\ \cos(r_k) \end{bmatrix}, x^\dagger \in S^{d-k} \end{aligned} \quad (\text{B.5})$$

Equation B.5 shows the function f that enables going from a sphere dimension S^d to a sub-sphere S^{d-1} and the corresponding inverse, where $x \in A_{d-1}$, $x^\dagger \in S^{d-k}$. Matrix R , rotates the data to the north pole. $R = \Omega(v_k, e_k)$, where e_k is the north pole, *i.e.*, $e_k = (0, \dots, 0, 1)^T$. R^- is the $m \times m + 1$ matrix consisting of the first m rows of R .

B.1.5 Best fitting subsphere

Let x_1, \dots, x_n be a sample in S^d , $d \geq 2$. The shortest distance from x to a subshpere $A_{d-1}(v_1, r_1)$ of S^d is the lenght of the minimal path that joins x to A_{d-1} .

The best fitting subsphere $\hat{A}_{d-1} = A_{d_1}(\hat{v}_1, \hat{r}_1)$ is found by minimizing the sum of squares of residuals of the data points to \hat{A}_{d-1} . Equation B.6 shows the procedure to find the best fitting subsphere.

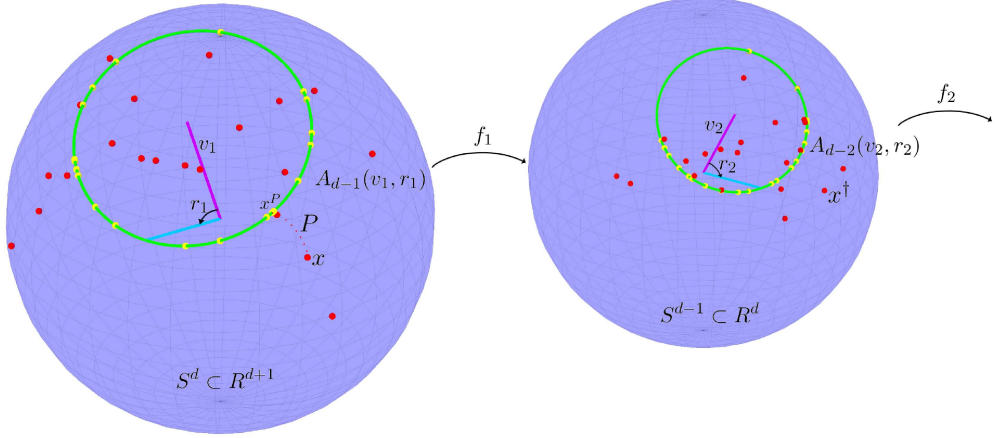


Figure B.2: The data points x are shown in red, the best fitting sub-sphere to the data is shown in green $A_{d-1}(v_1, r_1)$, the vector v_1 is shown in magenta, the projected data points $x^P = P(x)$ in yellow on top of the best fitting circle. Function $x^\dagger = f_1(x^P)$ takes the projected points on $A_{d-1}(v_1, r_1)$ to the sub-sphere S^{d-1} .

$$\hat{A}_{d-1} = \operatorname{Arg\,min}_{v_1, r_1} \sum_{i=1}^n \varepsilon_i(v_1, r_1)^2 = \operatorname{Arg\,min}_{v_1, r_1} \sum_{i=1}^n (\rho_d(x_i, v_1) - r_1)^2 \quad (\text{B.6})$$

Once the sub-sphere is found the points are projected to it, as shown in Equation B.7.

$$P(x, A_{d-1}(v, r)) = \frac{\sin(r)x + \sin(\rho_d(x, v) - r)v}{\sin(\rho_d(x, v))} \quad (\text{B.7})$$

Let $x^P = P(x, \hat{A}_{d-1})$ be the projected point on the sub-sphere. x^P can be transformed from \hat{A}_{d-1} to S^{d-1} using the formula defined at B.5, $x^\dagger = f(x^P)$ with $v_k = \hat{v}_1$ and $r_k = \hat{r}_1$.

Figure B.2 shows an example of finding the best fitting sub-sphere for the data points.

B.1.6 Sequence of principal nested spheres

The method finds the sequence of best fitting sub-spheres from the projected data points $\hat{f}(P(x, \hat{A}_{d-k})) \in S^{d-k}$ ($x \in S^{d-k+1}$). When a sub-sphere is fitted, the residuals defined by $\varepsilon_{i,d-k}$ are kept for later use as analogues of principal component scores.

The lowest best fitting sub-sphere \hat{A}_1 is a small circle isomorphic to S^1 . Since no further sphere or circle can be used to reduce the dimensionality, the Fréchet mean is computed. Equation B.8 defines the Fréchet mean [Fréchet (1944)], [Fréchet (1948)], [Karcher (1977)], [Bhattacharya and Patrangenaru (2003)].

$$\hat{A}_0 = \operatorname{Arg\,min}_{x \in S^1} \sum_{i=1}^n \rho_1(x, x_i^\dagger)^2 \quad (\text{B.8})$$

The sequence of principal nested spheres in S^d is $\{\hat{\Psi}_0, \dots, \hat{\Psi}_{d-1}\}$, where $\hat{\Psi}_{d-k}$ is defined as shown in Equation B.9. $\hat{\Psi}_0$ is the principal nested spheres mean.

$$\hat{\Psi}_{d-k} = \begin{cases} \hat{f}_1^{-1} \circ \dots \circ \hat{f}_{k-1}^{-1} & (k = 2, \dots, d), \\ \hat{A}_{d-1} & (k = 1) \end{cases} \quad (\text{B.9})$$

Similarly, the mean value \hat{A}_0 can be projected back to S^d by recursively composing the inverse functions as shown in Equation B.9.

B.2 Residuals and principal arcs

The signed residuals $\varepsilon_{i,d-k}$ ($i = 1, \dots, n$) collected during the fitting process are rescaled to make them commensurate. This is done by multiplying $\prod_{i=1}^{k-1} \sin(\hat{r}_i)$ to the residuals as

$$\Xi(d-k)_{1 \times n} = \prod_{i=1}^{k-1} \sin(\hat{r}_i)(\varepsilon_{i,d-k}, \dots, \varepsilon_{n,d-k}). \quad (\text{B.10})$$

where $(\varepsilon_{i,d-k}, \dots, \varepsilon_{n,d-k})$ is a row vector of residuals.

The commensurate residuals are combined into a $d \times n$ matrix. Each entry in $\Xi(k)$ lies in a subset of $E = [\pi, \pi] \times [-\pi/2, \pi/2]^{d-1}$ and correspond to the sample's coordinates in terms of the principal nested sphere.

$$\hat{X}_{PNS} = \begin{bmatrix} \Xi(0) \\ \Xi(1) \\ \vdots \\ \vdots \\ \Xi(d-1) \end{bmatrix} \quad (\text{B.11})$$

To compute the principal arcs (analogues to principal directions), each point in S^d can be mapped to E using the projection B.7 and rescaling. Leading to a mapping $h : S^d \rightarrow E$. The k th principal arc γ_k coincides with direction e_k and is parameterized by $\gamma_k(t) = h(te_k)$, where e_k is a vector of zeros with 1 at the k th position.

The matrix \hat{X}_{PNS} can be used to visualize the structure of the data. Further analysis can be done on \hat{X}_{PNS} using conventional multivariate statistics based on Euclidean geometry such as PCA.

Bibliography

- [Amaral *et al.* (2007)] Amaral, G. A., Dryden, I., and Wood, A. T. A. (2007). Pivotal bootstrap methods for k-sample problems in directional statistics and shape analysis. *Journal of the American Statistical Association*, 102(478):695–707.
- [Amenta *et al.* (2001)] Amenta, N., Choi, S., and Kolluri, R. K. (2001). The power crust, unions of balls, and the medial axis transform. *Computational Geometry*, 19(2):127–153.
- [Ashikhmin (2001)] Ashikhmin, M. (2001). Synthesizing natural textures. In *Proceedings of the 2001 symposium on Interactive 3D graphics*, pages 217–226. ACM.
- [Aspert *et al.* (2002)] Aspert, N., Santa-Cruz, D., and Ebrahimi, T. (2002). Mesh: Measuring errors between surfaces using the hausdorff distance. In *Multimedia and Expo, 2002. ICME'02. Proceedings. 2002 IEEE International Conference on*, volume 1, pages 705–708.
- [Aydm *et al.* (2011)] Aydm, B., Pataki, G., Wang, H., Ladha, A., Bullitt, E., and Marron, J. (2011). Visualizing the structure of large trees. *Electronic Journal of Statistics*, 5:405–420.
- [Bayly *et al.* (2013)] Bayly, P., Taber, L., and Kroenke, C. (2013). Mechanical forces in cerebral cortical folding: a review of measurements and models. *Journal of the mechanical behavior of biomedical materials*.
- [Benoit-Cattin *et al.* (2005)] Benoit-Cattin, H., Collewet, G., Belaroussi, B., Saint-Jalmes, H., and Odet, C. (2005). The simri project: a versatile and interactive mri simulator. *Journal of Magnetic Resonance*, 173(1):97–115.
- [Bergen and Landy (1991)] Bergen, J. R. and Landy, M. S. (1991). Computational modeling of visual texture segregation. *Computational models of visual processing*, pages 253–271.
- [Bhattacharya and Patrangenaru (2003)] Bhattacharya, R. and Patrangenaru, V. (2003). Large sample theory of intrinsic and extrinsic sample means on manifolds. i. *Annals of statistics*, pages 1–29.
- [Binford (1971)] Binford, T. O. (1971). Visual perception by computer. In *IEEE conference on Systems and Control*, volume 261, page 262.
- [Blum *et al.* (1967)] Blum, H. *et al.* (1967). A transformation for extracting new descriptors of shape. *Models for the perception of speech and visual form*, 19(5):362–380.
- [Bookstein (1991)] Bookstein, F. (1991). Morphometric tools for landmark data. cambridge, new york, port chester.

- [Bradley *et al.* (1997)] Bradley, C., Pullan, A., and Hunter, P. (1997). Geometric modeling of the human torso using cubic hermite elements. *Annals of Biomedical Engineering*, 25(1):96–111.
- [Brechbühler *et al.* (1995)] Brechbühler, C., Gerig, G., and Kübler, O. (1995). Parametrization of closed surfaces for 3-d shape description. *Computer vision and image understanding*, 61(2):154–170.
- [Brown (1992)] Brown, L. G. (1992). A survey of image registration techniques. *ACM computing surveys (CSUR)*, 24(4):325–376.
- [Buettner-Janusch (1964)] Buettner-Janusch, J. (1964). *Evolutionary and genetic biology of primates*, volume 2. Academic Press.
- [Cao *et al.*] Cao, F., Commowick, O., Bannier, E., Crimi, A., and Barillot, C. M3. 3.2– validation study of the brain model for ms uspio-enhanced diagnosis.
- [Cao *et al.* (2005)] Cao, Y., Miller, M. I., Winslow, R. L., and Younes, L. (2005). Large deformation diffeomorphic metric mapping of vector fields. *Medical Imaging, IEEE Transactions on*, 24(9):1216–1230.
- [Castella *et al.* (2008)] Castella, C., Kinkel, K., Descombes, F., Eckstein, M., Sottas, P., Verdun, F., and Bochud, F. (2008). Mammographic texture synthesis: second-generation clustered lumpy backgrounds using a genetic algorithm. *Opt. Express*, 16(11):7595–7607.
- [Chan and Vese (2001)] Chan, T. F. and Vese, L. A. (2001). Active contours without edges. *Image Processing, IEEE Transactions on*, 10(2):266–277.
- [Charpigny *et al.* (2009)] Charpigny, D., Grenier, T., Odet, C., and Benoit-Cattin, H. (2009). Towards iron oxide nanoparticles quantization in molecular mr images by default field deconvolution. In *Proc. ISBI 2009: 6th IEEE international symposium on biomedical imaging*.
- [Chen and Wang (2010)] Chen, J. and Wang, B. (2010). High quality solid texture synthesis using position and index histogram matching. *The Visual Computer*, 26(4):253–262.
- [Cootes *et al.* (1995)] Cootes, T. F., Taylor, C. J., Cooper, D. H., and Graham, J. (1995). Active shape models-their training and application. *Computer vision and image understanding*, 61(1):38–59.
- [Cootes *et al.* (2001)] Cootes, T. F., Edwards, G. J., and Taylor, C. J. (2001). Active appearance models. *Pattern Analysis and Machine Intelligence, IEEE Transactions on*, 23(6):681–685.
- [Culver *et al.* (1999)] Culver, T., Keyser, J., and Manocha, D. (1999). Accurate computation of the medial axis of a polyhedron. In *Proceedings of the fifth ACM symposium on Solid modeling and applications*, pages 179–190. ACM.
- [Damon (2003)] Damon, J. (2003). Smoothness and geometry of boundaries associated to skeletal structures i: Sufficient conditions for smoothness. In *Annales de l'institut Fourier*, volume 53, page 1941. Chartres: L’Institut, 1950-.
- [Damon (2008)] Damon, J. (2008). Swept regions and surfaces: Modeling and volumetric properties. *Theoretical Computer Science*, 392(1):66–91.

- [Defelipe *et al.* (2012)] Defelipe, J., Markram, H., and Rockland, K. S. (2012). The neo-cortical column. *Frontiers in Neuroanatomy*, 6.
- [Drury *et al.* (1996)] Drury, H. A., Van Essen, D. C., Anderson, C. H., Lee, C. W., Coogan, T. A., and Lewis, J. W. (1996). Computerized mappings of the cerebral cortex: a multiresolution flattening method and a surface-based coordinate system. *Journal of cognitive neuroscience*, 8(1):1–28.
- [Dryden and Mardia (1993)] Dryden, I. and Mardia, K. (1993). Multivariate shape analysis. *Sankhyā: The Indian Journal of Statistics, Series A*, pages 460–480.
- [Efros and Leung (1999)] Efros, A. A. and Leung, T. K. (1999). Texture synthesis by non-parametric sampling. In *Computer Vision, 1999. The Proceedings of the Seventh IEEE International Conference on*, volume 2, pages 1033–1038. IEEE.
- [Filas *et al.* (2013)] Filas, B. A., Xu, G., and Taber, L. A. (2013). Mechanisms of brain morphogenesis. In *Computer Models in Biomechanics*, pages 337–349. Springer.
- [Fischl *et al.* (1999)] Fischl, B., Sereno, M. I., and Dale, A. M. (1999). Cortical surface-based analysis: II: inflation, flattening, and a surface-based coordinate system. *NeuroImage*, 9(2):195 – 207.
- [Fischl *et al.* (2002)] Fischl, B., Salat, D. H., Busa, E., Albert, M., Dieterich, M., Haselgrove, C., van der Kouwe, A., Killiany, R., Kennedy, D., Klaveness, S., *et al.* (2002). Whole brain segmentation: automated labeling of neuroanatomical structures in the human brain. *Neuron*, 33(3):341–355.
- [Fischl *et al.* (2004)] Fischl, B., Van Der Kouwe, A., Destrieux, C., Halgren, E., Ségonne, F., Salat, D. H., Busa, E., Seidman, L. J., Goldstein, J., Kennedy, D., *et al.* (2004). Automatically parcellating the human cerebral cortex. *Cerebral Cortex*, 14(1):11–22.
- [Fisker (2000)] Fisker, R. (2000). *Making deformable template models operational*. Institute of Mathematical Modelling, Technical University of Denmark.
- [Fletcher *et al.* (2004)] Fletcher, P. T., Lu, C., Pizer, S. M., and Joshi, S. (2004). Principal geodesic analysis for the study of nonlinear statistics of shape. *Medical Imaging, IEEE Transactions on*, 23(8):995–1005.
- [Fréchet (1944)] Fréchet, M. (1944). *L'intégrale abstraite d'une fonction abstraite d'une variable abstraite et son application à la moyenne d'un élément aléatoire de nature quelconque*. La Revue Scientifique.
- [Fréchet (1948)] Fréchet, M. (1948). Les éléments aléatoires de nature quelconque dans un espace distancié. In *Annales de l'institut Henri Poincaré*, volume 10, pages 215–310. Presses universitaires de France.
- [Geng *et al.* (2009)] Geng, G., Johnston, L. A., Yan, E., Britto, J. M., Smith, D. W., Walker, D. W., and Egan, G. F. (2009). Biomechanisms for modelling cerebral cortical folding. *Medical image analysis*, 13(6):920–930.
- [Glatard *et al.* (2011)] Glatard, T., Lartizien, C., Gibaud, B., Ferreira da Silva, R., Forestier, G., Cervenansky, F., Benoit-Cattin, H., Montagnat, J., Tabary, J., and Friboulet, D. (2011). A virtual imaging platform for multi-modality medical image simulation.

- [Grenander and Miller (1998)] Grenander, U. and Miller, M. I. (1998). Computational anatomy: An emerging discipline. *Quarterly of applied mathematics*, 56(4):617–694.
- [Han *et al.* (2006)] Han, Q., Pizer, S. M., and Damon, J. N. (2006). Interpolation in discrete single figure medial objects. In *Computer Vision and Pattern Recognition Workshop, 2006. CVPRW'06. Conference on*, pages 85–85. IEEE.
- [Heeger and Bergen (1995)] Heeger, D. J. and Bergen, J. R. (1995). Pyramid-based texture analysis/synthesis. In *Proceedings of the 22nd annual conference on Computer graphics and interactive techniques, SIGGRAPH '95*, pages 229–238, New York, NY, USA. ACM.
- [Heimann *et al.* (2007)] Heimann, T., Münzing, S., Meinzer, H.-P., and Wolf, I. (2007). A shape-guided deformable model with evolutionary algorithm initialization for 3d soft tissue segmentation. In *Information Processing in Medical Imaging*, pages 1–12. Springer.
- [Hermosillo *et al.* (1999)] Hermosillo, G., Faugeras, O., and Gomes, J. (1999). Unfolding the cerebral cortex using level set methods. *Scale-Space Theories in Computer Vision*, pages 58–69.
- [Hill *et al.* (2000)] Hill, A., Taylor, C. J., and Brett, A. D. (2000). A framework for automatic landmark identification using a new method of nonrigid correspondence. *Pattern Analysis and Machine Intelligence, IEEE Transactions on*, 22(3):241–251.
- [Hipp and Simmons (1997)] Hipp, J. and Simmons, C. (1997). Method-based differences in the automated analysis of the three-dimensional morphology of trabecular bone. *Journal of Bone and Mineral Research*, 12.
- [Huang and Stockman (1993)] Huang, Q. and Stockman, G. C. (1993). Generalized tube model: Recognizing 3d elongated objects from 2d intensity images. In *Computer Vision and Pattern Recognition, 1993. Proceedings CVPR'93., 1993 IEEE Computer Society Conference on*, pages 104–109. IEEE.
- [Huckemann *et al.* (2010)] Huckemann, S., Hotz, T., and Munk, A. (2010). Rejoinder-intrinsic shape analysis: Geodesic pca for riemannian manifolds modulo isometric lie group actions.
- [James Rohlf and Marcus (1993)] James Rohlf, F. and Marcus, L. F. (1993). A revolution in morphometrics. *Trends in Ecology & Evolution*, 8(4):129–132.
- [Jean-Loic *et al.*] Jean-Loic, R., Chantal, R.-M., Christophe, O., and Christian, R. Variational region growing.
- [Jensen (2004)] Jensen, J. A. (2004). Simulation of advanced ultrasound systems using field ii. In *Biomedical Imaging: Nano to Macro, 2004. IEEE International Symposium on*, pages 636–639. IEEE.
- [Joshi and Miller (2000)] Joshi, S. C. and Miller, M. I. (2000). Landmark matching via large deformation diffeomorphisms. *Image Processing, IEEE Transactions on*, 9(8):1357–1370.
- [Julész *et al.* (1978)] Julész, B., Gilbert, E., and Victor, J. (1978). Visual discrimination of textures with identical third-order statistics. *Biological cybernetics*, 31(3):137–140.

- [Jung *et al.* (2011)] Jung, S., Foskey, M., and Marron, J. (2011). Principal arc analysis on direct product manifolds. *The Annals of Applied Statistics*, 5(1):578–603.
- [Jung *et al.* (2012)] Jung, S., Dryden, I. L., and Marron, J. S. (2012). Analysis of principal nested spheres. *Biometrika*.
- [Kabul *et al.* (2011)] Kabul, I., Pizer, S. M., Rosenman, J., and Niethammer, M. (2011). An optimal control approach for texture metamorphosis. In *Computer Graphics Forum*, volume 30, pages 2341–2353. Wiley Online Library.
- [Kaplan *et al.* (2009)] Kaplan, R. F., Cohen, R. A., Moscufo, N., Guttmann, C., Chasman, J., Buttaro, M., Hall, C. H., and Wolfson, L. (2009). Demographic and biological influences on cognitive reserve. *Journal of Clinical and Experimental Neuropsychology*, 31(7):868–876. PMID: 19333862.
- [Karcher (1977)] Karcher, H. (1977). Riemannian center of mass and mollifier smoothing. *Communications on pure and applied mathematics*, 30(5):509–541.
- [Kass *et al.* (1988)] Kass, M., Witkin, A., and Terzopoulos, D. (1988). Snakes: Active contour models. *International journal of computer vision*, 1(4):321–331.
- [Katz and Pizer (2003)] Katz, R. A. and Pizer, S. M. (2003). Untangling the blum medial axis transform. *International Journal of Computer Vision*, 55(2-3):139–153.
- [Kendall (1989)] Kendall, D. G. (1989). A survey of the statistical theory of shape. *Statistical Science*, 4(2):87–99.
- [Kopf *et al.* (2007)] Kopf, J., Fu, C.-W., Cohen-Or, D., Deussen, O., Lischinski, D., and Wong, T.-T. (2007). Solid texture synthesis from 2d exemplars. *ACM Transactions on Graphics (Proceedings of SIGGRAPH 2007)*, 26(3):2:1–2:9.
- [Kwatra *et al.* (2003)] Kwatra, V., Schödl, A., Essa, I., Turk, G., and Bobick, A. (2003). Graphcut textures: image and video synthesis using graph cuts. In *ACM Transactions on Graphics (TOG)*, volume 22, pages 277–286. ACM.
- [Kwatra *et al.* (2005)] Kwatra, V., Essa, I., Bobick, A., and Kwatra, N. (2005). Texture optimization for example-based synthesis. *ACM Transactions on Graphics, SIGGRAPH 2005*.
- [Kybic (2010)] Kybic, J. (2010). Bootstrap resampling for image registration uncertainty estimation without ground truth. *Image Processing, IEEE Transactions on*, 19(1):64–73.
- [Lagae *et al.* (2009)] Lagae, A., Lefebvre, S., Drettakis, G., and Dutré, P. (2009). Procedural noise using sparse gabor convolution. In *ACM Transactions on Graphics (TOG)*, volume 28, page 54. ACM.
- [Landy and Graham (2004)] Landy, M. S. and Graham, N. (2004). Visual perception of texture. *The visual neurosciences*, 2:1106–1118.
- [Lefebvre and Hoppe (2006)] Lefebvre, S. and Hoppe, H. (2006). Appearance-space texture synthesis. *ACM Trans. Graph.*, 25:541–548.

- [Leung and Malik (2001)] Leung, T. and Malik, J. (2001). Representing and recognizing the visual appearance of materials using three-dimensional textons. *International Journal of Computer Vision*, 43(1):29–44.
- [Le Maitre *et al.* (2009)] Le Maitre, A., Segars, W. P., Marache, S., Reilhac, A., Hatt, M., Tomei, S., Lartizien, C., and Visvikis, D. (2009). Incorporating patient-specific variability in the simulation of realistic whole-body \leq formula formulatype=. *Proceedings of the IEEE*, 97(12):2026–2038.
- [Liang *et al.* (2001)] Liang, L., Liu, C., Xu, Y.-Q., Guo, B., and Shum, H.-Y. (2001). Real-time texture synthesis by patch-based sampling. *ACM Transactions on Graphics (ToG)*, 20(3):127–150.
- [Liu *et al.* (2011)] Liu, L., Chambers, E. W., Letscher, D., and Ju, T. (2011). Extended grassfire transform on medial axes of 2d shapes. *Computer-Aided Design*, 43(11):1496–1505.
- [Lorente de Nó (1934)] Lorente de Nó, R. (1934). Studies on the structure of the cerebral cortex. ii. continuation of the study of the ammonic system. *Journal für Psychologie und Neurologie*.
- [Marion *et al.* (2011)] Marion, A., Forestier, G., Benoit-Cattin, H., Camarasu-Pop, S., Clarysse, P., da Silva, R. F., Gibaud, B., Glatard, T., Hugonnard, P., Lartizien, C., *et al.* (2011). Multi-modality medical image simulation of biological models with the virtual imaging platform (vip). In *Computer-Based Medical Systems (CBMS), 2011 24th International Symposium on*, pages 1–6. IEEE.
- [Merck (2009)] Merck, D. (2009). *Model guided rendering for medical images*. PhD thesis, University of North Carolina.
- [Miklos *et al.* (2010)] Miklos, B., Giesen, J., and Pauly, M. (2010). Discrete scale axis representations for 3d geometry. *ACM Transactions on Graphics (TOG)*, 29(4):101.
- [Mitchell *et al.* (2002)] Mitchell, S. C., Bosch, J. G., Lelieveldt, B. P., van der Geest, R. J., Reiber, J. H., and Sonka, M. (2002). 3-d active appearance models: Segmentation of cardiac mr and ultrasound images. *IEEE TRANSACTIONS ON MEDICAL IMAGING*, 21(9):1167.
- [Mohlenkamp (2010)] Mohlenkamp, M. J. (2010). A user’s guide to spherical harmonics.
- [Mountcastle (1998)] Mountcastle, V. B. (1998). *Perceptual neuroscience: The cerebral cortex*. Harvard University Press.
- [Mumford and Shah (1989)] Mumford, D. and Shah, J. (1989). Optimal approximations by piecewise smooth functions and associated variational problems. *Communications on pure and applied mathematics*, 42(5):577–685.
- [Narayanan *et al.* (2005)] Narayanan, R., Fessler, J. A., Park, H., and Meyer, C. R. (2005). Diffeomorphic nonlinear transformations: A local parametric approach for image registration. In *Information Processing in Medical Imaging*, pages 174–185. Springer.
- [Netter (2010)] Netter, F. H. (2010). *Atlas of human anatomy*. Elsevier Health Sciences.
- [Nowell] Nowell, P. Math proofs: Mapping a square to a circle. <http://mathproofs.blogspot.fr/2005/07/mapping-square-to-circle.html>.

- [Odgaard and Gundersen (1993)] Odgaard, A. and Gundersen, H. (1993). Quantification of connectivity in cancellous bone, with special emphasis on 3d reconstructions. *Bone*, 14:173–182.
- [Olshausen and Field (1997)] Olshausen, B. A. and Field, D. J. (1997). Sparse coding with an overcomplete basis set: A strategy employed by v1? *Vision research*, 37(23):3311–3325.
- [Peachey (1985)] Peachey, D. R. (1985). Solid texturing of complex surfaces. In *ACM SIGGRAPH Computer Graphics*, volume 19, pages 279–286. ACM.
- [Perlin (1985)] Perlin, K. (1985). An image synthesizer. *SIGGRAPH Comput. Graph.*, 19(3):287–296.
- [Pizer *et al.* (1999)] Pizer, S. M., Fritsch, D. S., Yushkevich, P. A., Johnson, V. E., and Chaney, E. L. (1999). Segmentation, registration, and measurement of shape variation via image object shape. *Medical Imaging, IEEE Transactions on*, 18(10):851–865.
- [Pizer *et al.* (2003)] Pizer, S. M., Fletcher, P. T., Joshi, S., Thall, A., Chen, J. Z., Fridman, Y., Fritsch, D. S., Gash, A. G., Glotzer, J. M., Jiroutek, M. R., *et al.* (2003). Deformable m-reps for 3d medical image segmentation. *International Journal of Computer Vision*, 55(2-3):85–106.
- [Pizer *et al.* (2005)] Pizer, S. M., Fletcher, P. T., Joshi, S., Gash, A. G., Stough, J., Thall, A., Tracton, G., and Chaney, E. L. (2005). A method and software for segmentation of anatomic object ensembles by deformable m-reps. *Medical Physics*, 32:1335.
- [Pizer *et al.* (2012)] Pizer, S., Jung, S., Goswami, D., Zhao, X., Chaudhuri, R., Damon, J., Huckemann, S., and Marron, J. (2012). Nested sphere statistics of skeletal models. In *To appear in Proc. Dagstuhl Workshop on Innovations for Shape Analysis*.
- [Pohl *et al.* (2007)] Pohl, K., Bouix, S., Nakamura, M., Rohlfing, T., McCarley, R., Kikinis, R., Grimson, W., Shenton, M., and Wells, W. (2007). A hierarchical algorithm for mr brain image parcellation. *IEEE Transactions on Medical Imaging*, 26(9):1201–1212.
- [Pons *et al.* (2004)] Pons, J.-P., Keriven, R., and Faugeras, O. (2004). Area preserving cortex unfolding. *Medical Image Computing and Computer-Assisted Intervention-MICCAI 2004*, pages 376–383.
- [Praun *et al.* (2000)] Praun, E., Finkelstein, A., and Hoppe, H. (2000). Lapped textures. In *Proceedings of the 27th annual conference on Computer graphics and interactive techniques*, pages 465–470. ACM Press/Addison-Wesley Publishing Co.
- [Prieto *et al.* (2011)] Prieto, J., Revol-Muller, C., and Odet, C. (2011). Modélisation multiparamétrique d'organes basée sur le codage de la structure interne.
- [Prieto *et al.* (2012)a] Prieto, J., Mihaila, S., Hilaire, A., Fanton, L., Odet, C., and Revol-Muller, C. (2012a). Age estimation from 3d x-ray ct images of human fourth ribs. In *Worldcomp'12: 16th International Conference on Image Processing, Computer Vision, & Pattern Recognition IPCV'12*, Las Vegas, Nevada, USA.
- [Prieto *et al.* (2012)b] Prieto, J., Pérez Romanello, C., Pérez Romanello, V., Revol-Muller, C., Odet, C., Orkisz, M., and Hernández Hoyos, M. (2012b). Segmentación del árbol vascular pulmonar. In *XXXVIII Conferencia Latinoamericana en Informática (CLEI)*, pages 1–7, Medellín, Colombia.

- [Prieto *et al.* (2012)c] Prieto, J., Revol-Muller, C., Camelitti, P., and Odet, C. (2012c). Modeling 3d realistic organic tissues from 2d digital microscope images. In *ESMI "Hot Topics in molecular imaging" Topim'12*, page in press.
- [Prieto *et al.* (2012)d] Prieto, J., Revol-Muller, C., Odet, C., Orkisz, M., and Hernández Hoyos, M. (2012d). Crealungs: a variational region growing method to segment pulmonary vascular trees. In *ISBI VESSEL12 Challenge*, Barcelona, Spain.
- [Prieto *et al.* (2012)e] Prieto, J., Revol-Muller, C., Peyrin, F., Camelitti, P., and Odet, C. (2012e). 3d texture synthesis for modeling realistic organic tissues. In *VISAPP 2012. International Conference on Computer Vision Theory and Applications*, pages 60–65, Rome, Italy.
- [Raghavan *et al.* (1997)] Raghavan, R., Lawton, W., Ranjan, S., and Viswanathan, R. (1997). A continuum mechanics-based model for cortical growth. *Journal of theoretical biology*, 187(2):285–296.
- [Reilhac *et al.* (2004)] Reilhac, A., Lartizien, C., Costes, N., Sans, S., Comtat, C., Gunn, R. N., and Evans, A. C. (2004). Pet-sordeo: A monte carlo-based simulator with high count rate capabilities. *Nuclear Science, IEEE Transactions on*, 51(1):46–52.
- [Revol-Muller *et al.* (2002)] Revol-Muller, C., Benoit-Cattin, H., Carillon, Y., Odet, C., Briguet, A., and Peyrin, F. (2002). Bone mri segmentation assessment based on synchrotron radiation computed microtomography. *IEEE Trans Nucl Sci*, 49(1):220–224.
- [Rolland *et al.* (2000)] Rolland, J. P., Vo, V., Bloss, B., and Abbey, C. K. (2000). Fast algorithms for histogram matching: application to texture synthesis. *Journal of Electronic Imaging*, 9:39–45.
- [Saboo *et al.*] Saboo, R. R., Levy, J. H., Chaney, E. M., and Pizer, S. M. Medial models of populations of nearly tubular objects.
- [Saboo *et al.* (2011)] Saboo, R., Niethammer, M., North, M., and Pizer, S. (2011). Anti-aliasing discretely sampled object boundaries using fourth-order laplacian of curvature flow.
- [Sato *et al.* (1997)] Sato, Y., Nakajima, S., Atsumi, H., Koller, T., Gerig, G., Yoshida, S., and Kikinis, R. (1997). 3D multi-scale line filter for segmentation and visualization of curvilinear structures in medical images. In Troccaz, J., Grimson, E., and Mösges, R., editors, *CVRMed-MRCAS'97*, volume LNCS 1205, pages 213–222. Springer Berlin / Heidelberg.
- [Schröder and Sweldens (1995)] Schröder, P. and Sweldens, W. (1995). Spherical wavelets: Efficiently representing functions on the sphere. In *Proceedings of the 22nd annual conference on Computer graphics and interactive techniques*, pages 161–172. ACM.
- [Schulz *et al.* (2012)] Schulz, J., Pizer, S., Marron, J., and Godtliebsen, F. (2012). Nonlinear hypothesis testing of geometrical object properties of shapes applied to hippocampi.
- [Schwartz (2008)] Schwartz, E. (2008). Spherical Wavelets: A new tool for shape description. Technical Report PRIP-TR-118, Pattern Recognition and Image Processing Group (PRIP), Vienna University of Technology, Austria.

- [Segars *et al.* (2008)] Segars, W., Mahesh, M., Beck, T., Frey, E., and Tsui, B. (2008). Realistic ct simulation using the 4d xcat phantom. *Medical physics*, 35:3800.
- [Simonson (2011)] Simonson, K. M. (2011). Image registration with uncertainty analysis. US Patent 7,912,321.
- [Small (1996)] Small, C. (1996). The statistical theory of shape.
- [Snyder (1987)] Snyder, J. P. (1987). *Map projections-A working manual*. Number 1395. USGPO.
- [Styner *et al.* (2004)] Styner, M., Lieberman, J. A., Pantazis, D., and Gerig, G. (2004). Boundary and medial shape analysis of the hippocampus in schizophrenia. *Medical Image Analysis*, 8(3):197–203.
- [Styner and Gerig (2001)] Styner, M. and Gerig, G. (2001). Medial models incorporating object variability for 3d shape analysis. In *Information Processing in Medical Imaging*, pages 502–516. Springer.
- [Sørensen *et al.* (2011)] Sørensen, L., Lo, P., Dirksen, A., Petersen, J., and De Bruijne, M. (2011). Dissimilarity-based classification of anatomical tree structures. In *Information Processing in Medical Imaging*, pages 475–485. Springer.
- [Tabary *et al.* (2009)] Tabary, J., Marache-Francisco, S., Valette, S., Segars, W. P., and Lartizien, C. (2009). Realistic x-ray ct simulation of the xcat phantom with sindbad. In *Nuclear Science Symposium Conference Record (NSS/MIC), 2009 IEEE*, pages 3980–3983. IEEE.
- [Thall (2004)] Thall, A. L. (2004). *Deformable solid modeling via medial sampling and displacement subdivision*. PhD thesis, The University of North Carolina.
- [Tobon-Gomez *et al.* (2011)] Tobon-Gomez, C., Sukno, F., Bijnens, B., Huguet, M., and Frangi, A. (2011). Realistic simulation of cardiac magnetic resonance studies modeling anatomical variability, trabeculae, and papillary muscles. *Magnetic Resonance in Medicine*, 65(1):280–288.
- [Tong *et al.* (2002)] Tong, X., Zhang, J., Liu, L., Wang, X., Guo, B., and Shum, H.-Y. (2002). Synthesis of bidirectional texture functions on arbitrary surfaces. In *ACM Transactions on Graphics (TOG)*, volume 21, pages 665–672. ACM.
- [Toro and Burnod (2005)] Toro, R. and Burnod, Y. (2005). A morphogenetic model for the development of cortical convolutions. *Cerebral Cortex*, 15(12):1900–1913.
- [Walter *et al.* (2001)] Walter, M., Fournier, A., and Menevaux, D. (2001). Integrating shape and pattern in mammalian models. In *Proceedings of the 28th annual conference on Computer graphics and interactive techniques*, pages 317–326. ACM.
- [Wang and Marron (2007)] Wang, H. and Marron, J. (2007). Object oriented data analysis: Sets of trees. *The Annals of Statistics*, 35(5):1849–1873.
- [Wei and Levoy (2000)] Wei, L.-Y. and Levoy, M. (2000). Fast texture synthesis using tree-structured vector quantization. In *Proceedings of the 27th annual conference on Computer graphics and interactive techniques*, pages 479–488. ACM Press/Addison-Wesley Publishing Co.

- [Wexler *et al.* (2004)] Wexler, Y., Shechtman, E., and Irani, M. (2004). Space-time video completion. In *Computer Vision and Pattern Recognition, 2004. CVPR 2004. Proceedings of the 2004 IEEE Computer Society Conference on*, volume 1, pages I–120. IEEE.
- [Witkin and Kass (1991)] Witkin, A. and Kass, M. (1991). Reaction-diffusion textures. *ACM Siggraph Computer Graphics*, 25(4):299–308.
- [Wu and Yu (2004)] Wu, Q. and Yu, Y. (2004). Feature matching and deformation for texture synthesis. *ACM Transactions on Graphics (TOG)*, 23(3):364–367.
- [Wyawahare *et al.* (2009)] Wyawahare, M. V., Patil, P. M., Abhyankar, H. K., *et al.* (2009). Image registration techniques: an overview. *International Journal of Signal Processing, Image Processing and Pattern Recognition*, 2(3):11–28.
- [Yu *et al.* (2007)] Yu, P., Yeo, B. T., Grant, P. E., Fischl, B., and Golland, P. (2007). Cortical folding development study based on over-complete spherical wavelets. In *Computer Vision, 2007. ICCV 2007. IEEE 11th International Conference on*, pages 1–8. IEEE.
- [Yushkevich *et al.* (2003)] Yushkevich, P., Thomas Fletcher, P., Joshi, S., Thall, A., and Pizer, S. M. (2003). Continuous medial representations for geometric object modeling in 2d and 3d. *Image and Vision Computing*, 21(1):17–27.

Abstract

Geometric modeling has been one of the most researched areas in the medical domain. Today, there is not a well established methodology to model the shape of an organ. There are many approaches available and each one of them have different strengths and weaknesses.

Most state of the art methods to model shape use surface information only. There is an increasing need for techniques to support volumetric information. Besides shape characterization, a technique to differentiate objects by shape is needed. This requires computing statistics on shape.

In this work, we use a technique for shape modeling that is able to model surface and internal features and is suited to compute shape statistics.

Using this technique, a procedure to model the human cerebral cortex is proposed. This novel representation offers new possibilities to analyze cortical lesions and compute shape statistics on the cortex.

The second part of this work proposes a methodology to parameterize the interior of an object. The method is flexible and can enhance the visual or the physical properties of an object.

The geometric modeling enhanced with physical parameters is used to produce simulated magnetic resonance images. This image simulation approach is validated by analyzing the behavior and performance of classic segmentation algorithms for real images.

Keywords

S-rep, texture synthesis, shape statistiques, medical image simulation, cortex modeling.

Résumé

La modélisation géométrique a été l'un des sujets les plus étudiés pour la représentation des structures anatomiques dans le domaine médical. Aujourd'hui, il n'y a toujours pas de méthode bien établie pour modéliser la forme d'un organe. Cependant, il y a plusieurs types d'approches disponibles et chaque approche a ses forces et ses faiblesses.

La plupart des méthodes de pointe utilisent uniquement l'information surfacique mais un besoin croissant de modéliser l'information volumique des objets apparaît. En plus de la description géométrique, il faut pouvoir différencier les objets d'une population selon leur forme. Cela nécessite de disposer des statistiques sur la forme dans organe dans une population donné.

Dans ce travail de thèse, on utilise une représentation capable de modéliser les caractéristiques surfaciques et internes d'un objet. La représentation choisie (s-rep) a en plus l'avantage de permettre de déterminer les statistiques de forme pour une population d'objets.

En s'appuyant sur cette représentation, une procédure pour modéliser le cortex cérébral humain est proposée. Cette nouvelle modélisation offre de nouvelles possibilités pour analyser les lésions corticales et calculer des statistiques de forme sur le cortex.

La deuxième partie de ce travail propose une méthodologie pour décrire de manière paramétrique l'intérieur d'un objet. La méthode est flexible et peut améliorer l'aspect visuel ou la description des propriétés physiques d'un objet.

La modélisation géométrique enrichie avec des paramètres physiques volumiques est utilisée pour la simulation d'image par résonance magnétique pour produire des simulations plus réalistes. Cette approche de simulation d'images est validée en analysant le comportement et les performances des méthodes de segmentations classiquement utilisées pour traiter des images réelles du cerveau.